Remote Vessel Detection Using an Optical Imager and an AIS Receiver Combination for a CubeSat Constellation

Student:

Mr F.N. Lombard

Supervisor:

Prof. W.H. Steyn

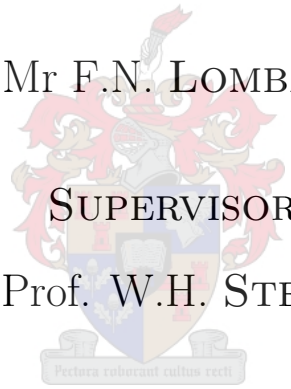

Dissertation presented for the degree of Master in Electronic Engineering at Stellenbosch University

Department of Electrical and Electronic Engineering
University of Stellenbosch
Private Bag X1, 7602 Matieland, South Africa

March 2020

Acknowledgements

I would like to thank my supervisor, Prof. Steyn, for his guidance and motivation throughout these two years.

Also, my close friends at the Electronic Systems Laboratory with whom I made many great memories with. I will always be thankful for the friendships and connections I made throughout my time there.

I would like to thank my family for their continuous support and love.

Lastly, I would like the thank the engineers I met at workshops who were kind enough to share their datasets.

Plagiarism Declaration

1. Plagiarism is the use of ideas, material and other intellectual property of another's work and to present it as my own.
2. I agree that plagiarism is a punishable offence because it constitutes theft.
3. I also understand that direct translations are plagiarism.
4. Accordingly, all quotations and contributions from any source whatsoever (including the internet) have been cited fully. I understand that the reproduction of text without quotation marks (even when the source is cited) is plagiarism.
5. I declare that the work contained in this assignment, except where otherwise stated, is my original work and that I have not previously (in its entirety or in part) submitted it for grading in this module/assignment or another module/assignment.

March 2020

F.N. Lombard — Date

Samevatting

Hierdie tesis ondersoek onwettige vissery aktiwiteite aan die kus van Suid-Afrika. Daar is tot die gevolgtrekking gekom dat 'n konstellasie van 10 6U satelliete wat wentel in 'n gespesialiseerde wentelbaan, met herhalende grond spore, die suksesvolste is om die Suid-Afrikaanse kus te observeer. Hierdie wentelbaan benodig 'n hellingshoek van 48° met 'n hoogte bo seespieël van 493.2 km. Boonop sal hierdie wentelbaan die satellietkonstellasie in staat stel om die kus met 'n passiewe kamera 35 keer per dag te ondersoek met 'n 10-dag sonsverduistering-periode in een sonjaar. Verder, in die Suid-Afrikaanse omgewing, kan dit radioseine stuur en ontvang vir 112 son-dae met n herbesoek periode van 10 ure. Ten slotte, is 'n omvattende kommunikasiekanaal analise gedoen en daar is bevind dat 95% van die vaartuie in die Suid-Afrikaanse kus opgevang sal kan word.

Drie wentelbane is vergelyk deur van 'n ontwikkelde MATLAB simulasie-omgewing gebruik te maak, wat 'n algemene vereenvoudigde versteuringsmodel implementeer. Verder is die kommunikasiemodel analise uitgevoer deur 'n realistiese steekproefruimte te skep wat gebaseer is op 'n realistiese verspreiding van vaartuie, asook om die vaartuie en satelliete se antennas te simuleer. Daar is bevind dat 85% van die vaartuie op die satelliet se radio-horison lê en dit word aanbeveel om 'n antennakonfigurasie met 'n sterker aanwins gerig na die horison te gebruik.

Daarna, is klassieke beeldverwerkingstegnieke ondersoek wat aanboord van 'n satelliet kan funksioneer. Beelde was suksesvol voorafverwerk om gebiede van belang, wat vaartuie bevat, te identifiseer. Hierdie gebiede se grense is verder verfyn en word geklassifiseer deur agt kenmerke uit die geïdentifiseerde gebiede te onttrek deur gebruik te maak van 'n linieêre masjienleer tegniek (support vector machine). Hierdie agt kenmerke word gekombineer om ses nuwes te skep met die doel om interklas variansie te verminder wat lei tot 'n klassifikasie telling van 72%.

Ter samevatting, hierdie tesis bied n suksesvolle uitvoerbaarheidsstudie of vaartuie opgespoor kan word in die Suid-Afrikaanse kus deur gebruik te maak van n 6U satelliet konstellasie. Dit sluit 'n omvattende lys van aanbevelings in waarmee hierdie tesis se uitkomste verbeter kan word.

Abstract

This thesis investigates illegal fishing activities on the coast of South Africa. It was concluded that a constellation of 10 6U satellites orbiting in a specialised orbit, with repeating ground tracks, is best for surveying South Africa's coast. This orbit will require an orbital inclination angle of 48° at an altitude of 493.2 km. It can survey the coast with passive imagers up to 35 times a day, with a 10-day eclipse period in a solar year. Furthermore, it can send and receive radio signals in the South African region for 112 solar days with a maximum revisit time of 10 hours. Lastly, a comprehensive communication link analysis was conducted, and it is concluded that 95% of the vessels in the South African coast can be intercepted.

Three orbits were compared using a simulation environment developed in MATLAB using a simplified general perturbation model. Additionally, the link analysis was performed by sampling the vessels from a realistic distribution and simulating the vessel and satellite antennas. It was found that 85% of the vessels lie on the satellite's radio horizon and it is recommended to have an antenna configuration with a stronger gain towards this region.

Thereafter, classical image processing techniques, that can function on board a satellite, were investigated. Images were successfully pre-processed to extract regions of interests containing vessels. These regions were refined and classified using a linear support vector machine that extracts eight features from candidate regions. These were combined into six new features with less interclass variance, resulting in a classification score of 71%.

To conclude, this thesis presents a successful feasibility study whether vessels can be detected in the South African coast using a 6U satellite constellation. It includes a comprehensive list of recommendations on which this thesis can be improved upon.

Contents

CONTENTS

List of Tables

List of Figures

LIST OF FIGURES

List of Algorithms

Nomenclature

Abbreviations and Acronyms

AA	Access Area
AC	Average Contrast
ADCS	Attidude Determination and Control System
AIS	Automatic Identification System
AoI	Area of Interest
ASCII	American Standard Code for Information Interchange
AtoN	Aids to Navigation
BER	Bit-Error Rate
BLOb	Binary Large Object
CA-CFAR	Cell-Average Constant False Alarm Rate
CB	Current Boundary
CCL	Connected Component Labelling
CP	Coverage Polygon
CR	Current Region
DAFF	Department of Agriculture, Forestry and Fisheries
DC	Daytime Coverage
DCM	Direction Cosine Matrix
DEM	Digital Elevation Map
DG	Dark Gaps
DoD	Depth-of-Discharge
DP	Douglas Peucker
EC	Earth Coverage
ECEF	Earth Centred Earth Fixed
EEZ	Exclusive Economic Zone

EM	Electromagnetic
EO	Earth Observation
ESA	European Space Agency
FAO	Food and Agriculture Organisation (of the United Nations)
FN	False Negative
FoV	Field of View
FP	False Positive
FPGA	Field-Programmable Gate Array
GLCM	Gray-Level Co-occurance Matrix
GMSK	Gaussian-Minimum Shift Keying
GPS	Global Position System
GSD	Ground Sampling Distance
GT	Gross Tonnage
HPBW	Half-Power Beam-Width
IB	Inner Boundary
IMO	International Maritime Organisation
IR	Infrared
ISS	International Space Station
ITU	International Telecommucanication Union
IUU	Illegal, Unreported and Unregulated
JPEG	Joint Photographic Experts Group
LEO	Low Earth Orbit(ing)
MLI	Multi-Layer Insulation
MMSI	Maritime Mobile Service Identities
MPA	Marine Protected Area
NASA	National Aeronautics and Space Administration
NC	Night-time Coverage
NCG	National Coast Guard

NIR	Near-Infrared
NL	Non-Linear
NMEA	National Marine Electronics Association
NOAA	National Oceanic and Atmospheric Administration
NORAD	North American Aerospace Defence Command
ORC	Orbit Reference Coordinate
PC	Peripheral Contrast
PCA	Principle Component Analysis
PDF	Probability Density Function
PER	Packet-Error Rate
PFT	Phase spectrum of the Fourier Transform
RAAN	Right order of the Ascending Node, Nodal Regression
RC	Radio Coverage
RGB	Red, Green, and Blue
RGT	Repeat Ground Track
RPY	Roll, Pitch and Yaw
S-AIS	Satellite Automatic Identification Systems
SA	South Africa(n)
SAMSA	South African Maritime Safety Authority
SCS	Space Commercial Services
SGP	Simplified General Perturbations Model
SNR	Signal-to-Noise Ratio
SOLAS	Safety of Life at Sea
SOTDMA	Self-Organised Time Division Multiple Access
SSO	Sun-Synchronous Orbit
SSP	Sub-Satellite Point
STK	Systems Tool Kit
SVM	Support Vector Machine

TLE	Two-Line Element
TMDA	Time Division Multiple Access
TN	True Negative
TP	True Positive
TT&C	Telemetry, Tracking and Commands
UHF	Ultra-High Frequency
US	Unitated States
UTC	Coordinated Universal Time
VDES	VHF Data Exchange
VDM	VHF Data-Link Message
VHF	Very High Frequency
VIS	Visible Spectrum
WRC	World Radiocommunication Conferences

Greek Letters

α	Absorbtivity, Atmospheric Drag, or Satellite Semi-Major Axis
δ	Small Change or Latitude
ℓ	Denoted Distance
η	Nadir Angle or Efficiency
γ	Satellite Look Angle
ι	Object Luminosity
κ	Kernel
λ	Earth Central Angle, Longitude, or Wavelength
μ	Earth's Gravitational Constant, Filter Window, or Mean
ν	True Anomaly, Principle Component
Ω	Nodal Regresion
ω	Argument of Perigee
π	PI constant
ρ	Earth Angular Radius, or Atmoshperic Density

σ	Standard Deviation or Radar Cross Section
τ	Reporting Interval
θ	Measuring Angle
ε	Elevation, or Emissivity,
φ	Latitude or Vessel Orientation

Lowercase Letters

c	Speed of Light in a Vacuum, Abbreviation for Cosine or Drag Coefficient
d	Pixel Size or Distance
d'	Diffraction Distance
e	Euler Axis
f	Focal Length, Object Feature, or Frequency
g	Gaussian Filter or Gravitational Acceleration
h	Perigee or Apogee Height
i	Orbital Inclination Angle, or Horizontal Image Axis
j	Vertical Image Axis or Complex Value
k	Boltzmann's Constant
m	Mass
n	Mean Motion
q	Quaternion
r	Pointint Distance
s	Seconds or Abbreviation for Sine
t	Time
u	Unit Vector
v	Velocity

Uppercase Letters

A	Surface Area
B	Bandwidth or Binary Image
C	Auxiliary Parameter for Helical Antenna or Signal Strength

D	Aperture or Days
E	Energy
F	Noise Figure or Fourier Transform ($\mathcal{F}$)
G	Antenna Gain or Image Gradient
H	Orbiting Altitude or Histogram
I	Intensity Image
J	Earth's Zonal Harmonics
L	Transmission Losses or Image Labels
M	Mean Anomaly or SOTDMA-Regions
N	Integer Number or Noise Power
P	Power, Pixels, Coordinate Point, Image Composite or Probability
R	Data-Rate, Rotation Matrix, Earth's Equatorial Radius, or Normalising Factor
S	Sensitivity, Sunlight Power Density, or Saliency Map
T	Period or Noise Temperature
W	Image Weight
X	Spatial Resolution or Battery Efficiency
X'	Ground Sampling Distance

1. Introduction

This thesis discusses an approach to identifying vessels in the coast of SA that refrain from broadcasting their whereabouts to nearby vessels and receiving stations along the coast. It investigates the current methodologies regarding illegal, unreported and unregulated (IUU) vessels in the exclusive economic zone (EEZ) of South Africa (SA). Ships and vessels are used interchangeably in most research papers; a vessel in this thesis refers to a ship of 300 gross tonnages or more. IUU includes the theft of a country's marine resources whereby a foreign vessel enters its EEZ, unannounced or without a licence, from international waters. Illegal fishing refers to fishing in the jurisdictional waters without the country's permission or in violation of its laws and regulations; not all unreported and unregulated fishing is illegal. Therefore, the easiest way to determine a possible guilty party would be to assess whether they have switched off their automatic identification system (AIS) within the EEZ. Lastly, the EEZ of a country dictates ownership regarding marine resources. This region is bound by the country's coastline that stretches out 370 km towards the ocean.

The SA EEZ, which is larger than its landmass, is made up of two separate areas, as depicted in Fig. 1.1 by the red and blue areas representing the *mainland* and *island* EEZs, respectively. The *mainland EEZ* is an area along the 3000 km SA coast, whereas the *island EEZ* is the Prince Edward archipelago, comprising the Marion and Prince Edward volcanic islands. Within the EEZs are marine protected areas (MPA) that are wildlife conservation and research areas [1], depicted as the yellow areas in Fig. 1.1.

IUU fishing reports highlight that one in five fish in global markets are caught illegally, equating to an annual value of $23.5 bn [2]. Furthermore, the NOAA satellite constellation is used to detect vessels fishing in low-light conditions: a common method for night-time fishing is to employ bright 300 kW lights to attract bait [3]. Squid, which is caught in this method, were targetted off the Peruvian coast by roughly 40 radio-silent Chinese fishing vessels in 2018 [2].

In 2013, two South Africans were ordered to pay R480 million for the West Coast Rock Lobsters they illegally harvested from the SA EEZ between 1987 and 2001 [4]. SA's ocean economy generates R6 billion annually [1]. The Marine Living Resources Act states that officers may seize any vessel believed to be partaking in illegal activities, which includes acting erratically or switching AIS off. However, vessels may switch off their AIS transponders so as to avoid detection for various reasons as per [5]. An airborne solution to AIS detection is aeroplanes with mounted AIS receivers. However, the southern oceans are too dangerous for this solution, as

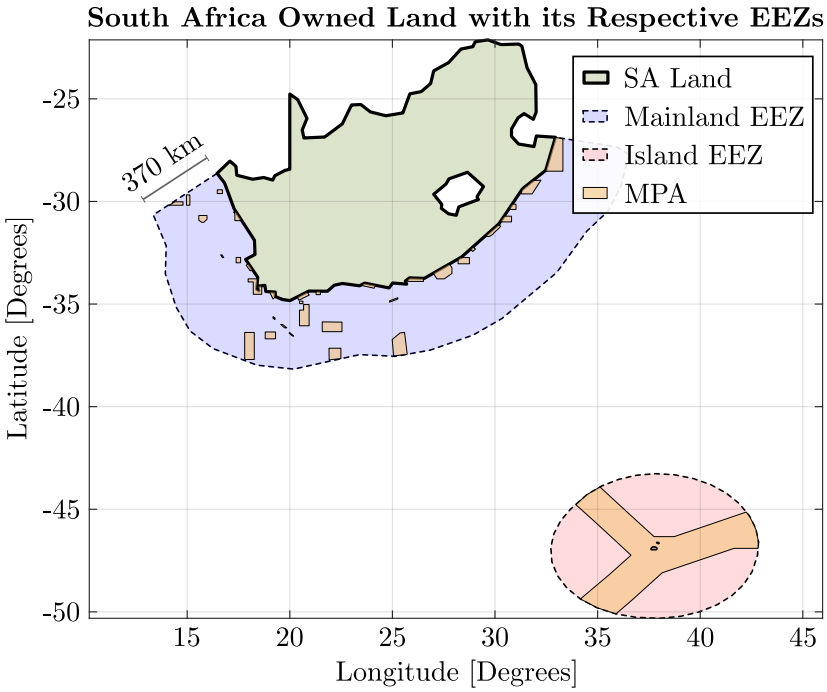

Figure 1.1: The area of interest for this thesis is the EEZ of SA. The mainland and islands EEZ is indicated as blue and red, respectively. Furthermore, all the SA MPAs are indicated with yellow blocks within the EEZs.

the strong winds could damage aircraft [6].

1.1 IUU in a SA Context

From an SA perspective, $1.5 \times 10^6\,\mathrm{km}^2$ of the ocean needs to be patrolled. Consequently, coastal surveillance becomes problematic considering that only the vessels dedicated to patrolling the coast are listed in Table 1.1. There are three inshore and one offshore Department of Agriculture, Forestry and Fisheries (DAFF) vessels, in addition to three inshore and two offshore SA Navy vessels dedicated to patrolling the EEZ [7], [8]. Three new 62 m by 11 m inshore patrol vessels, with a maximum speed of $37\,\mathrm{km\,h}^{-1}$, are scheduled for release by the end of 2023 [9], [10].

A patrolling vessel, the Victoria Mxenge listed in Table 1.1, was sent to escort a fleet of nine fishing vessels, travelling at $17\,\mathrm{km\,h}^{-1}$, that switched off their navigation lights and AIS to Saldanha Bay. One vessel, Lu Huang Yuan Yu 186 (20 m by 12 m), was impounded for marine pollution. Furthermore, only six of the nine vessels had AIS devices. Some of the vessels avoided conviction as they left SA's naval jurisdiction. With nearly 500 Chinese vessels operating in African waters, vessels must be anticipated so that they can be intercepted or prevented from "fishing the line" [11].

The Patagonian toothfish is the only targeted species around the Prince Edward Islands; 22 949 tonnes were caught illegally in 1997. As of 2006, there has been no

Table 1.1: List of DAFF and SAN patrol vessels.

Vessel Name	Top Speed	Range	Dimensions
Lillian Ngoyi	28 km h^{-1}	6500 km	47 m by 8 m
Ruth First	28 km h^{-1}	6500 km	47 m by 8 m
Victoria Mxenge	28 km h^{-1}	6500 km	47 m by 8 m
Sarah Baartman	41 km h^{-1}	13 900 km	83 m by 13 m
SAS Isaac Dyobha	59 km h^{-1}	5800 km	62 m by 8 m
SAS Galeshewe	59 km h^{-1}	5800 km	62 m by 8 m
SAS Tobie	59 km h^{-1}	850 km	22 m by 7 m
SAS Tern	59 km h^{-1}	850 km	22 m by 7 m
SAS Tekwane	59 km h^{-1}	850 km	22 m by 7 m

evidence of IUU activity in the aforementioned area, although data suggest that this resource is declining and may be depleted [1]. The islands have also been declared an MPA, as 8500 to 18 500 seabirds breeding on the islands have died due to both legal and illegal fishing operations [12]. The declared and estimated illegal catch for the island and eastern part of the mainland EEZ is depicted in Fig. 1.2, where the majority catch is blue shark (island EEZ), squid and linefish (Indian Ocean EEZ).

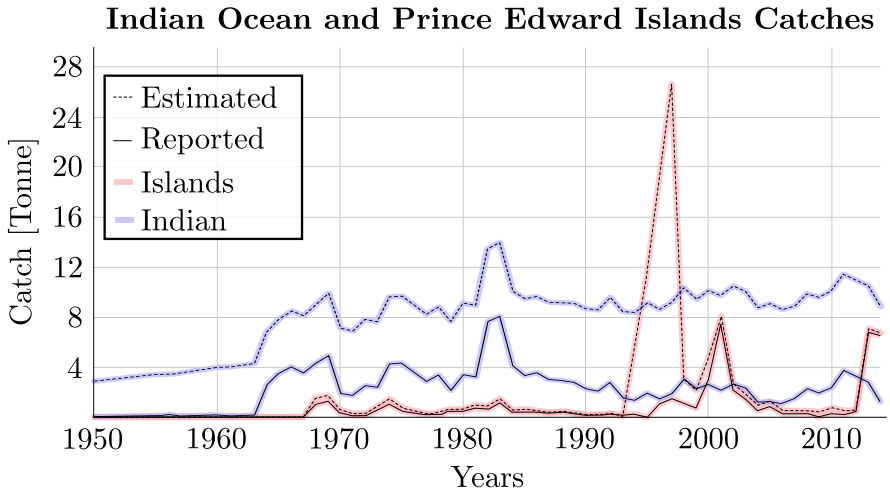

Figure 1.2: Thesis Area of Interest: EEZ of South Africa.

Lastly, the west coast's exploited marine life include: hake, anchovy, sardine, horse mackerel, tuna, snoek, rock lobster and abalone. The declared and the estimated illegal catch is displayed in Fig. 1.3 and it is clear that more fishing activity occurs in this section of the EEZ.

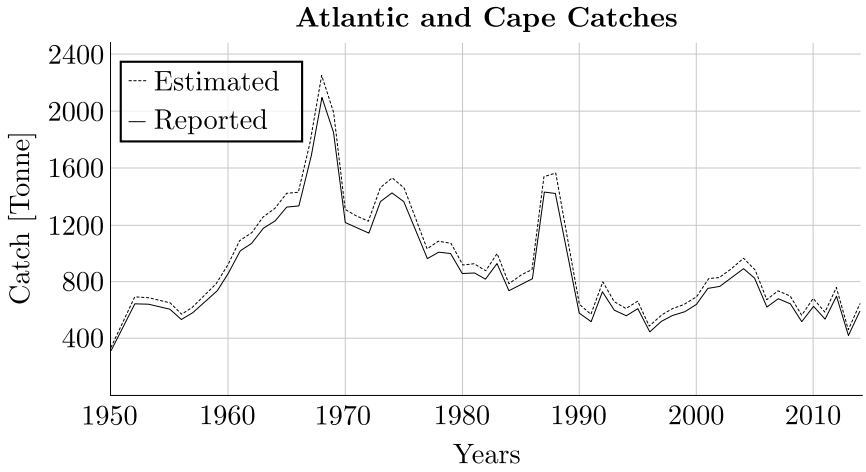

Figure 1.3: Atlantic and Cape catches in the western part of the EEZ. The dotted line is the unreported catches which includes major discards and illegal activity, whereas the solid line is the reported catches. This graph was adapted from [13].

1.2 Proposed Solution

It is clear that SA requires an effective surveillance solution that will generate local growth and is not dependent on foreign third parties, as commercially available AIS-data is costly. Notably, near-shore poaching is a difficult problem to address with a space-bourne solution, as the vessels are much smaller than the aforementioned ones, in addition to individuals poaching using scuba-equipment. It is decided under the author's discretion that small-scale poaching lies outside the scope of this thesis. A locally manufactured satellite constellation can remove restrictions on data-sharing and engage with the research-community. Prior research and flight heritage show that it is possible to receive AIS messages by using satellites [14]. However, packet loss and long durations of radio-silent vessels introduce possible tracking difficulties.

The proposed solution is to monitor the SA EEZ using AIS-data with auxiliary optical images acquired from a low earth orbit (LEO) constellation of satellites. Moreover, fixed land-based radars have a radio-horizon of approximately 25 km, depending on the antenna's height [15]. Therefore, this solution will only use AIS-data from space-borne solutions. The orbit should be such that SA has a high temporal resolution. Furthermore, optical solutions should be investigated to evaluate vessel-detecting capabilities. Finally, AIS detection success should be investigated to determine system reliability.

1.3 Thesis Outline

The general layout and process are summarized in Fig. 1.4 and will be elaborated on in the subsection to follow.

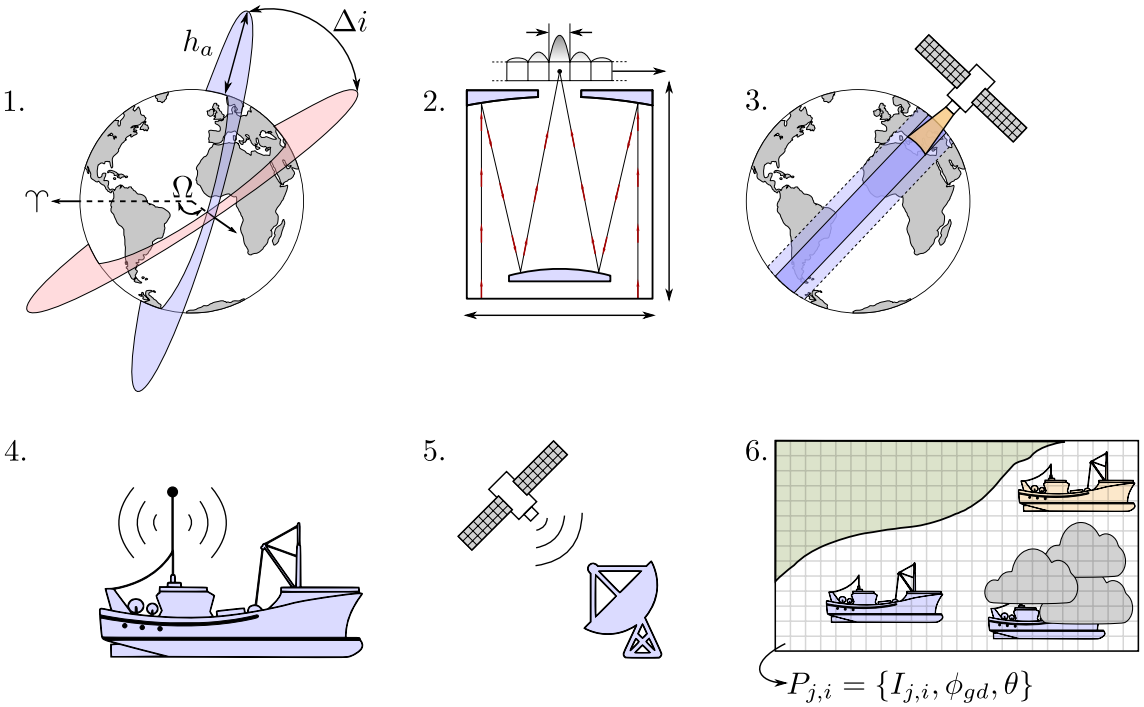

Figure 1.4: The thesis summary is depicted into six images in ascending order: orbital mechanics, payload inspection and requirements, coverage analysis given a selected orbit and payload, AIS link analysis, constellation mission design, and image processing.

Fig. 1.4.1: Firstly, a proper orbit for the satellite constellation must be decided upon. This includes determining the orbit's inclination and altitude, assuming that the orbit is circular and taking the impact that orbital perturbations will have on the resultant orbit into account.

Fig. 1.4.2: Secondly, the payload must be chosen based on the orbital analysis. The payload and communication frequency is restricted by the satellite's mass, dimensions and power constraints. The payload will determine the electromagnetic (EM) spectral bands that can be sensed, the swath width, and will influence the vessel detection algorithm. All of these variables will impact the satellite's power, storage, volume and mass budget. As such, these parameters will determine the effectiveness of the satellite and can only be iteratively chosen.

Fig. 1.4.3: Next, the orbit and payload coverage is investigated to determine the effectiveness of each considered orbit. The factors that influence the final decision will be: daytime and night-time-coverage, dark gaps, radio coverage, and area-of-interest coverage. The number of satellites in this constellation and the orbital inclination angle is the largest contributor. It is assumed that the constellation will consist of a single plane, assuming that two separate launches will be too expensive.

Fig. 1.4.4: Next, the AIS feasibility is inspected given the selected orbit and communication payload. It is assessed based on the number of vessels one can expect in the SA EEZ and in a typical satellite access area (AA) based on realistic AIS data, antenna analysis and the communication link.

Fig. 1.4.5: Penultimately, the satellite constellation's mission design is assessed. This chapter is in appendix B, it is a brief overview of a satellite's feasibility regarding the required payloads and orbit. This includes investigating the satellite's power, mass, link, and propulsion budgets and inter-satellite links.

Fig. 1.4.6: Finally, candidate vessel-detection algorithms are discussed for onboard processing. This introduces a three-step process of pre-processing images to highlight vessel-regions, extracting these regions and, finally, classifying whether the regions contains a vessel.

2. Background and Concepts

This chapter discusses the required information required to pursue the thesis. The following will thoroughly be investigated in order:

1. Maritime domain awareness and AIS,
2. Remote sensing,
3. LEO satellite,
4. Orbital mechanics,
5. The capabilities of CubeSats, and
6. A brief overview of image processing

2.1 Automatic Identification System

Since December 2004, the International Maritime Organisation's (IMO) International Convention for the Safety of Life at Sea (SOLAS) requires vessels with a minimum gross tonnage of 300 or when it is a passenger's vessel, to equip a 161.975 MHz Class A AIS-transceivers. In 2006, they required non-SOLAS and pleasure vessels to equip a 162.025 MHz Class B type AIS-transceiver. AIS transponders automatically broadcast vessel-related information at regular intervals, briefly summarised in Table 2.1. However, there are many areas where vessels congregate and signals may be lost due to interference.

Table 2.1: Message-reporting interval distributions for class A vessels (adapted from [16]).

	2 s	**6 s**	**10 s**	**180 s**
Deep Sea	25 %	55 %	15 %	5 %
Coast Line	10 %	65 %	10 %	15 %

AIS was developed to provide short-range identification and positioning information to both vessels and shore stations. AIS is widely used by national authorities to monitor the activities of their fishing fleets along their coastline, typically to a range of 72 km, assuming a vessel antenna height of 10 m. Furthermore, AIS-data can be used to identify exploited fishing areas, to monitor open and closed fishing areas, and provide real-time data on fishing activities [7]. Furthermore, the task to survey the coast will be even more difficult if the United Nations allow SA to expand its EEZ [17].

Each vessel controls its access to the AIS-network by using the self-organised time division multiple access (SOTDMA) protocol. A vessel listens on the channel before broadcasting and builds a schedule of when each other vessel will broadcast. Thereafter, it has a local replica of the current TDMA frame and can schedule its broadcasting period. SOTDMA functions on a best-effort basis; successful reception of any transmission is not acknowledged. A radio cell is formed and defined by the maximum communication distance, therefore, as two vessels approach one another their cells merge. Lastly, data is assumed to be lost when vessels in the same region transmit simultaneously.

The AIS ITU-R M.1371 technical standard allows for 4500 messages per minute if both AIS channels are used with a data-rate of 9600 bps. To avoid interference, AIS can operate in half-duplex mode and use 2250 slots per minute [18]. It uses Gaussian minimum shift-keying (GMSK) modulation with a receiving bandwidth time-product of 0.5 or 0.3 for a bandwidth of 25 kHz (high seas) or 12.5 kHz, respectively [18]. Furthermore, it allows 2250 time slots every 60 s resulting in a message duration of 26.6 ms. Class A vessels are equipped with a 12.5 W (±20% tolerance) omnidirectional monopole-antenna with a centre frequency of 162 MHz that has a 25 kHz bandwidth [18]. The AIS standard is depicted in Fig. 2.1.

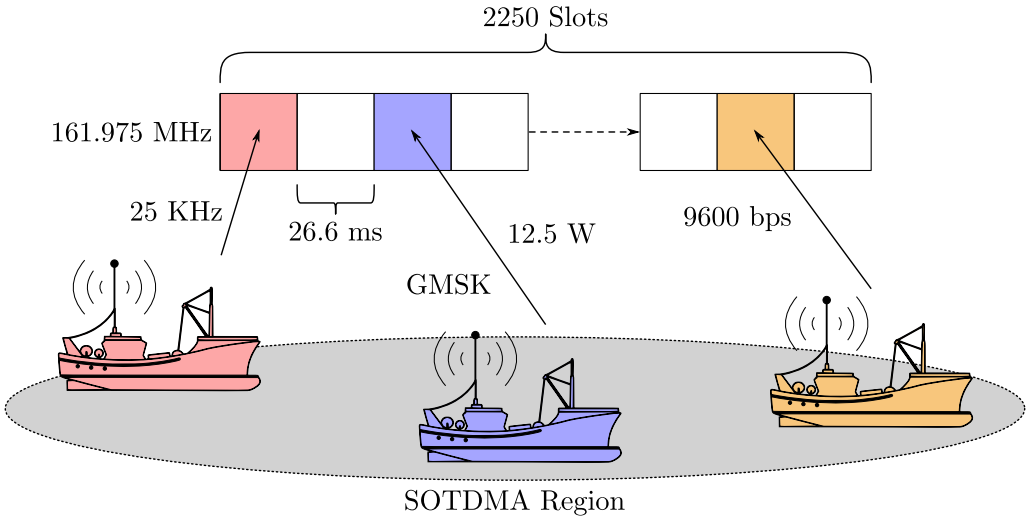

Figure 2.1: Depiction of the AIS standard that only expresses a single channel, 161.975 MHz.

If the number of AIS messages exceed the frame capacity in terms of reports per minute, the SOTDMA algorithm reduces the radio cell range. This is achieved with the *Robin Hood* algorithm and is initialized when 90% of the link load is achieved. Consequently, AIS stations closer than 22.2 km are prioritised by the receiver, whereas stations that are further away and broadcast weaker transmissions are suppressed [18].

The 27 AIS-message types are categorized as static, dynamic or voyage related,

each having different update rates. Static information is obtained during the AIS installation and need only be updated if the vessel undergoes a name or type change. Whereas dynamic information is automatically updated by sensors connected to the AIS-system. Finally, voyage-related information is entered manually and updated during the voyage.

AIS message five sends static information that includes the maritime mobile service identities (MMSI), the call sign and vessel name, the IMO number, length and beam, vessel-type, location and height of the fixed antenna, and auxiliary data which is reported every 6 min or when requested. There may exist duplicate MMSI numbers as they are not regulated. Flag registries allocate MMSI numbers and when a vessel changes its flag their MMSI number may be reallocated to another. This may result in a vessel appearing at two locations simultaneously, known as *spoofing*. A study done by Iphar et al. estimates that given a specific period: one in four vessels switch off their AIS 10% for the time and 2% of MMSI numbers are falsified [19].

AIS messages one to three is the dynamic information includes the vessel's position with an accuracy score, UTC time, course over ground, speed, heading, rate-of-turn, and navigational status; this is broadcasted as per Table 2.2. The voyage information will not be discussed. Furthermore, there are also short safety-related messages which are manually sent as required and are independent of timing. Lastly, AIS message 27 is a long-range broadcast message similar to messages one to three where redundant fields are removed to increase the number of delay bits. This message is only broadcasted once the vessel is out of range of a base station and it is taken under the author's discretion to include this message with types one to three [18].

EM waves with a frequency ranging between 30 MHz–300 MHz are denoted very high frequencies (VHF) signals. The transmission distances for these waves are approximately the line-of-sight as they travel in straight lines. It is roughly 30 km–75 km for land-based communications and it is limited by the curvature of the earth. Furthermore, VHF radio waves are affected by atmospheric conditions and landmass, resulting in variances in the signal range [20]. Each SOTDMA region is designed function with path delays not longer than 14 bits. The path delay distance is the maximum permissible distance between a sender and a receiver before messages in consequent NMEA slots overlap. It is calculated using 14 bits travelling at the speed of light, c_0, in a vacuum with the AIS baud rate of 9600 bps and to equates to a maximum range of

$$d_{\max} = 14\frac{c_0}{9600} \approxeq 437.2\,\text{km}$$

Typically, AIS has a maximum range of 75 km which is limited by the curvature of Earth.

2.1.1 Data-Link Message Encapsulation

The typical national marine electronics association (NMEA) 0183 standard AIS message is depicted in Fig. 2.2 that consists of 256 bits. The decoding of these messages lies outside the scope of this thesis.

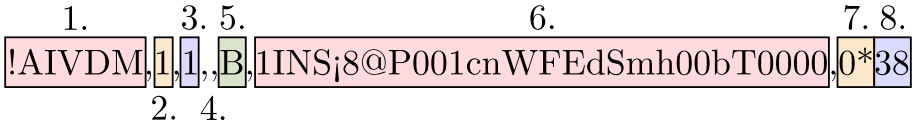

Figure 2.2: Depiction of the AIS standard for a position report. The following numbered fields correspond with their respective significance: 1: The NMEA message type, !AIVDM for data from other vessels and !AIVDO for the own vessel's information. 2: Number of sentences. 3: Sentence number. 4: Sequential message ID. 5: AIS channel used, either A or B. 6: Encoded AIS data using AIS-ASCII6. 7: End of data. 8: NMEA checksum.

Referring to the first field depicted in Fig. 2.2, the character "!" indicates the start of a sentence followed by two characters identifying the talker-type, in this case, *AI* is a mobile base station. Thereafter, the *VDM* indicate that the report is from other vessels, whereas, *VDO* would indicate packets being sent from the current vessel. The second field is the number of sentences being transmitted and the third field is the current sentence's number. The fourth field is the sequential message ID. The fifth field is the AIS channel in use designated by WRC-97 for worldwide use [18]. Field six is the encoded AIS data using AIS-ASCII6. Field 7 is the number of fill bits and the last field bit is the checksum delimiter.

Table 2.2: Class A vessel mobile equipment reporting intervals for dynamic messages (adapted from [18]).

Dynamic Conditions	**Rate [s]**
Anchored and travelling slower than 5.56 km h^{-1}	180 s
Anchored and travelling slower than 5.56 km h^{-1}	10 s
Travelling 0 km h^{-1}–25.9 km h^{-1}	10 s
Travelling 0 km h^{-1}–25.9 km h^{-1} and changing course	3.5 s
Travelling 25.9 km h^{-1}–42.6 km h^{-1}	6 s
Travelling 25.9 km h^{-1}–42.6 km h^{-1} and changing course	2 s
Travelling faster than 42.6 km h^{-1}	2 s
Travelling faster than 42.6 km h^{-1} and changing course	2 s

2.1.2 Space-Based Maritime Traffic Monitoring

Although never designed for this purpose, VHF AIS signals can be detected by satellites, as most use the VHF amateur band as a means of communications. This allows vessels to be detected outside the reach of base stations' terrestrial commu-

nication distance. Recent research has been dedicated to intercepting AIS-messages via satellites, called S-AIS. In dense traffic areas, S-AIS complements base stations' AIS-data. However, the temporal resolution of S-AIS depends on the satellite's orbit; as such, it cannot detect vessels as frequently as fixed terrestrial receivers.

A space-based AIS detector would receive uncoordinated messages from vessels belonging to different SOTDMA cells. The 4500 slots can easily be overwhelmed by the satellite's large field of view (FoV), described in chapter 4, that will result in message collisions that may result in data-loss. Therefore, the fundamental challenge for S-AIS is to receive large numbers of AIS messages simultaneously from within the satellite's large footprint. The number of messages collisions per timeslot depends on both the number of vessels in the satellite FoV and their reporting intervals, which will be elaborated upon in Sec. 4.4 [21] and is depicted in Fig. 2.3. The aim of S-AIS systems is to generate vessel location-data for route-monitoring applications. For this purpose, it is considered sufficient that the system provide a location update at least every 6 hours.

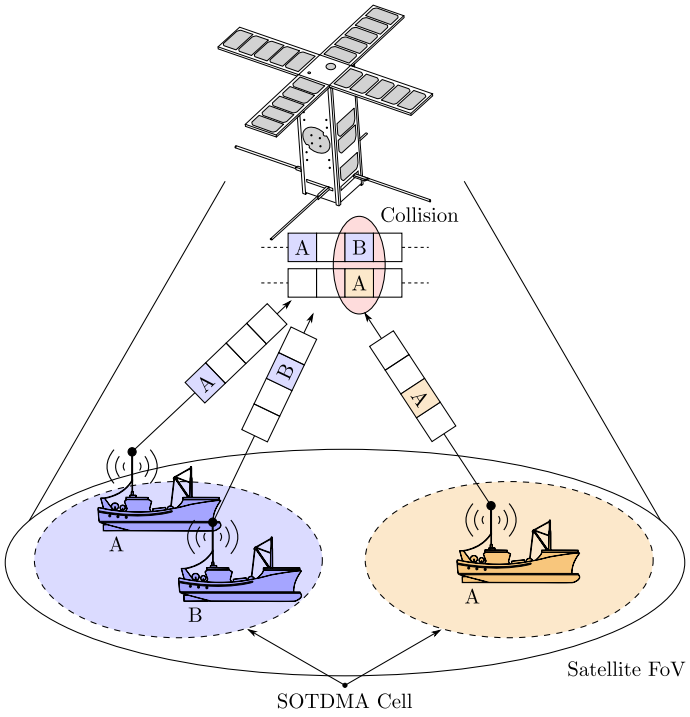

Figure 2.3: Satellite-based AIS SOTDMA-cell message collision illustration (adapted from [16]). Assuming that a vessel's antenna is situated 10 m above sea level, the communication distance will typically be 37 km. As such, the diameter of a SOTDMA-cell is in the range of 74 km because the antennas are omnidirectional.

2.1.2.1 The Doppler Effect

The Doppler frequency shift is a function of relative velocity between transmitter and receiver. In the case of the S-AIS system, the vessel's velocity is negligibly small

compared to the satellite's velocity, such that the Doppler shift can be calculated as

$$\Delta f = V_r/\lambda$$

Where λ is the wavelength of the transmitted AIS-signal and V_r is the component of the satellite velocity vector directed towards the vessel. This component will vary with the elevation and azimuth angles from zero, when the vessel's horizontal line-of-sight is orthogonal to the satellite's velocity vector, to the maximum when the elevation angle is at a maximum.

2.1.2.2 Other Propagating Effects

Interference exists from fixed and mobile terrestrial VHF systems in certain areas such as VHF Public Correspondence stations (VPC) in the maritime mobile services and Land Mobile Radio (LMR). Due to the lack of data, this potential interference is ignored under the author's discretion.

Faraday rotation occurs when a linearly-polarised wave passes through the ionosphere, leaving with a different polarisation angle. It is primarily dependent on the frequency, elevation angle, geomagnetic flux density and electron density in the ionosphere. If the satellite is equipped with a circularly polarised antenna, a constant 3 dB loss is induced when the satellite receives rotated linearly-polarised VHF waves from vessel antennas [16], [22]–[24].

2.2 Maritime Domain Awareness in South Africa

With the 2018 launch of ZACube-2, SA can monitor the EEZ traffic. The ZACube-2 is a 3U CubeSat that contains a medium resolution matrix imager and various communication subsystems. The payload data is downloaded using a S-band transmitter and high gain patch antenna. Furthermore, the Cubesat is equipped with a software-defined radio capable of decoding AIS and VHF data exchanges system (VDES) messages. VDES is being designed to extend the two AIS channels to at least eight and will include support for space communications for improved coverage [25].

2.3 Remote Sensing

Remote sensing is defined as obtaining reliable information about physical objects and the environment through the process of sensory systems, which in the case of this thesis, is an optical payload. Passive remote sensing uses sensors that detect the reflected or emitted EM energy from natural sources. The emissivity of a material, ε, is the relative ability of its surface to emit radiation, where a $\varepsilon = 1$ emits all frequencies. Whereas, active remote sensing uses sensors that transmit EM energy to detect the reflected energy. Active remote sensing falls outside the scope of this thesis, as it is assumed that CubeSats do not have enough energy for active remove

sensing solutions.

Roughly 60% of Earth observations are covered by clouds [26], which consists mainly of dry air mixed with liquid water drops, ice particles, or both. Thin and upper clouds, cirrus, are made of tiny ice particles. Consequently, clouds will restrict an optical payload from sensing vessels.

Lastly, remote sensing requires georeferenced data. Georeferencing is the process of assigning latitude and longitude coordinates to each pixel that will be further discussed in Sec. 5.5. For this thesis, the satellite images are focussed on the ocean and can assumed to be a flat surface. Therefore, no digital elevation map (DEM) is required to georeference data as illustrated in Fig. 2.4. However, for this thesis georeferencing will only be required on the open ocean to detect vessels to an accuracy of 1 km.

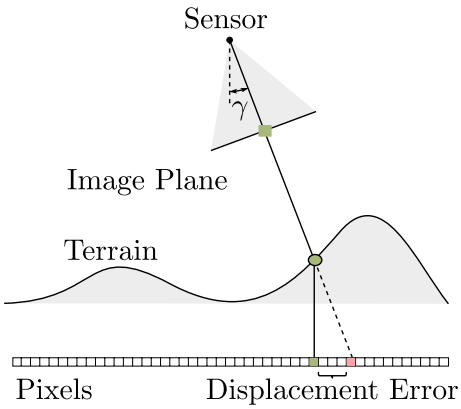

Figure 2.4: Depiction of the use of a digital elevation map to increase the accuracy of ortho-mapping.

2.4 Low Earth Orbit Satellites

Earth satellites that operate at altitudes from 160 km to 2500 km and are in near-circular orbits, are referred to as LEO satellites. These satellites have much stronger communication links because they are closer to Earth, leading to lower path losses which result in lower power. This may result in smaller antennas should the same power still be used. Furthermore, propagation delay is less because of shorter path distances compared to satellites with orbital altitudes lager than that of LEO.

LEO satellites' operations period is restricted by the satellite not being at a fixed location in the sky, instead, it sweeps across the sky for 10 to 14 minutes from a fixed location on Earth. If continuous global or wide area coverage is desired, a constellation of multiple LEO satellites is required with links between the satellites to allow for point-to-point communications. Current LEO satellite networks operate with 12, 24 and 66 satellites to achieve the desired coverage.

Polar orbits are often sun-synchronous orbits (SSO). The choice of altitude for a polar orbit is determined by several factors. A lower altitude orbit results in a short orbital period, poorer coverage, stronger signal returns, better spatial resolution, greater drag and a shorter lifetime. Satellite coverage depends on both the altitude and the AA of the sensor. For example, LandSat requires 16 days to provide full global coverage as it carries narrow AA instruments, whereas meteorological satellites provide full coverage twice a day.

Lastly, Earth's oblateness induces two major perturbations to the LEO orbit. Firstly, the point on the equator where the satellite crosses from south to north (the ascending node) will drift westward. Secondly, the semimajor axis will rotate either clockwise or counter-clockwise within the orbit plane. These effects will be discussed in greater detail in Sec. 2.5.1.

2.4.1 Satellite Geometry

This subsection elaborates on the required geometry to express the relevant angles and distances regarding a satellite pointing off-nadir. The necessary relations are depicted in Fig. 2.5 and expressed as per Eqs. (2.1) to (2.6) [27]. It should be noted that these are planar relationships and that the satellite's look angle, η, lies within the plane when referring to Fig. 2.5. Furthermore, the sub-satellite point (SSP) is the coordinate on Earth closest to the satellite, which is calculated as the intersection between the Earth's surface and a line from the Earth's centre to the satellite.

Eqs. (2.1) to (2.6) use the geocentric coordinate system. As the Earth is oblate, not all lines orthogonal to Earth's surface intersects its centre. Therefore, geocentric coordinates should be converted to geodetic coordinates for the points to lie on Earth's surface. Notably, in general GPS coordinates used to describe locations on

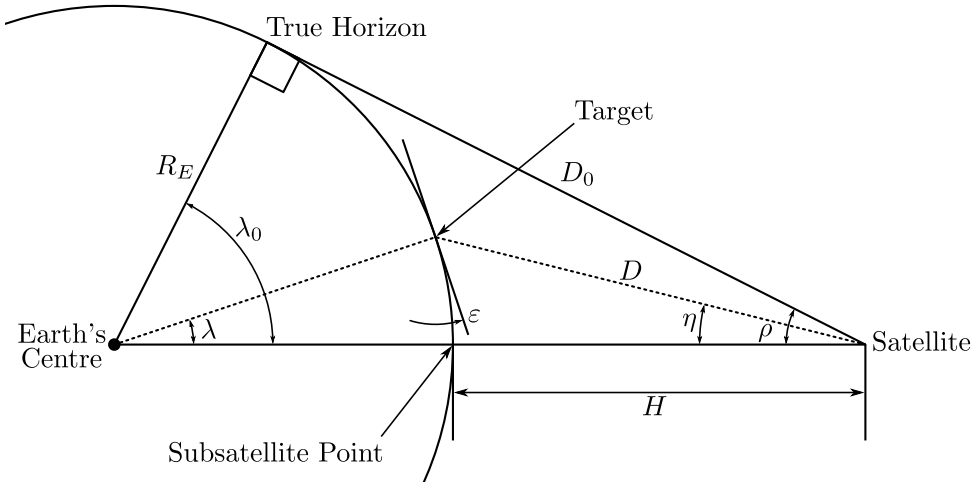

Figure 2.5: Angular and distance relationships between the satellite, target and Earth's centre (adapted from [27]).

Earth use geodetic coordinates. This is achieved by:

$$\phi_{gd} = \arctan\left[\left(1 - 0.081819^2\right) \cdot \tan\phi_{gc}\right]$$

Where subscripts gd and gc denote geodetic and geocentric latitudes, respectively.

$$\sin\rho = \cos\lambda_0 = \frac{R_\oplus}{R_\oplus + H} \tag{2.1}$$

$$\tan\eta = \frac{\sin\rho\sin\lambda}{1 - \sin\rho\cos\lambda} \tag{2.2}$$

$$\cos\varepsilon = \frac{\sin\eta}{\sin\rho} \tag{2.3}$$

$$\eta + \lambda + \varepsilon = \frac{\pi}{2} \tag{2.4}$$

$$D = R_\oplus \frac{\sin\lambda}{\sin\eta} \tag{2.5}$$

$$D_0 = \frac{R_\oplus}{\tan\rho} \tag{2.6}$$

2.5 Orbital Elements

This section elaborates on the parameters required to accurately describe an orbit at epoch. The epoch is the time at which the time-dependent orbital elements are observed. For this thesis, the Keplerian elements are chosen to describe an orbit and are as follows:

1. Eccentricity (ε),
2. Semimajor axis (α),

3. Longitude of the ascending node or nodal regression (Ω) is measured from the Vernal Equinox (Υ), ascending node (Ω), and descending node ($\mho$),
4. Inclination (i),
5. Argument of perigee or nodal precession (ω),
6. True anomaly (ν)

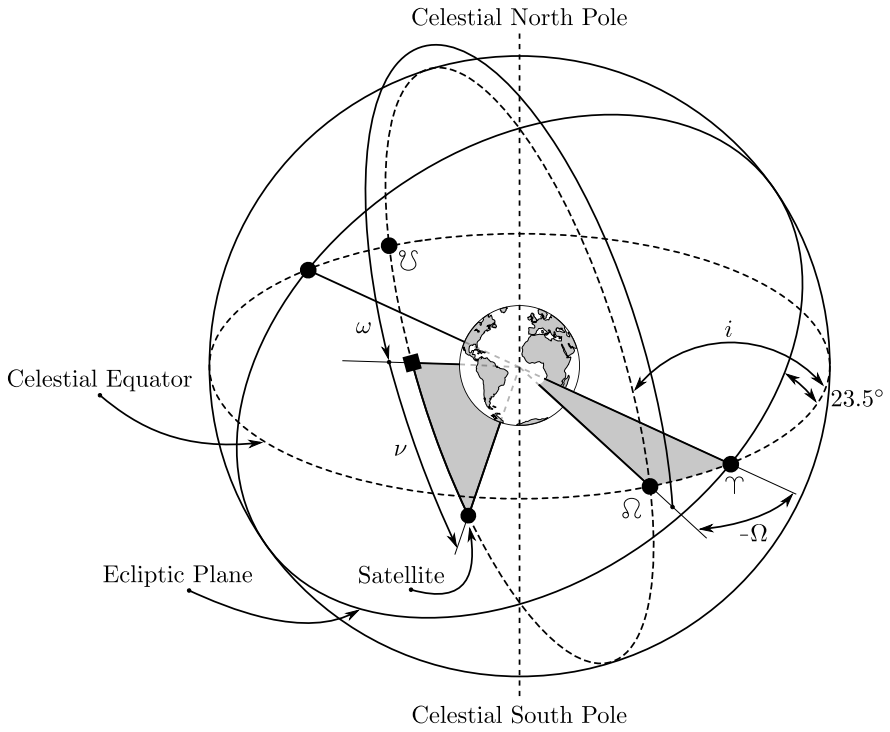

Figure 2.6: Depiction of Keplerian elements used to describe an orbit given an epoch. The celestial body, in this case, is the satellite orbiting along the dotted line. The other dotted line is the celestial equator which is used as reference to measure the orbit plane's inclination angle, i. The Vernal Equinox (Υ) is used as an inertially fixed reference direction to measure the RAAN (Ω). The ascending and descending nodes are indicated with $\Omega$and $\mho$, respectively. The argument of perigee and true anomaly are depicted with ω and ν, respectively.

The elements are illustrated in Fig. 2.6 using a celestial sphere. This sphere is an abstract concept used in astronomy and navigation where all of the visible objects from Earth is projected to the inside of the sphere of unit length. The ecliptic plane is the Sun's orbit relative to Earth projected onto the sphere and the celestial equator lies in between the celestial poles. Consequently, the Vernal Equinox is the ascending node where the ecliptic crosses the celestial equator.

Because the celestial sphere is of unit length, α and ε are omitted. The orbit eccentricity describes the orbit circularity, zero indicating perfectly circular and one being a parabola. The semimajor axis is the sum of the apogee and perigee divided

by two. It indicates the satellites orbiting altitude. The longitude of the ascending node (also called the right ascension of the ascending node, RAAN) describes the rotation of the orbiting plane about the Earth's axis. The ☊ and ☋ are the points where the satellite crosses the equator on an ascending or descending motion, respectively. The orbit inclination, i, is the angle that the orbiting plane makes with the equator, measured at ☊. If i is 0° the satellite orbits in the same direction as Earth's rotation. As such, when i is less than 90° the orbit called a prograde orbit and when i is larger than 90° the orbit is called a retrograde orbit. ω is the angle from ☊ to the perigee within the orbiting plane. Finally, ν describes the satellite's angular position (true anomaly angle) within the orbiting plane, measured from ω.

The final parameter not previously mentioned is the mean anomaly (M), which is used to describe the position of a satellite in an eccentric orbit as if though the orbit was perfectly circular. As such, the mean anomaly scales linearly with time and is described as

$$M = M_0 + n(t - t_0)$$

where n is the satellites mean motion in radians per second, M_0 is the mean anomaly at epoch.

The mean motion of a satellite is the average angular velocity calculated as

$$n = \frac{2\pi}{T}$$

Where T is the orbit period and is calculated as

$$T = 2\pi\sqrt{\frac{\alpha^3}{\mu}}$$

Where μ is the Earth's gravitational constant. It can be shown that this formula is related to constant angular momentum and holds true for circular and elliptical orbits. Consequently, the true anomaly can be estimated using the mean anomaly as

$$\nu \approx M + 2\varepsilon \sin M + 1.25\varepsilon^2 \sin(2M)$$

However elliptical orbits were considered, after calculations, it was deemed a poor option, as the changing argument of perigee will result in the satellite becoming out of phase with the EEZ and will drastically reduce the observation time. As such, only circular orbits with small eccentricities will be considered.

2.5.1 Orbit Perturbing effects

The orbital plane would remain fixed in space should no external forces act on the system. However, when introducing perturbing forces onto the dynamics of the system, this no longer holds true. These forces, described in Table 2.3, induce

secular (slow change over time) and periodic changes onto the orbiting plane listed in Table 2.4. For this thesis, the secular effects of the sun and moon are neglected in calculations. For the orbital design process described in Sec. 4.3, the second (J_2), fourth (J_4), and sixth (J_6) zonal harmonic constants for non-spherical Earth are considered, which do not depend on longitude [28].

Table 2.3: Forces perturbing a satellite's Keplerian elements with their respective sources.

Force	**Source**
Non-spherical gravitational field	Non-spherical and non-homogeneous Earth
Gravitational attraction of auxiliary bodies	Moon, planets
Radiation pressure	Sun's radiation
Particle flux	Solar wind
Lift and drag	Residual atmosphere
EM forces	Interaction of electrical currents in the satellite with the Earth's magnetic field

The eccentricity only has a secular effect for LEO satellites. Large secular effects strongly influence the RAAN, orbit-perigee (ω), and altitude. These perturbations can be monitored by observing the satellite's orbital elements and adjust the orbit accordingly by using on-board thrusters.

Table 2.4: Sources to large and small secular and periodic perturbing forces.

	Secular		**Periodic**	
	Large	Small	Moderate	Small
Earth's Oblateness	Ω, ω	-	ϵ	i, Ω, ω
Sun and Moon	-	Ω, ω	-	α, ϵ, i, Ω, ω
Atmospheric Drag	α, ϵ	i	-	Ω, ω
Solar Radiation Pressure	-	-	-	α, ϵ, i, Ω, ω

The gravitational potential of the Earth is a complicated function of the Earth's shape. In cross-section, the Earth is approximately elliptical. The average distance from the centre of the Earth to the equator is specified as according the World Geodetic System (WGS) 1984 as 6378.137 km, whereas the distance to the poles is 6356.752 km. The gravitational potential of the Earth is given approximately by [29]:

$$U = -\frac{\mu}{\alpha}\left[1 + \frac{1}{2}J_2\left(\frac{R_\oplus}{\alpha}\right)^2\left(1 - 3\sin^2\delta\right) + ...\right]$$

Where $R_\oplus$ is Earth's equatorial radius and δ is the latitude.

The higher-order zonal harmonic terms, J_4 and J_6, are more than two orders of magnitude smaller than J_2 but are necessary for accurate calculations. Consequently, a satellite travels at a slightly different speed in a gravitationally perturbed orbit. The time-rate of change of the mean anomaly is given by the mean motion (n) in the unperturbed orbit and by the anomalistic mean motion constant (n_a) in a perturbed orbit. Considering zonal harmonics J_2, J_4 and J_4, the anomalistic mean motion is described as[29]:

$$\frac{dM}{dt} = n_a = n_0 + \dot{M}_{sec} + \mathcal{O}\left(J_8\right)$$

where $\dot{M}_{sec}$ is the secular effects on the orbit. For this thesis, periodic effects are deemed as negligible. When the inclination angle lies between 54.7° and 125.3°, n_a is less than n, resulting in the satellite orbiting slower than it would in an unperturbed orbit. The effect that the perturbing forces have on the mean anomaly, RAAN, and precession rate is expressed by Eqs. (2.8) to (2.10), respectively [29].

The three orbital elements, α, ε, and i, undergo small, oscillatory changes induced by Earth's oblateness that may be neglected, when inspecting Table 2.4. The interval between successive passages at perigee is called the anomalistic period, which differs from the Keplerian period, and is expressed as:

$$T_a = \frac{2\pi}{n_a}$$

However, because M is measured from perigee, the anomalistic period is the time interval for the satellite to travel from perigee to moving perigee. Whereas the nodal or draconic period, T_N, is the time interval between two successive ascending node passages. An exact value of T_N must be calculated numerically, however, the following is a good approximation [30]:

$$T_N = \frac{2\pi}{n_a + \dot{\omega}} \tag{2.7}$$

$$
\begin{aligned}
\dot{M}_{sec} =& \frac{3n_0 J_2\sqrt{1-\varepsilon^2}}{4}\left(\frac{R_\oplus}{\alpha}\right)^2\left[3\sin^2(i)-2\right] \\
&+\frac{3n_0 J_2^2}{512\sqrt{1-\varepsilon^2}}\left(\frac{R_\oplus}{\alpha}\right)^4\left[320\varepsilon^2-280\varepsilon^4\right. \\
&\qquad +\left(1600-1568\varepsilon^2+328\varepsilon^4\right)\sin^2(i) \\
&\qquad \left.+\left(-2096+1072\varepsilon^2+79\varepsilon^4\right)\sin^4(i)\right] \\
&-\frac{45n_0 J_4\varepsilon^2\sqrt{1-\varepsilon^2}}{128}\left(\frac{R_\oplus}{\alpha}\right)^4\left[-8+40\sin(i)-35\sin^2(i)\right] \\
&-\frac{35n_0 J_6\varepsilon^2\sqrt{1-\varepsilon^2}}{2048}\left(\frac{R_\oplus}{\alpha}\right)^6\left[-128+320\varepsilon^2+24\varepsilon^4\right. \\
&\qquad +\left(1344-3360\varepsilon^2-2520\varepsilon^4\right)\sin(i) \\
&\qquad +\left(-1512+3780\varepsilon^2+2835\varepsilon^4\right)\sin^2(i) \\
&\qquad \left.-\left(-1848+4620\varepsilon^2+3465\varepsilon^4\right)\sin^4(i)\right]
\end{aligned} \tag{2.8}
$$

$$
\begin{aligned}
\dot{\Omega}_{sec} =& -\frac{3n_a J_2\cos(i)}{2}\left(\frac{R_\oplus}{\alpha}\right)^2 \\
&+\frac{3n_a J_2^2\cos(i)}{32}\left(\frac{R_\oplus}{\alpha}\right)^4\left[12-4\varepsilon^2-\left(80+15\varepsilon^2\right)\sin^2(i)\right] \\
&+\frac{15n_a J_4\cos(i)}{32}\left(\frac{R_\oplus}{\alpha}\right)^4\left[8+12\varepsilon^2-\left(14+21\varepsilon^2\right)\sin^2(i)\right] \\
&-\frac{105n_a J_6\cos(i)}{1024}\left(\frac{R_\oplus}{\alpha}\right)^6\left[64+160\varepsilon^2+120\varepsilon^4\right. \\
&\qquad -\left(288+720\varepsilon^2+540\varepsilon^4\right)\sin^2(i) \\
&\qquad \left.+\left(264+660\varepsilon^2+495\varepsilon^4\right)\sin^4(i)\right]
\end{aligned} \tag{2.9}
$$

$$
\begin{aligned}
\dot{\omega}_{sec} =& \frac{3n_a J_2}{4}\left(\frac{R_\oplus}{\alpha}\right)^2\left[4-5\sin^2(i)\right] \\
&+\frac{9n_a J_2^2}{384}\left(\frac{R_\oplus}{\alpha}\right)^4\left[56\varepsilon^2+\left(760-36\varepsilon^2\right)\sin^2(i)\right. \\
&\qquad \left.-\left(890+45\varepsilon^2\right)\sin^4(i)\right] \\
&-\frac{15n_a J_4}{128}\left(\frac{R_\oplus}{\alpha}\right)^4\left[64+72\varepsilon^2-\left(248+252\varepsilon^2\right)\sin^2(i)\right. \\
&\qquad \left.+\left(196+189\varepsilon^2\right)\sin^4(i)\right] \\
&+\frac{105n_a J_6}{2048}\left(\frac{R_\oplus}{\alpha}\right)^6\left[256+960\varepsilon^2+320\varepsilon^4\right. \\
&\qquad -\left(2048+6680\varepsilon^2+2160\varepsilon^4\right)\sin^2(i) \\
&\qquad +\left(4128+13080\varepsilon^2+3960\varepsilon^4\right)\sin^4(i) \\
&\qquad \left.-\left(2376+14520\varepsilon^2+2145\varepsilon^4\right)\sin^6(i)\right]
\end{aligned} \tag{2.10}
$$

The satellite's mean angular velocity is expressed by the nodal mean motion, n_N. The relation between nodal and anomalistic mean motions is expressed as:

$$n_N = n_a + \dot{\omega}$$

Additionally, drag perturbations also affect the nodal period, however, it is assumed the satellite's α is corrected with in-orbit manoeuvres; as such, remains constant.

Table 2.5: Constant sidereal parameters.

Parameter	**Value**
s_m	84 600 s
T_{sid}	31 558 149.504 s
D_{sid}	365.256 30 day

With reference to Table 2.5, a sidereal day is the time required for the earth to rotate 360° with respect to far-away stars in the celestial sphere. Additionally, a solar day is the time required for the earth to rotate 360° with respect to the sun. Furthermore, the angular velocity of the Earth's axis around the Sun can be expressed as

$$\omega_{\oplus} = \frac{2\pi}{T_{sid}}$$

Where T_{sid} is the number of seconds in a sidereal year. Lastly, the orbit's longitudinal revolutions per year, P, is expressed as [30]:

$$P = \frac{\dot{\Omega} T_{sid}}{2\pi} \tag{2.11}$$

Earth's zonal harmonics influence the ascending node such that it regresses secularly along the equator. Consequently, the satellite's ground-track shift, λ_S, between consecutive equator crossings is defined by how far the Earth rotates during the nodal period; it is relative to the ascending node located in inertial space. Considering the Earth's angular velocity, $\omega_{\oplus}$, and the satellite's nodal regression, the angular spacing is expressed by:

$$\lambda_S = T_N \left(\omega_{\oplus} - \dot{\Omega} \right)$$

Because the Earth rotates eastward, the next consecutive prograde satellite equator-crossing will be west of the previous one. Furthermore, the number of satellite-revolutions in a nodal day, or nodal day orbital frequency, is expressed in Eq. (2.12) [30]. It takes Earth's rotation into account and if N is an integer, the satellite will return to the same location after a sidereal day if the atmospheric drag is compensated. This is further discussed in Sec. 4.3.3.

$$N = \frac{n_a + \dot{\omega}}{\omega_{\oplus} - \dot{\Omega}} \tag{2.12}$$

2.6 Cube Satellites

This section will elaborate on Cube Satellites (CubeSats), shown in Fig. 2.7 with its respective body coordinates, and how to introduce them into a simulation environment. Satellite technology has a high temporal resolution compared to ground-based or airborne measurements with improved coverage. Consequently, satellites are ideal for weather forecasting, disaster monitoring, water management, pollution, and agriculture and have become attractive for their reduced cost per kilogram [31]. The CubeSat is a miniaturized satellite with a standardized unit (U), where 1U will measure $10 \times 10 \times 10$ cm^3 and will weigh no more than 1.33 kg [32].

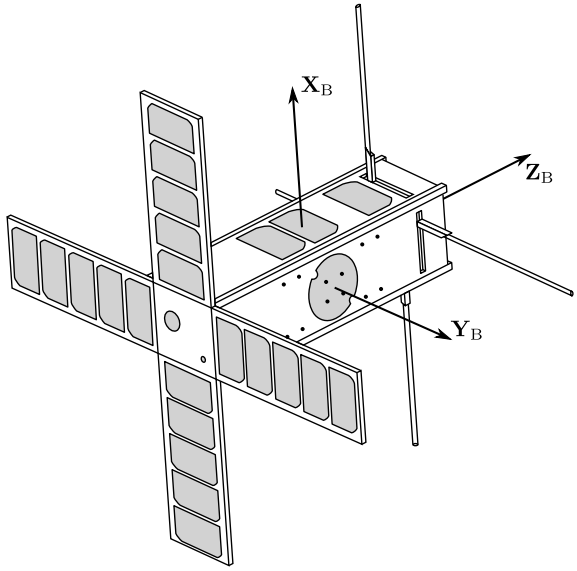

Figure 2.7: Depiction of a 3U CubeSat with its body coordinates. The Z-axis points in the direction of the payload and the x-axis points towards the closes point on the shortest edge.

2.6.1 Orbital Parameters

A cost-effective and viable option to launch CubeSats is by use of the Electron Rocket. This solution can launch satellites into orbital inclination angles ranging from 39° to 98°, with respective payload masses of 224 kg and 142 kg at an altitude of 600 km [33]. Consequently, the maximum mass and altitude for this thesis is chosen as 142 kg and 600 km. The orbit injection accuracies and deployment rates for the rocket is listed in Table 2.6.

SGP4, which was developed in 1970 by Ken Cranford, is a simplified general perturbations mathematical model used for LEO satellite position prediction. It uses the solution of Brouwer for its gravitational model and a power density function for its atmospheric model [34]. SGP4 requires a publicly available two-line element (TLE) set and uses UTC time, generated by the North American Aerospace Defence Command (NORAD) that encodes the satellite's orbital elements into a text file as

Table 2.6: Electron Rocket deployment accuracies and rates (adapted from [33]).

Parameter	**Margin**
Inclination	$\pm 0.15°$
Perigee	$\pm 15\,\mathrm{km}$
Apogee	$\pm 15\,\mathrm{km}$
Attitude	$\pm 5°$
Rates	$\pm 1\,°\,\mathrm{s}^{-1}$

Line 1:

01	03-07	08	10-11	12-14	15-17	19-20	21-32	34-43	45-52	54-61	63	65-68	69
01	02	03	04	05	06	07	08	09	10	11	12	13	14

Line 2:

01	03-07	09-16	18-25	27-33	35-42	44-51	53-63	64-68	69
01	02	03	04	05	06	07	08	09	10

Figure 2.8: TLE set description with each respective line (L). The red is the column (C) and the blue is the characters in the text file containing the relevant content. The content is elaborated upon in Table 2.7.

expressed in Fig. 2.8. The file's respective lines' (L) and columns' (C) contents are elaborated upon in Table 2.7. The values: n, ε, i, Ω, ω, and M are independent quantities required for calculations and the remaining variables: $\dot{n}$, $\ddot{n}$, and B^* are required to describe the effect of perturbations on the satellite's motion. The B^* is the SGP4 drag coefficient [35] and is calculated as

$$B^* = \frac{c_D A}{2m}\rho_0 \tag{2.13}$$

Where c_D is the drag coefficient, which is determined by satellite's shape and is usually 2.2, A is the frontal area, ρ_0 is the atmospheric density at orbit perigee, and m is the satellite's mass. The true ballistic coefficient, BC, is approximated by using B^* term as:

$$BC = \frac{R_\oplus \rho_0}{2B^*}$$

The SGP4 model uses zonal harmonics J_2 and J_4 to approximate secular perturbing effects [35], whereas SGP uses the pseudo drag terms $\frac{\dot{n}}{2}$ and $\frac{\ddot{n}}{6}$ in a truncated Taylor series expansion to approximate the anomalistic mean anomaly [28]. The harmonics J_2 and J_4 have to be considered when propagating an artificial satellite for longer than weeks. Furthermore, terms $\dot{n}$ and $\ddot{n}$ will not be further discussed [34].

SGP4 is only accurate enough to track a satellite with an orbital period of fewer than 225 min, as the TLE is limited by decimal places. This translates to an accuracy at an epoch in the order of 1 km.

Table 2.7: TLE Content Description

L	C	Content	L	C	Content
1	1	Line Number	2	1	Line Number
1	2	Satellite Catalogue Number	2	2	Satellite Catalogue Number
1	3	Classification (U, C or S)	2	3	Inclination (degrees), i
1	4	Last two digits of the launch year	2	4	RAAN (degrees), Ω
1	5	Launch number of the year	2	5	Eccentricity, ε
1	6	Piece of the Launch	2	6	Argument of perigee, ω
1	7	Last two digits of the epoch year.	2	7	Mean anomaly (degrees), M
1	8	Day of the year and fractional portion of the day.	2	8	Mean motion (revolutions per day), n
1	9	SGP ballistic coefficient ($\frac{\dot{n}}{2}$)	2	9	Revolution number at epoch (revolutions)
1	10	Second derivative of the mean motion ($\frac{\ddot{n}}{6}$)	2	10	Checksum
1	11	Drag term (radiation pressure coefficient or B^*)	-	-	-
1	12	Ephemeris type (usually 0)	-	-	-
1	13	Element set number, incremented when a new TLE is generated for the satellite.	-	-	-
1	14	Checksum.	-	-	-

2.7 Image Processing

This section will elaborate on uncooperative vessel detection in optical satellite composites. Optical imagery is attractive due to its low cost and ease of management. Synthetic aperture radar is another means of acquiring satellite images but is infeasible for CubeSat solutions as expressed in appendix B.5. Optical imagery implies passive sensors that rely on illumination from the sun. For this thesis, the investigated EM bands are the visible spectrum (VIS), that ranges from 400 nm–700 nm, and reflected infrared that covers the near-and short-wave infrared bands (NIR) up to 3 µm, as depicted in Fig. 3.4. A CubeSat has limited battery capacity that would restrict its thermal IR's imaging effectiveness at surveying the SA EEZ because the IR sensors have to be cooled down. For this thesis, different bands are combined into a greyscale image as a satellite's onboard memory is limited [36]. The near-infrared spectrum ranges from 750 nm–1400 nm and is defined by water absorption, as seen in Fig. 3.4.

Vessel detection refers to the process of locating vessel candidates in the satellite

Figure 2.9: Vessel in the presence of cloud presence with a coast. The vessel is enlarge to ease visibility. The image was acquired by Sentinel-2 on 2019-04-29 with 1.2% cloud coverage, 76.8% water coverage.

images. After which, classification is used to discriminate detected candidates between the vessel and non-vessel type. Vessel-identification from optical imagery falls outside the scope of this thesis.

Several factors influence vessel detection: heavy clouds, complex ocean states, sunglint, and image acquisition angles. This is shown in Fig. 2.9, as it is clear that many of the clouds appear to look like vessels. For optical imagery to be feasible, there has to be the absence of heavy clouds and strong waves. Night-time imagery that penetrates clouds is possible, however, the required imagers have to be cooled down to low Kelvins and have low spatial resolutions in the range 1 km when nadir-looking. Furthermore, only bright lit vessels will be detected and grouped with others.

Table 2.8: Vessel detection summary using passive sensing for the period of 1978-2017 [37].

Method	**Algorithms**	**Advantages**	**Disadvantages**
Threshold	Otsu, histogram, component tree, multi-level segmentation	Fast and simple	Homogenous sea only
Shape and Texture	Mathematical morphology, region-growing, successive shape analysis	Robust with high accuracy	Many false candidates
Statistics	Principle component analysis	Fast	High knowledge of operator

The vessel-detection strategies listed in Table 2.8 will elaborated upon in chapter 5. These methods are combined into a three-step process to best extract vessels from images captured in the VIS-spectrum. Lastly, a common image-processing tool used to refine extracted binary regions is discussed in the following subsection.

2.7.1 Morphological Operators

Basic morphological operators is a collection of non-linear operations related to the shape of image features. These operators are suitable for binary images as they rely on the relative ordering of pixels. Furthermore, they rely on a *kernel* that is used to compare neighbouring pixels. The kernel's centre is placed over each pixel and either fits the image-segment if all the pixel-values correspond or hits (intersects) if at least one pixel-value correspond with the kernel's values. Consequently, the kernel's zero-valued pixels are ignored.

The fundamental operations are erosion and dilation and are depicted in Fig. 2.10. These figures are acquired with a 3×3 kernel of values 1; for illustrative purposes, values 1 and 0 are depicted as black and white, respectively. The compound operations are opening and closing of binary images and are depicted in Fig. 2.11. Opening is erosion followed by dilation, whereas closing is dilation followed by erosion, both operations using the same kernel. Opening removes slim connections between neighbouring pixels, whereas closing fills holes within a region whilst maintaining its size.

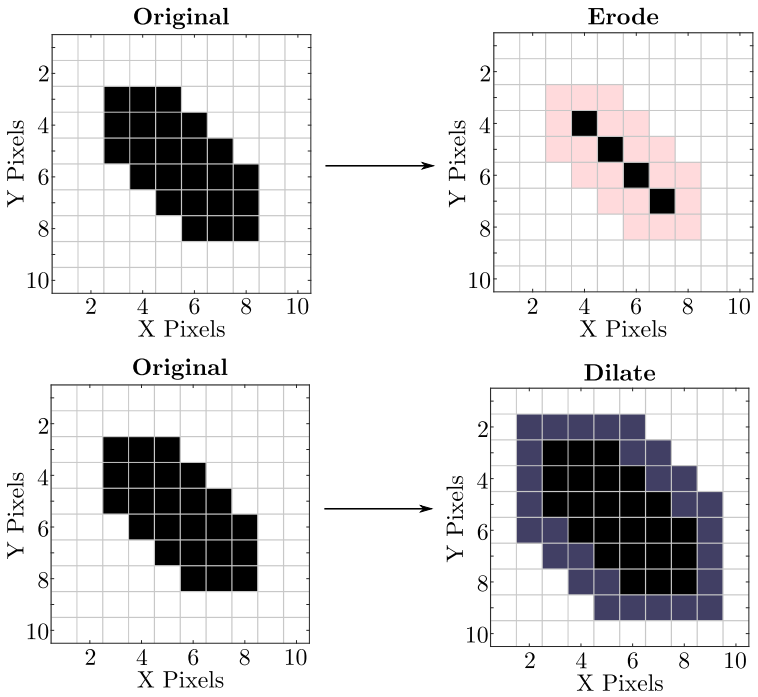

Figure 2.10: Fundamental morphological operators erosion and dilation using a 3×3 kernel. Red and blue highlighted pixels indicate removed and added pixels, respectively.

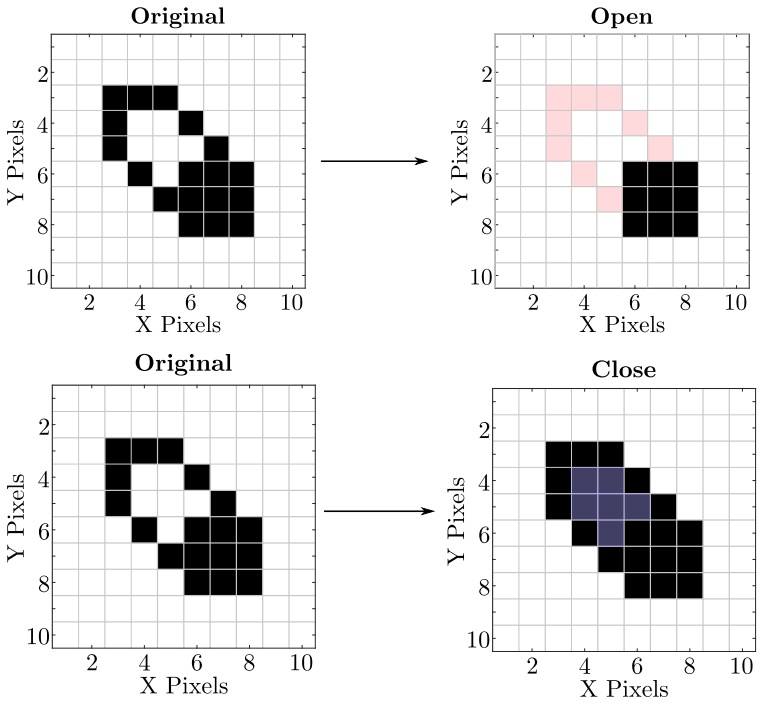

Figure 2.11: Compounded morphological operators open and close using a 3×3 kernel. Red and blue highlighted pixels indicate removed and added pixels, respectively.

3. Dataset Description

This thesis is based on real-world problems and, therefore, will require real data with which to base its solution. This chapter will elaborate on the datasets used necessary for the informed assumptions in this thesis. It introduces the AIS dataset, vessel heat-map, and satellite images.

3.1 AIS Dataset

In general, S-AIS data and services, such as searching online archives, are supplied at a cost. Therefore, AIS data is not easily accessible and the free data is limited. A 10.2 GB dataset, in addition to a Web Map Service heat-map, with courtesy of the CSIR, is used to conduct AIS feasibility tests, as further discussed in Sec. 4.4.

The raw NMEA data was decoded and converted to AIS-strings using an AIS decoder written by Arno Duvenhage [38]. The 10.2 GB dataset is divided into days ranging from 31st October 2017 to 14th March 2018. Each day was evaluated for continuous coverage and number of messages sent. The most active day to the author's discretion was chosen to be the 2nd November 2017 and will be used for the remainder of this thesis. The day consists of 717 vessels that broadcasted 1 465 036 messages. The data was parsed as per Fig. 3.1 to create vessel objects with which to run the simulations to be further elaborated on. The antenna models and bit error rates are discussed in Sec. 4.4

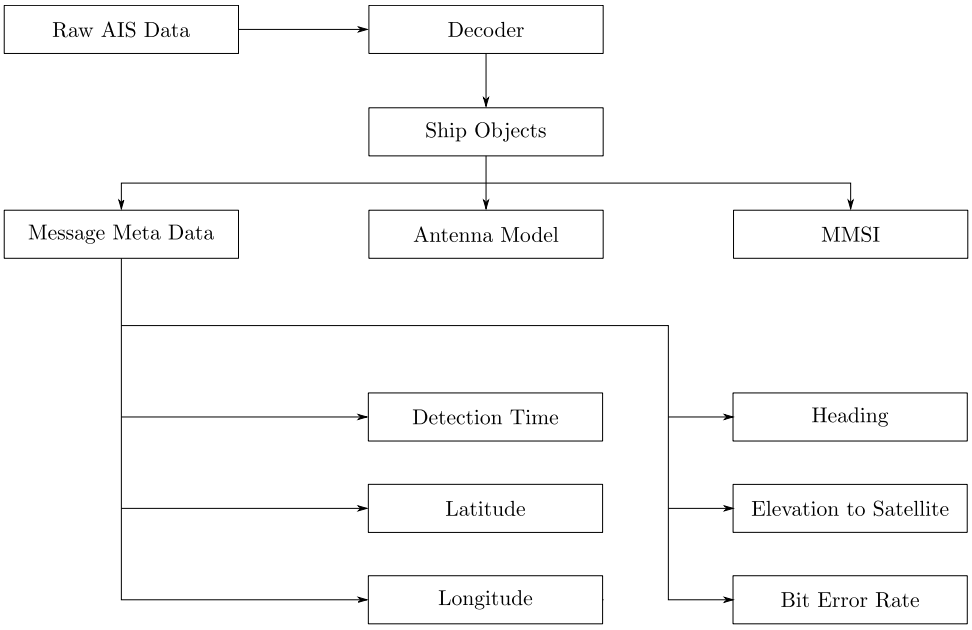

Figure 3.1: Data structure to which AIS data was parsed.

For the AIS dataset, it was found that 1 846 572 messages' types are identifiable and 69 797 corrupt because the decoder failed to decode the message. The message-type distribution is shown in Fig. 3.2 and for clarification, messages 24, 21, 27, 19, and 11 occurred 32 112, 9003, 954, 571, and 94 times. Furthermore, 585 079 of the messages do not transmit their heading.

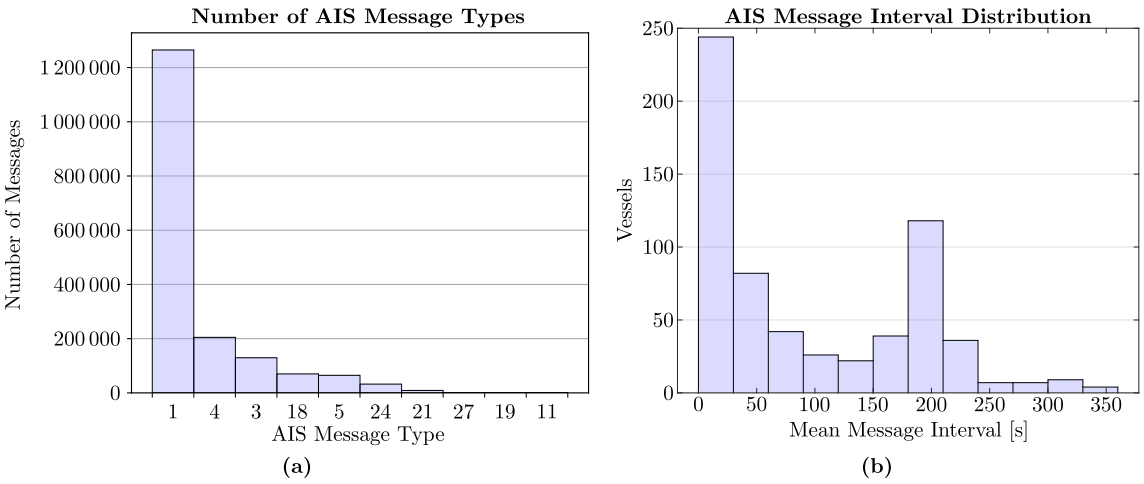

Figure 3.2: AIS Dataset description. **(a)** is AIS data types. **(b)** is the mean vessel AIS broadcasting interval for the selected dataset

The extracted data from each AIS message contains its MMSI, heading, longitude and latitude, and message type information. Further dynamic information that can be extracted is its navigational status, rate of turn, speed over ground, positional accuracy and course of ground. These parameters can be used to predict where vessels may be in the future and are deemed as future work. However, this will be required to identify where vessels will be in a remote image as it is unlikely that the vessels will broadcast during image acquisition.

No meta-data regarding the dataset is known but it is deduced that it is an S-AIS dataset because the coverage exceeds 72 km from SA's coast. The vessel's coordinates are grouped and depicted in Fig. 3.3 that indicates that vessel movements can be predicted with linear-interpolation. Furthermore, the vessels' reporting interval can be approximated by calculating the time difference between consecutive messages. This is used to generate the histogram depicted in Fig. 3.2b and it is evident that certain messages do not abide the NMEA interval-protocol of 2, 3.5, 6, 10, 180, 360 s intervals, as there is a distinctive peak in reporting intervals at 200 seconds. Moreover, it is more likely that messages are missing in the dataset. Furthermore, all vessels are required to transmit a compulsory static-position report (Message-5) every 360 s. Therefore, at least 172 000 Message-5's are expected, assuming that no spoofing occurs that results in 717 detected vessels. Notably, less than 100 000 of this message type is detected. Lastly, the peak at 200 s in Fig. 3.2b is due to anchored vessels broadcasting their positions every 180 s.

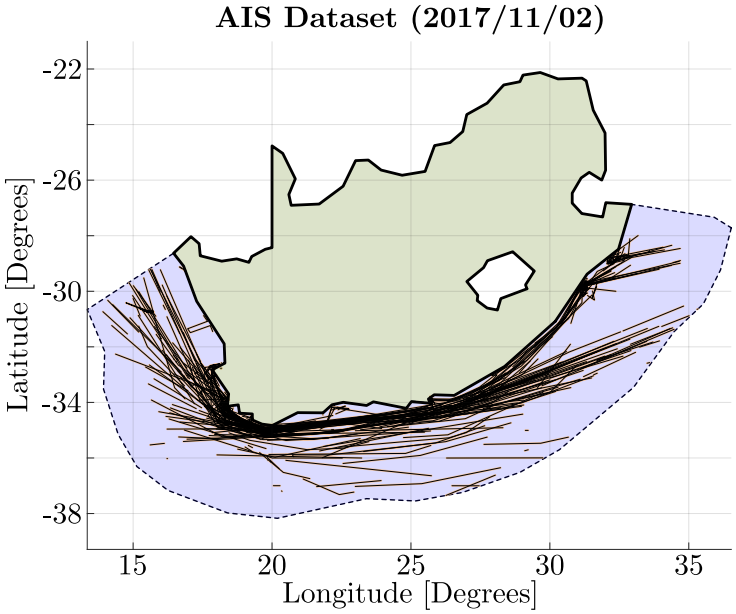

Figure 3.3: Vessel locations extracted from the AIS dataset by grouping them according to their MMSI numbers.

3.2 Satellite Images

The second part of this chapter will discuss the satellite images used to determine a satellite's pointing accuracy, band selection and vessel identification. Four different sources were grouped to make a dataset for this thesis and are listed in Table 3.1, where the satellite's ground sampling distance (GSD) will be further discussed in Sec. 4.2.3. This dataset mainly consists of RGB-images due to data availability of vessels and each respective satellite will be discussed in the subsections to follow.

Table 3.1: Satellite image dataset description where H and i is the satellite's respective altitude and inclination.

Satellite	***H***	***i***	**GSD**
SumbandilaSat	≈460 km	97.15°	6.3 m @ 500 km
nSight-1	380 km	51.6°	39 m @ 500 km
Sentinel-2	≈786 km	98.62°	20 m @ 500 km
ISS	400 km	51.6°	Dependent on Camera

Satellite images are prone to radiometric flaws caused by the curved shape of the Earth, absorbent atmosphere, variation in Sun illumination, and sensor imperfections that require images to be corrected. However, for this thesis, it is assumed that the images have already been corrected. Furthermore, this thesis will focus on passive sensors acquiring information from the EM bands in the microwave to the visible spectrum. It is assumed that active illumination sensors, such as synthetic

aperture radar is incompatible with 6U CubeSats due to their power requirements and will not be further discussed in this thesis.

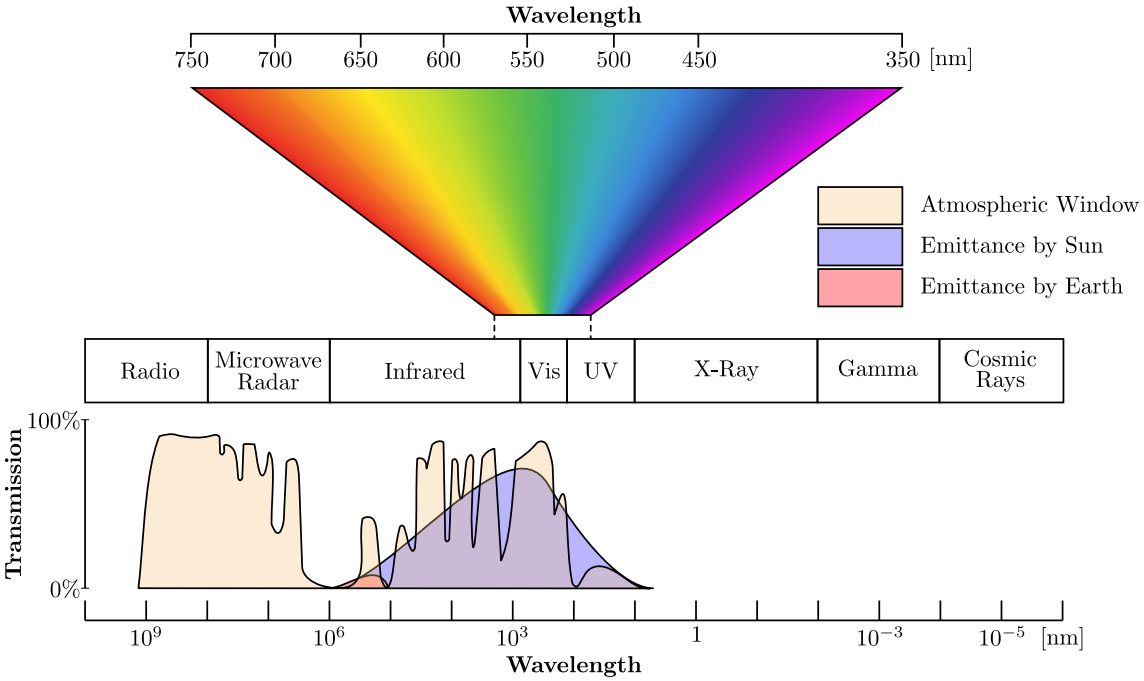

Figure 3.4: EM spectrum with each wavelength's respective atmospheric absorption adapted from [39].

The EM spectrum is depicted in Fig. 3.4, where the spectra names correspond with their respective wavelength windows and *VIS* and *UV* are shortened for visible and ultraviolet, respectively. Furthermore, the atmospheric window is the percentage that wavelengths get absorbed by Earth's atmosphere and can therefore not be sensed from space when its transmission is low. Passive sensors detect the Sun's reflected emittance from Earth. This is only possible when the satellite is not in eclipse. Lastly, imaging during an eclipse is possible due to the Earth' Emittance from its Black-body radiation, which is in the thermal infrared spectrum. Imaging during night-time is possible in the visible spectrum, however, the vessels are required to be well-lit. Furthermore, when capturing images in low-light conditions the camera's shutter speed has to be increased that can result in blurry images, in addition to the satellite's reduced pointing accuracy when in eclipse. The pointing Therefore, night-time imaging will not be further discussed in this thesis.

3.2.1 Sentinel-2

Sentinel-2 is the only dataset that contains multispectral data with its 13 EM bands and GSD summarised in Table 3.2. The images are captured by a constellation of two optical satellites with freely available data since December 2015. Furthermore, the satellites have a temporal resolution of five days at the equator and two to three days at mid-latitudes [37].

Table 3.2: Sentinel 2 multispectral instrument EM bands adapted from [40].

Band	λ [nm]	GSD	EM Band	Band	λ [nm]	GSD	EM Band
1	443	60 m	Violet	8	833	10 m	Infrared
2	492	10 m	Blue	8a	865	20 m	Infrared
3	560	10 m	Green	9	945	60 m	Infrared
4	665	10 m	Red	10	1374	60 m	Microwave
5	704	20 m	Infrared	11	1614	20 m	Microwave
6	741	20 m	Infrared	12	2202	20 m	Microwave
7	781	20 m	Infrared				

Fig. 3.5 is an enlargement of the vessel highlighted in Fig. 2.9, showing only the bands of 10 m and 20 m GSD, as its difficult to identify vessels in 60 m GSD images. As the wavelength increases the sea clutter and effects from precipitation decrease whilst the vessel become more clear. Conversely, at the lowest wavelength, the vessels' wake is most prominent which can be used for orientation estimation. Generally, CubeSats cannot capture images of wavelengths larger than 1000 nm when inspecting imagers such as the Gecko or HyperScape100 imagers, the latter being discussed in Sec. 4.2.3.

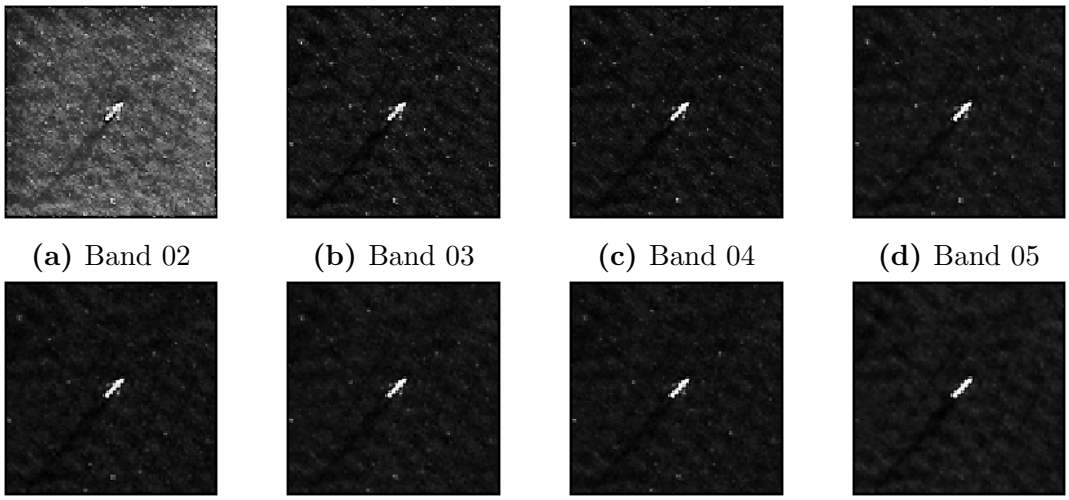

(a) Band 02 **(b)** Band 03 **(c)** Band 04 **(d)** Band 05

(e) Band 06 **(f)** Band 07 **(g)** Band 8A **(h)** Band 11

Figure 3.5: Vessel extracted from Sentinel-2 image `T36JTL_20190429T073621` to illustrate vessel clarification in different EM bands.

A microwave imager would be ideal as Band 11 in Fig. 3.5 has less sea clutter. Unfortunately, is not realisable onboard a CubeSat. Nor is thermal infrared as it has to be kept cool and will be very demanding on the CubeSat's power budget if it has to survey the EEZ, further discussed in appendix B.5. Therefore, for the remainder of this thesis, images captured in the visible spectrum will be assessed.

3.2.2 SumbandilaSat

SumbandilaSat was developed by Sun Space and Information Services (SunSpace) and Stellenbosch University and launched in 2009 [41]. For this thesis, two of its images, in addition to its attitude determination and control system's (ADCS) log used to determine its pointing accuracy, are used. The images are false-colour and mixed to produce a red, green and blue (RGB) image that is JPEG-compressed. Consequently, image detail will be lost; it will be used to build vessel-extraction algorithms on as its images contain the most candidates, compared to images from the sources listed in Table 3.1 which will be further discussed in chapter 5. Furthermore, the ADCS log will be discussed in appendix A.

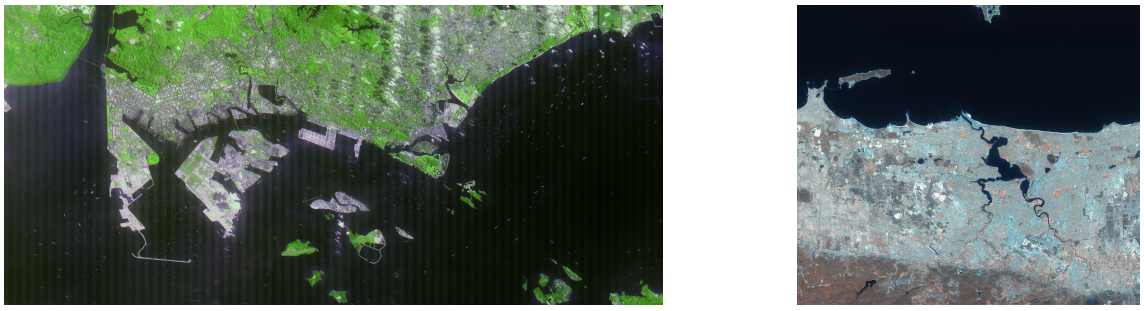

(a) **(b)**

Figure 3.6: SumbandilaSat remote sensed images. **(a)** is sensed of Singapore on 2nd March, 2010 and **(b)** is sensed of Perth on 17th November 2010.

3.2.3 nSight-1

nSight-1 is a nano-satellite designed and built by SCS Space and was launched in 2017. Its images were supplied with the courtesy of SCS Space in .raw format; no data is lost due to compression. Therefore, the developed algorithms could be compared to RGB images that are colour-corrected and false-colour. The images are sensed using a Bayer colour pattern and the pixels have to be mosaic filtered to acquire an RGB-image which will not be discussed in this thesis. The mosaic filtering adds a blur to the image, effectively slightly degrading its GSD. The resultant 2048×1088 images used for this thesis are displayed in Fig. 3.7.

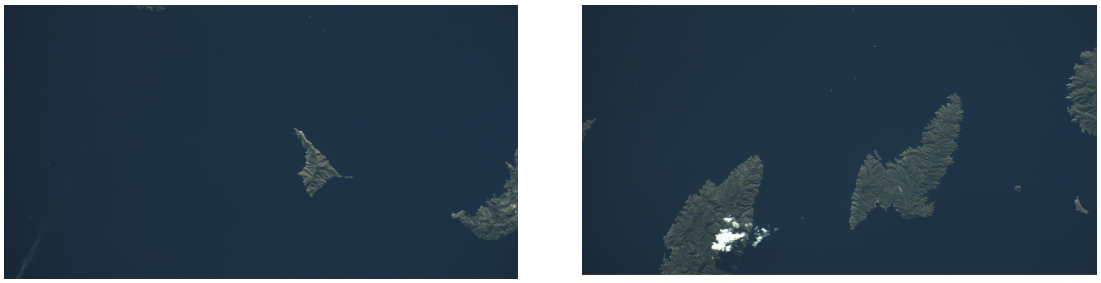

(a) **(b)**

Figure 3.7: nSight-1 Images

Table 3.3: Images captured from astronauts onboard the ISS. The ISS's altitude is denoted h_p. The camera's physical pixel size, focal length, and effective aperture are denoted d, f, and D, respectively. The sun-angle and camera's tit angles are denoted ε_S and η, respectively. The image's GSD is denoted X.

N	h_p [km]	d [μm]	f [mm]	D [mm]	ε_S	η	X [m]
a	407	6.4	500	45.5	51°	39°	6.85
b	406	7.3	170	7.7	7°	22°	18.90
c	407	7.3	170	5.4	52°	33°	21.13
d	419	7.3	500	50	48°	29°	7.07
e	419	7.3	500	50	47°	22°	6.63
f	419	8.45	400	80	74°	53°	15.68
g	354	3.45	400	50	20°	53°	5.35

3.2.4 ISS Satellite Images

Images captured of Cape Town, SA were acquired through NASA's ISS remote sensing portal. These images are captured by astronauts on board the international space station (ISS) using the electronic cameras Nikon D3S, D4 and D5 and a Kodak K760C. The images chosen for this thesis are such to best represent different scenarios: clear, cloudy, dark, sunglint, complex sea states with some containing vessels. Unfortunately to the author's knowledge, no images are captured of the open ocean surrounding SA's coast.

The ISS images are depicted in Fig. 3.8 with their respective specifications listed in Table 3.3. The respective images will be used in Sec. 5.3 for:

a, **d-f**: vessel detection,
b: land-masking,
c: non-vessel rejection,
g: night-time land-masking

Each camera has a different pixel sensor size on its image plane and focal length. The effective aperture is calculated as each image's F# is supplied with each image as part of the camera's meta-data. Consequently, Eq. (4.3) is used to calculate each image's GSD and is listed in Table 3.3.

(a) ISS055-E-6893

(b) ISS052-E-2625

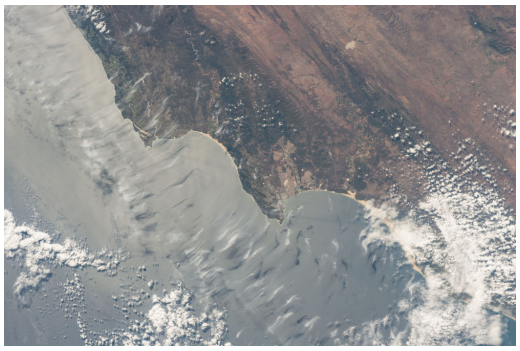

(c) ISS050-E-11672

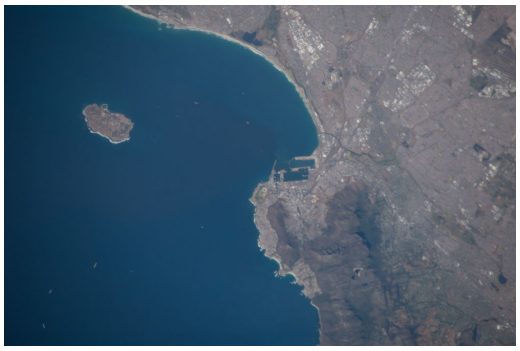

(d) ISS042-E-24792

(e) ISS042-E-24794

(f) ISS038-E-15450

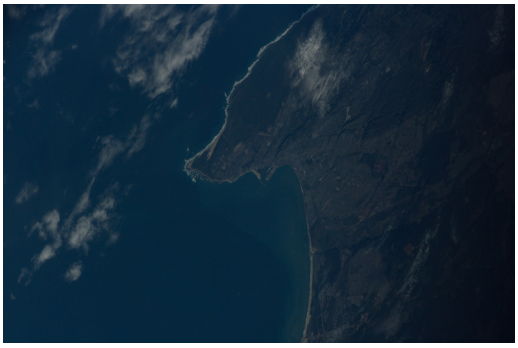

(g) ISS011-E-9748

Figure 3.8: Image courtesy of the Earth Science and Remote Sensing Unit, NASA Johnson Space Center. Each respective image's caption refers to a unique image's mission-roll-frame and can be acquired from `https://eol.jsc.nasa.gov`.

4. Simulation Environment

This chapter will discuss Earth coverage (EC) and elaborate on different techniques used to assess Earth observation (EO) orbits. A simulation environment is required to evaluate candidate orbits' EO, in addition to their AIS reception feasibility. The chosen simulation environment is the SGP4-model as described in Sec. 2.6.1. Furthermore, SGP4 will be used to simulate fictitious satellite constellations with ballistic coefficients of zero, assuming that the satellite will use propulsion to continuously correct its orbit and is further elaborated upon in appendix B.6.

EC refers to the area that a satellite's payload can sense over a period, whereas the instantaneous field of view (FoV), or footprint, is the area that the payload is sensing. Sensing refers to data that the payload can capture within its FoV. The AA is the area that could potentially be sensed by rotating the satellite to potential targets. Consequently, its AA will always lie within its FoV, as depicted in Fig. 4.1, with the AA the red area within the blue FoV.

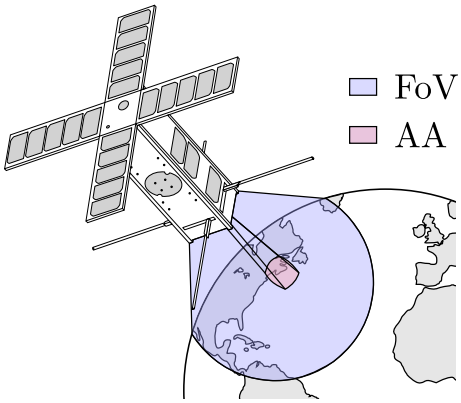

Figure 4.1: Exaggerated satellite's field of view within its access area.

It should be noted that EC is not a statistical quantity as a satellite's consequent time-steps are correlated [27]. Therefore, statistical data is generated from simulations and the results should be analysed to ensure that it does not misrepresent the actual EC. Lastly, analytical approximations should be used in conjunction with the simulations to aid its results and to identify possible EC patterns.

The simplest approach for analysing coverage patterns is by generating ground track plots using the SGP4-model, which entails connecting consecutive SSP, as depicted in Fig. 4.2. Thereafter, the simulation's coverage histograms can be investigated to identify coverage patterns by adding time as a dimension to ground track plots, which is depicted in Fig. 4.3. The analytical expressions are discussed in Sec. 4.2.5.

4.1 Engine Description

This section will elaborate on the methodology used to generate EC results. An SGP4-model, written in C as a MATLAB S-function, is used to determine a satellite's position at any time, given its TLE. The used software is an adaptation, written by Prof. W.H. Steyn, of freely available software from Celestrak [42] that are overlaid on accurate representations of the SA EEZ [43]. Therefore, it is used to calculate access times and coverage areas given a satellite constellation.

In this thesis the epoch is chosen as 12h00 6$^{\text{th}}$ August 2018 for local SA time (GMT+02h00), or 1 533 549 600 in Unix time. Satellites are simulated by generating their TLEs and calling an SGP4-routine to acquire their geodetic coordinates. The other SGP4 parameters, described in Sec. 2.6.1, are generated as required for different scenarios and will be specified in the thesis where necessary. Finally, the satellite's information is requested at each second, or time-step t_{step}, after the aforementioned epoch to emulate the satellite's motion.

Simulating a constellation of satellites for a prolonged period generates a vast amount of data. Therefore, to improve on the simulation's execution time, its time-steps are varied depending on the SSP's distance from the SA EEZ as:

$$t_{\text{step}} = 1 + \left\lfloor \exp\left(\frac{d_{min}}{740}\right) \right\rfloor$$

Where d_{min} is the distance in kilometres to whichever EEZ is closest to the SSP and it is calculated as expressed in Eq. (4.2) with auxiliary Eq. (4.1), where φ_{gc} and λ denote a coordinate's geodetic latitude and longitude, respectively. Furthermore, the number in the subscript denotes the respective coordinate. It was chosen for t_{step} to increase exponentially relative to double the distance that an EEZ extends into the ocean of 370 km, as it was empirically found that smaller values resulted in too large time-steps, with 1 s being the smallest time-step. The varying time-steps are depicted in Fig. 4.2 as the • markers on the ground track plot.

$$\alpha = \sin^2 \frac{\varphi_{\text{gc},1} - \varphi_{\text{gc},2}}{2} + \cos \varphi_{\text{gc},1} \cdot \cos \varphi_{\text{gc},2} \cdot \sin^2 \frac{\lambda_1 - \lambda_2}{2} \tag{4.1}$$

$$d = 2R_{\oplus} \arctan \frac{\sqrt{\alpha}}{\sqrt{1-\alpha}} \tag{4.2}$$

Given a number of satellites, the program will calculate the angular spacing between satellites such that they form a *string-of-pearls* configuration as follows:

$$\Delta\omega = \frac{360^\circ}{\#\text{satellites}}$$

Which will maximise its EC at the compromise of the satellites potentially not having interlinked communications with a smaller effective swath-width. Alternatively, the

satellites can be flown in a trailing formation to augment a satellite with a wider swath-width and to increase data-integrity as certain areas can be imaged in quick succession.

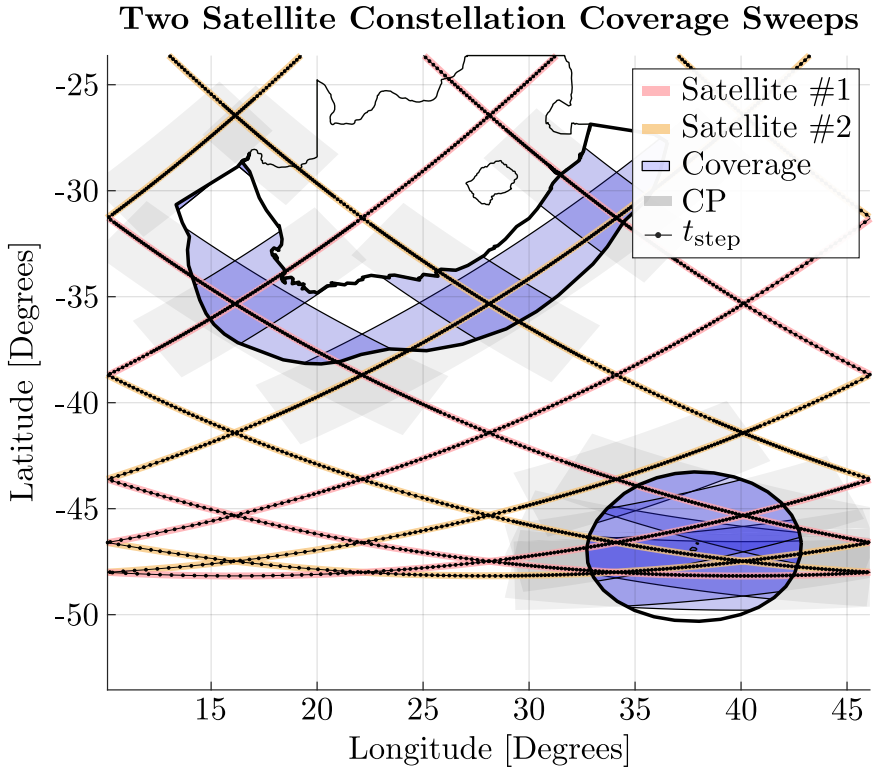

Figure 4.2: SGP4 coverage simulation example using two satellites phased 180° from each other in the same orbital plane.

A TLE is generated for each satellite in the constellation that is then parsed to the SGP4-routine. Upon completion, the results are augmented as a single satellite to determine its coverage and histograms, as expressed in algorithm 4.1. This algorithm is used to generate the coverage polygons as a subset of the EEZ for all SSPs denoted $\{\text{SSP}_1, ..., \text{SSP}_\text{N}\}$, as depicted in Fig. 4.2. This is the resultant coverage for a two-satellite constellation is calculated as a subset of its cumulative AAs that is calculated using λ, which is acquired using Eq. (2.4) with a look-angle of 20°. Lastly, each respective satellite's ground track highlighted using a red and yellow tint.

The coverage is indicated with an opaque blue polygon with the darker regions more frequently sensed. Each time-step is indicated with a • and can be seen that the further the satellites move from the EEZ the larger the time-steps become. The bold and dashed lines signify satellites one and two, respectively. Finally, the course coverage-sweeps, denoted CP, are used to calculate the coverage polygons and are indicated using light-grey polygons.

Referring to algorithm 4.1, the rotation-matrix denoted `DCM`, described in appendix A, is used to create the imager's FoV by rotating the SSP about the Earth's centre or-

thogonal to the satellite's velocity vector, in a 2-D plane. The satellite's velocity vector is acquired by the double cross-product expressed in algorithm 4.1 to acquire points $\boldsymbol{p}_1$ and $\boldsymbol{p}_2$. The SSP at each time-step, denoted SSP_n, contains the satellite's geodetic latitude and longitude coordinates. The `sweep`-polygon is the set containing all the satellite's AAs as the satellite comes within range of the SA EEZ. These course polygons have to be refined by intersecting them with the SA EEZ to form a subset of the EEZ. Furthermore, Algorithm 4.1 stores all the `coast`-values to generate coverage histograms, which will be discussed in Sec. 4.2.1. The coverage polygon is used to calculate the coverage area on the projected plane.

The algorithm returns all the coverage polygons, denoted `coverage_polygons`, in geodetic coordinates, where the MATLAB functions used in algorithm 4.1 are described as follows:

- `min` - the minimum value of an array,
- `arclength` - the arc-length between two geocentric spherical coordinates,
- `flip` - reverses the indexing of an array,
- `intersect` - finds the locations where polygons intersect, and
- `inside` - returns `True` if a coordinate lies within a polygon.

4.2 Numerical Analysis Factors

This section will elaborate on all the factors considered for the simulation environment to best represent EC. The following factors were considered for this environment and will be elaborated upon in the subsequent subsections to follow:

1. Local imaging time,
2. Coverage area,
3. Look-angle to calculate AA,
4. Simulation time, and
5. Initial inspection.

4.2.1 Time of Pass for Imaging Purposes

As this thesis is considering passive imaging in the visible EM band, the FoV has to be illuminated by the Sun. Consequently, it is assumed that during worst-case conditions daytime occurs between 07h00 and 17h00 as the SA Winter solstice is roughly from 6h55 until 17h24 and that images acquired during this time can be processed to achieve sensible results. A coverage histogram is a means of describing the access frequency in addition to expressing the time at which the satellite will sense the targetted area, which is important for imaging-needs. Furthermore, if the

Algorithm 4.1: Returns a satellite constellation's EC given the number of SSPs (N), altitude (H), SSP's longitude (θ) and geocentric latitude (ϕ_{gc}), and look angle (γ).

Input: SSP (ϕ_{gc}, θ), γ, H, N, EEZ
Output: coverage_polygon

$\lambda \leftarrow \frac{\pi}{2} - \gamma - \arccos\left(\frac{\sin\gamma(R_\oplus + H)}{R_\oplus}\right)$;
coast $\leftarrow$ **False**;
$i \leftarrow 0$;
for $n \leftarrow 1$ **to** $N - 1$ **step do**
  if min(arclength(SSP$_n$, EEZ))$/R_\oplus < \lambda$ **or** SSP$_n$ **inside** EEZ **then**
    coast $\leftarrow$ **True**;
    $\mathbf{u}_n \leftarrow [\cos\phi_{gc,n}\cos\theta_n \;\; \cos\phi_{gc,n}\sin\theta_n \;\; \sin\theta_n]^T$;
    $\mathbf{u}_{n+1} \leftarrow [\cos\phi_{gc,n+1}\cos\theta_{n+1} \;\; \cos\phi_{gc,n+1}\sin\theta_{n+1} \;\; \sin\theta_{n+1}]^T$;
    // DCM returns spherical coordinates with geodetic latitude
    $\mathbf{p}_1 \leftarrow \mathrm{DCM}\,[\mathbf{u}_n \times \mathbf{u}_{n+1} \times \mathbf{u}_n, \lambda]$;
    $\mathbf{p}_2 \leftarrow \mathrm{DCM}\,[\mathbf{u}_n \times \mathbf{u}_{n+1} \times \mathbf{u}_n, -\lambda]$;
    if $\mathbf{p}_1$ **above** SSP$_n$ **then**
      $P_{\text{upper},\,i} \leftarrow \mathbf{p}_1$;
      $P_{\text{lower},\,i} \leftarrow \mathbf{p}_2$;
    else
      $P_{\text{upper},\,i} \leftarrow \mathbf{p}_2$;
      $P_{\text{lower},\,i} \leftarrow \mathbf{p}_1$;
  else if coast **then**
    coast $\leftarrow$ **False**;
    $i \leftarrow i + 1$;
for $n \leftarrow 1$ **to** $i - 1$ **do**
  sweep $\leftarrow$ polygon(P_{upper}, flip(P_{lower}), $P_{\text{upper},\,1}$);
  coverage_polygon(n)$\leftarrow$intersect(sweep, EEZ)

orbit under consideration is not a Sun-synchronous orbit (SSO), the local access time has to be calculated (SSO to be discussed in Sec. 4.3.2). This is achieved by keeping track of when the satellite senses the EEZ depending on how much time has passed.

A 24-hour coverage histogram of a satellite constellation with a 500 km altitude and 48° orbit inclination is depicted in Fig. 4.3. The histogram has a *high* value when it senses the coast and night-time is shown as a grey area fitted onto the histogram. The wider the histogram is, the longer the satellite senses the coast.

These plots are used to compare orbits and assess the passed time for subsequent

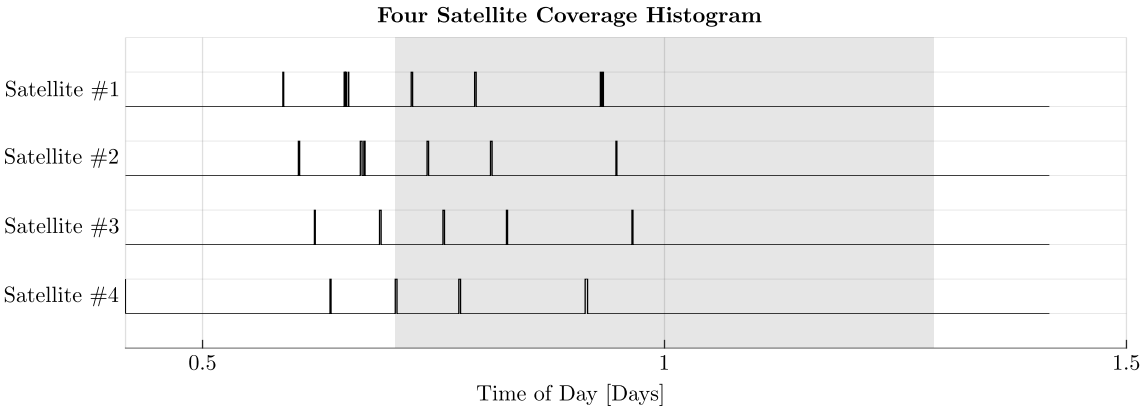

Figure 4.3: Four satellite constellation coverage histogram.

passes. Therefore, these plots are used in conjunction with the ground track plots depicted in Fig. 4.2 to add time as a dimension. Foremost, this can be improved upon by calculating the sunglint angle relative to the satellite's position as the Sun's coordinates is known; it will not be discussed in this thesis. Lastly, the simulation is required to run for longer than the satellite's repeat cycle, denoted by the astronomical Capricornus $T_{\mathcal{C}}$, to get an accurate representation of the coverage plots. This cycle is the period for the constellation to be in the same illumination conditions.

4.2.2 Coverage Approximations

The polygons of SA and EEZ [43] are high resolution and, therefore, contain redundant information. To improve simulation execution time, the excess points are removed by simplifying the polygons using the Douglas Peucker (DP) algorithm; in MATLAB called the `reducem` function. The algorithm is called with a threshold of $\varepsilon_{\text{DP}} = 0.1°$, which is the maximum arc-angle a point may lie from a line.

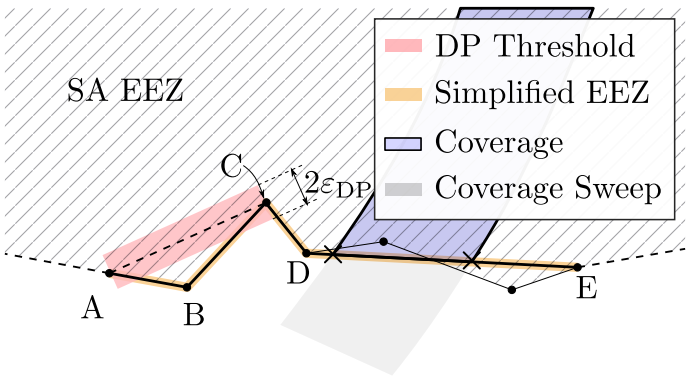

Figure 4.4: Simulation area inaccuracies cause by line simplification.

This process is depicted in Fig. 4.4, where the DP threshold and the simplified line is indicated with a red boundary and yellow highlight, respectively. The DP algorithm starts by adding the first and last points, denoted A and E, to the new line. Then,

it draws a line between them and searches for the point furthest away from this line, in this case, it is point C. It then removes all the points the lies within ε_{DP} from said line. The process is repeated until all the points that do not meet the criterion is removed. After which, the final simplified line, ABCD, is indicated with a bold line that has a yellow highlight in Fig. 4.4.

The coverage sweep's intersection with the EEZ, shown in Fig. 4.4 as two $\times$-symbols, is determined using a MATLAB function `InterX`, written by NS Imperial College London in 2009. Given two curves, defined by points, it returns the intersection coordinates. It is assumed that the high-resolution polygon contains errors and that simplifying the EEZ will result in a negligible error. However, it will have a slightly different resultant coverage polygon as the intersection is calculated by means of linear-interpolation and the coverage has a slight curve.

Finally, the coverage area is calculated by using the MATLAB function `areaint` from the Mapping Toolbox. It uses Green's Theorem on the surface enclosed by the coverage polygons, which will not be discussed in this thesis. The returned area is in kilometres and the function requires the polygon's latitude and longitude coordinates, in addition to the Earth's radius. For this calculation spherical Earth is assumed with its equatorial radius, $R_{\oplus} = 6378.137\,\text{km}$, as SA is relatively close to the equator.

Consequently, the coverage area is not precisely accurate given the input polygons. However, as seen in Fig. 4.4, the difference is deemed negligible, considering that it will be used for EC comparisons. It should be noted that access times will be a second shorter due to the line-simplification. Therefore, it can be assumed that this simulation delivers worst-case results.

4.2.3 Satellite Roll Angle

The satellite look-angle was determined by the maximum allowable GSD degradation. The GSD is calculated as a function of a camera's quality factor:

$$Q = \frac{d}{d'} = \frac{X}{X'}$$

That describes the ratio between the first minimum on the image plane's light response and the physical pixel size. The quality factor, Q, should ideally be one, indicating that the physical pixel sensor size, d, lines up exactly with the first minimum's diameter, d'. Furthermore, X is the GSD and X' is the diffraction-limited ground, or spatial, resolution.

A simplified camera model is depicted in Fig. 4.5 that illustrates diffraction that occurs when a circular aperture is used. The impulse response induced onto the image plane is illustrated as a *sinc* function, where the distance between the first minimums are denoted as d'. The physical pixels are illustrated using bold, black lines with the pixel size denoted d. Furthermore, f, D, h, X', and θ_r are the

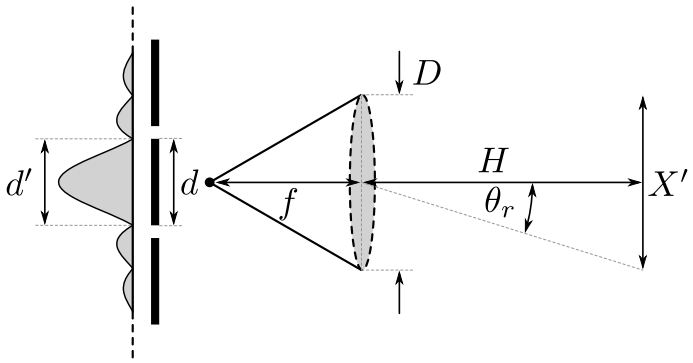

Figure 4.5: Circular aperture light response on a camera's image plane.

camera's focal length, lens diameter, the distance between the lens and source of light, diffraction-limited ground resolution, and the Rayleigh diffraction criteria, respectively.

For this thesis, the *Simera Sense HyperScape100* camera's will be used on which to base initial assumptions for the simulation, as it is a commercial-off-the-shelf product that is locally produced in SA with readily available specifications. This camera is ideal for CubeSats as it fits inside of a 3U satellite with the dimensions being $98 \times 98.4 \times 170$ mm^3 and the relevant specifications listed in Table 4.1. The *Gecko* imager, manufactured by SCS, is a viable option and was also considered.

Table 4.1: Simera Sense HyperScape100 camera specifications, adapted from [44].

Parameter	**Value**
GSD @ 500 km	4.75 m
Cross Track Pixels	4096
Number of bands	154 covering 470 nm–900 nm
Pixel Depth	8 or 10 bit
Focal Length	580 mm
Aperture Diameter	94.8 mm
Pixel Size	5.5 µm

The GSD will degrade when the satellite points off-nadir, where the maximum look-angle is governed by the maximum allowable GSD degradation. The specifications listed in Table 4.1 is used as a ground truth. This is used to calculate the maximum look-angle as the GSD degradation can be calculated as expressed in Eq. (4.3), where λ is the wavelength being captured and H is the satellite's altitude.

By using a worst-case wavelength of 900 nm and an altitude of 493.2 km, the GSD degradation is calculated as a function of the satellite's look angle, using Eqs. (2.1) to (2.5) to calculate H. Consequently, the percentage GSD degradation is calculated

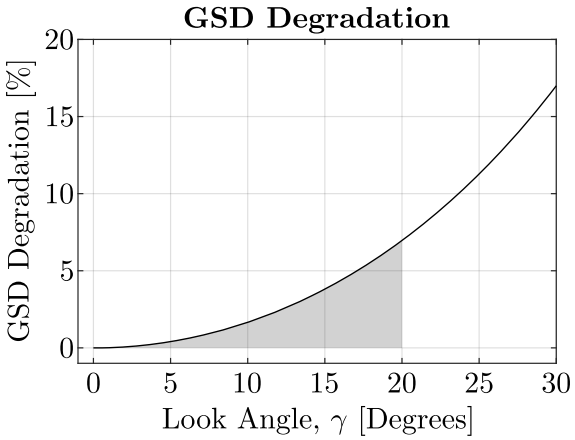

Figure 4.6: Degradation of a satellite's GSD as it points off-nadir.

as:

$$\xi_{\text{GSD}} = \frac{X - X_0}{X_0}\%$$

And is displayed in Fig. 4.6. Therefore, the maximum allowable look-angle for the thesis is assumed to be 20°; the GSD has an acceptable degradation of 5%.

$$X = 2.44\frac{H\lambda}{D} \cdot \frac{d}{2f\tan\theta_r} \tag{4.3}$$

Lastly, the GSD needs to be kept from exceeding this limit, as look-angles larger than 20% tend to exponentially degrade the GSD. This will result in image-processing algorithms failing when introduced to GSDs they are not programmed to process.

4.2.4 Simulation Time

The SGP4-model becomes inaccurate when one wants to predict a satellite's future location. This is because the model is not complex enough to compensate for the satellite's motion when introduced to atmospheric drag and solar radiation pressure. This can be tested by comparing a satellite's TLEs that are two weeks apart and will not be discussed in this thesis. However, the satellites' B^* is set to zero to disregard perturbations caused by solar radiation pressure and atmospheric drag, under the assumption that the satellite will continuously correct its orbit. Additionally, this assumes that the satellite has large enough propulsion-budget to maintain its orbit, which will further be discussed in appendix B.6.

Furthermore, if the simulation has a short duration and starts with the satellite sensing the EEZ, the results will reflect a much better coverage and not be an actual representation of the EC. Therefore, the number of days has to be chosen such that it is roughly an integer multiple of the orbit's repeat cycle, $T_{\circlearrowleft}$. This will ensure that parts from the start and end of a simulation will not bias the results. For this thesis, the elaborate comparisons are done on more than 100 days.

Lastly, the orbital perturbations induce harmonics onto the orbit that might cause the satellite to never observe certain areas in the world, such as with the specialised orbit discussed in Sec. 4.3.3. This will result in the simulation outputting zero coverage Therefore, the ground track has to be inspected to identify such an orbit and the nodal regression has to be changed to shift the ground track towards the areas under inspection so that they are sensed.

4.2.5 Initial Inspection

The aforementioned factors have to be taken into consideration when defining an initial parameter range on which to run tests. The last consideration is an analytical expression conveyed in Table 4.2 [27], where φ is the target-locations geocentric latitude, γ is the satellite's look-angle, and i is a circular orbital plane's inclination angle. It expresses the percentage coverage for a specific geocentric latitude-band, given an orbital inclination angle. The latitude band is varied from 0° to 90°, effectively moving the band under inspection from the equator to one of the poles. This is used to identify an orbital inclination best suited for surveying SA's EEZ. When assessing EC, there will be many consecutive orbits that provide coverage followed by a gap with no coverage, called a dark gap (DG), with a specific repeat-cycle.

Table 4.2: Percentage EC given a target's latitude (adapted [27]).

Latitude Range	**Coverage Regions**	**Percentage Coverage**
$\varphi > \gamma + i$	0	0
$i + \gamma > \varphi > i - \gamma$	1	$\varphi_1/180°$
$i - \gamma > \varphi > 0$	2	$(\varphi_1 - \varphi_2)/180°$

Furthermore, each latitude band has a discrete set of possible coverage patterns [27]. The ε angle restriction is based on the assumed minimum elevation for successful radio-communication, which will be elaborated upon in Sec. 4.4. The angles φ_1 and φ_2 are the negative and positive signed angles, respectively, and are calculated as:

$$\cos \varphi_{1 \text{ or } 2} = \frac{\pm \sin \gamma + \cos i \sin \varphi}{\sin i \cos \varphi}$$

The resultant percentage coverage described in Table 4.2, is depicted in Fig. 4.7. The two orbits being evaluated is of inclination 39° and 48° with an altitude of 500 km, respectively. The 39° orbit is depicted with a blue tint, whereas the radio communication coverage is depicted with dashed lines and the payload's FoV coverage percentage with a solid line.

The chosen altitude is based on CubeSats generally being launched into 400 km–650 km altitude orbits. Furthermore, the inclination angles are based on the minimum achievable angle using the Electron Rocket, described in Sec. 2.6.1, and an angle best suited for observing the entirety of the EEZ. This angle is acquired by

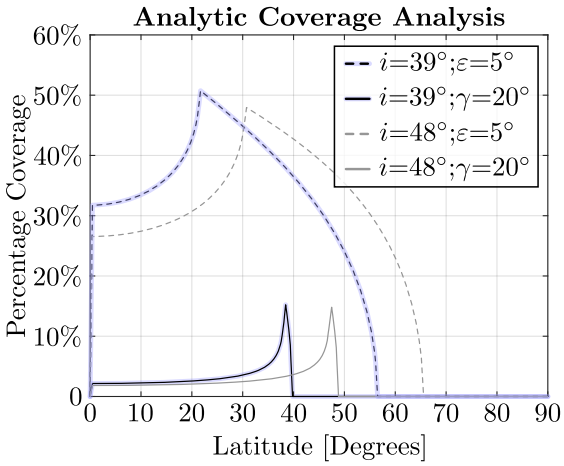

Figure 4.7: Analytic coverage analysis of SA's EEZ.

the lowest absolute latitude of the EEZ, roughly 50°, minus 2° which is roughly the Earth angle of the satellite orbiting at an altitude of 500 km with a look-angle of 20°, as per Eq. (2.4).

Given the aforementioned orbital parameters, it is shown that at least 50% of the orbits will be able to detect AIS-signals in the SA EEZ, under the assumption that the messages are detectable above an elevation of 5°, which is further discussed in Sec. 4.4. Furthermore, the 39° orbit is ideal for imaging the SA mainland EEZ, although the island-archipelago will be excluded. As such, an inclination angle of 48° is chosen to include the entirety of the EEZ. Lastly, even though the satellites can communicate with the EEZ for nearly half of their orbits, due to their narrow looking angle's they will only be able to sense the coast for 15% of their orbits.

The number of satellites correlates strongly with the EC. As this thesis assumes string-of-pearls formation flying, the number of satellites required for interlinked communication is dictated by the altitude, H, given N number of satellites and is described as:

$$H \geq \frac{R_{\oplus} + \varepsilon_H}{\cos\left(\frac{180^\circ}{N}\right)} - R_{\oplus}$$

Where ε_H is the desired distance above Earth's surface for the communication link, chosen as 50 km. If ε_H is too small, signals will be heavily attenuated by the atmosphere. As a rough estimate, interlinked satellite communication is possible for eight or more satellites at an altitude of 500 km.

After the analytical orbit analysis, a parameter sweep is implemented using the developed simulation environment. It was decided to keep the number of simulation days constant at 10 days, a nodal regression of 0°, and to use the epoch specified in Sec. 4.1, whilst sweeping the following parameters:

1. Number of satellites in the constellation,

2. Orbital inclination angle, and

3. Orbital altitude.

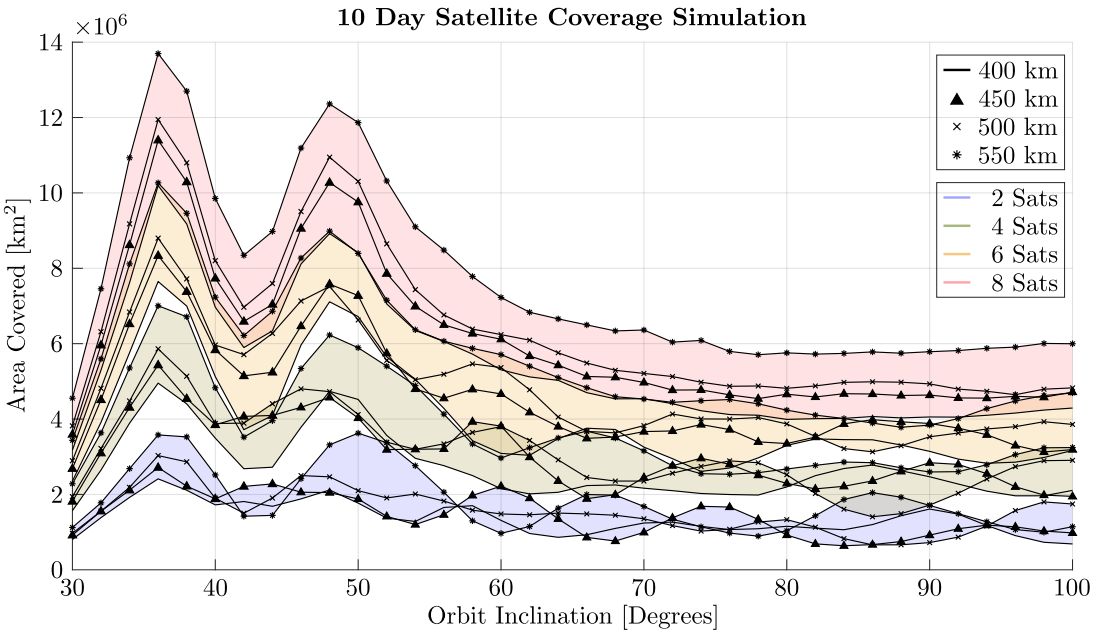

Figure 4.8: Parameter sweep of the coverage simulation.

The metric on which to compare the orbits is chosen as the total of AA covered in square kilometre with a look-angle of 20°. The results are depicted in Fig. 4.8, where the number of satellites is colour-coded and the altitudes are denoted using line-markers. Evidently, an orbital inclination of 39° will result in more than double the coverage when compared to an orbit with an inclination angle of more than 70°. Furthermore, the area coverage at 48° also peaks as the satellites sense the archipelago. It should be noted that at 39° the satellite will only observe the mainland EEZ and, therefore, the coverage at 48° is divided between the mainland's and archipelago's EEZs. However, at 48° the satellite will also sense the archipelago more than the mainland EEZ because the satellite has the longest access to an area at its turning points, where it goes from descending to ascending or vice versa, especially when it is a prograde orbit. As this point moves away from the mainland EEZ between 39°-46°, the coverage decreases. Finally, when reaching 47°-50° the coverage is similar to that of 39° taking into consideration that the archipelago is sensed for the majority of the time. Therefore, the mainland EEZ is not surveyed as frequently as with a 39° orbit.

As the inclination angle increases, the coverage remains constant. The only beneficial inclination after the aforementioned angles is at $\approx 97°$ that will result in an SSO. Additionally, as the orbital altitude increases, the coverage marginally increases whilst the GSD decreases as governed by Eq. (4.3) under the assumption that the CubeSat remains unchanged.

Finally, it is shown the number of satellites correlates with the EC. Consequently, this number will be dictated by the launch vehicle and the mission budget. The approximate EC for the number of satellites is depicted with red, orange, green, and blue shades for eight, six, four, and two satellites, respectively. The reason why there is uncertainty in the range is regarding the number of simulation days and the initial nodal regression. The mean of each distribution can be regarded as the general coverage.

4.3 Orbit Comparison

Based on the previous subsections, three orbits were chosen for inspection namely:

1. An orbit resembling the aforementioned qualities of an altitude of 500 km and inclination angle close to 50°,
2. A SSO that is generally chosen for EO, and
3. A specialised EO orbit similar to the first option that revisits specific areas on Earth.

These orbits will be elaborated upon and compared in the subsections to follow. The first orbit's inclination angle is chosen as 51.3° because it is the plane in which the ISS orbits that is good for EO, from this point onwards referred to as the ISS orbit. This orbital inclination angle allows for the satellites to maximise the amount of land they observe. The second orbit will be called the SSO and the third will be called the repeat ground track (RGT) orbit, which will be discussed in Sec. 4.3.3. An altitude of 500 km was chosen for this thesis as it delivers good coverage, allows for a good GSD using a 6U satellite, will have a longer lifespan due to less initial drag, and will have minimal interference from AIS signals which will be discussed in Sec. 4.4.

The daytime, night-time, and radio coverage of each orbit are to be assessed, in addition to coverage gaps between the constellations' successive revisits (DG). For the coverage analysis, all areas within the SA EEZ are regarded as equally important and prioritisation falls outside the thesis' scope. Furthermore, the nodal regression and argument of perigee for the orbits were chosen as 188° and 90°, respectively. This is because the orbit discussed in Sec. 4.3.3 repeats its ground track and these parameters places its track to move along the SA EEZ. Furthermore, for completeness' sake, all of the orbits are chosen to have the same epoch, nodal regression, and argument of perigee.

4.3.1 Orbit 1: ISS Inclined Orbit

This orbit is 100 km higher in altitude than the QB50 satellites, which were deployed from the ISS as it is a cheaper orbit-injection option. Therefore, it will have better global EC, a slightly worse GSD and a longer lifetime, as it has a higher orbiting

altitude. The Keplerian elements for the ISS orbit are listed in Table 4.3, where the eccentricity is based on the ISS's TLE. As this orbit has an inclination angle close to 50°, it should reflect good EC regarding the initial inspection.

Table 4.3: Keplerian orbital parameters for orbit 1.

Parameter	**Value**
Altitude	500 km
Inclination	51.64°
Eccentricity	0.000 850 8

However, it will be infeasible to transfer the satellite from the ISS's orbit into a 500 km orbit, as CubeSats do not possess the propulsion budget to accommodate a manoeuvre of approximately 52 $\mathrm{m\,s^{-1}}$ ΔV in addition to compensating for aerodynamic drag; this is discussed in appendix B.6.

4.3.2 Orbit 2: SSO

SSOs are usually chosen for EO as their ascending or descending SSP has consistent illumination from the Sun. Therefore, the orbit delivers constant lighting conditions for an optical payload throughout its lifetime. This will reduce that image-processing complexity as objects with their shadows will look similar in different images.

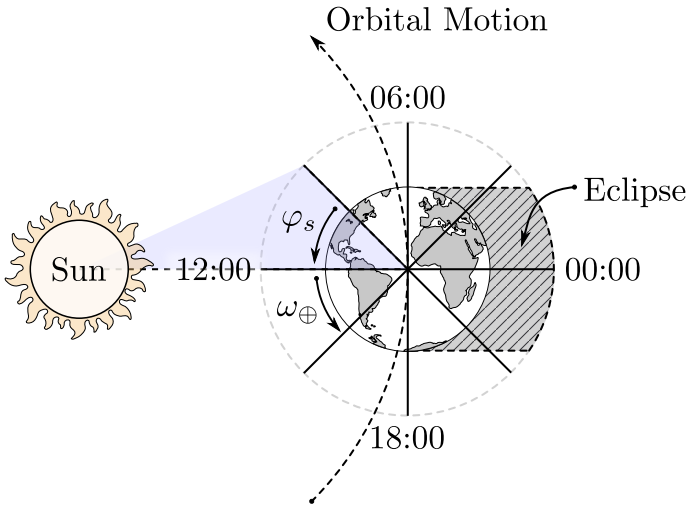

Figure 4.9: SSO orbital explanation.

These orbits make a constant angle to the centre of the Sun, depicted in Fig. 4.9 as the angle φ_s of the blue triangle. The orbital lines are viewed as top-down; therefore, they are straight lines. They are only ever in eclipse should the end of the line fall within the eclipse-region, depicted as a hatched grey area. The satellite's local revisit time can be chosen by adjusting φ_s. Consequently, each consecutive equatorial crossing has a half-day local time difference. Generally, a 02h00/14h00 or 10h00/22h00 orbit is chosen for ideal imaging conditions, as there will be no sun-glint present in images.

Table 4.4: Keplerian orbital parameters for orbit 2.

Parameter	Value
Altitude	500 km
Inclination	97.34°
Eccentricity	0.001

The angle φ_s remains constant by designing the orbit such the secular change in nodal regression is negative that of the angular velocity of the Earth about the Sun:

$$\dot{\Omega}_{\text{SSO}} = \frac{360^\circ}{365.2564} = 0.986^\circ \text{ per sidereal day}$$

As nodal regression is negative for retrograde orbits, this will only occur if the inclination angle is larger than 90°. Moreover, recalling Eq. (2.11) as a function of Eq. (2.9), the orbit will be sun-synchronous if P equals one, which will result in the orbital plane's change in nodal regression to be equal to 0.986° per sidereal day. This was iteratively solvedfor an orbiting altitude of 500 km as 97.34°. Finally, the SSO for this thesis is a 02h00/14h00 orbit.

4.3.3 Orbit 3: RGT

Satellite missions devoted to Earth and climate observation, such as to studying gravity, atmosphere, and altimetry, commonly use RGT orbits [45]. However, ground tracks gradually shift over time due to orbital-perturbation influences and correctional manoeuvres are required to maintain the repeatability of the ground track, which will be discussed in appendix B.6.

An RGT orbit retraces its ground track over a period within a repeat cycle to periodically revisit and observe the same locations on Earth [45]. These orbits require a set of fixed equator-crossing points with a constant inclination angle. Referring to Table 2.4, the orbital inclination has no secular effects and is assumed to remain constant for this thesis. A satellite's motion about the Earth should correspond with the Earth's rotation for an RGT orbit. Therefore, the repetition of its ground track is a function of both its orbit and the Earth's rotation period.

Recalling Eq. (2.12), the orbit is classified as an RGT if N is a rational number. The satellite's nodal frequency can furthermore be expressed as:

$$N = \nu_0 + \frac{d}{D}$$

Where ν_0 is the number of orbits completed in a sidereal day and D describes the number of repeat cycles required before the SSP is at the same location. Consequently, $N \cdot D$ is the number of orbits required for the satellite to revisit a coordinate on Earth. In the case where d is zero, the satellite performs an integer number of orbits with respect to a fixed coordinate, daily.

Table 4.5: List of successfully launched AIS satellites with their respective orbits.

Satellite	***H***	***i***
Triton	620 km	97.8°
Perseus-M	700 km	98°
Lemur-2 1 Joel	640 km	6°
Lemur-2 13 Beccadewey	500 km	51.6°
Lemur-2 101 Wanli	530 km	97.5°

Table 4.5 lists some S-AIS satellites launched to date, it should be noted that more than 100 AIS CubeSats have been launched, many of which were launched by Spire. These satellites generally have altitudes ranging from 400 km–640 km, therefore, an initial orbiting altitude of 600 km was chosen to iteratively find a RGT orbit. The nodal frequency, N, at this altitude is 14.6854. By increasing the altitude, N tends to 14.5 that will result in a non-realisable Electron Rocket launch and increased AIS-interference, as discussed in Sec. 4.4. Instead, it was decided to lower the altitude and using Eq. (2.12) in an iterative process to achieve a nodal frequency of 15 that resulted in an altitude of 493.2 km at the aforementioned orbital inclination of 48°. Finally, the RGT orbit's orbital parameters are listed in Table 4.6

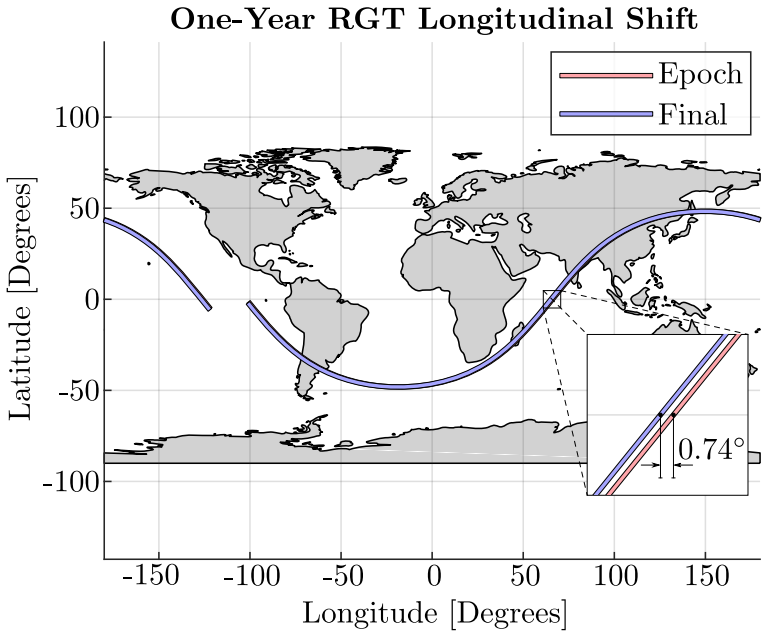

Figure 4.10: RGT orbit longitudinal drift after a solar year.

As approximations are used to calculate the RGT altitude, the repeatability is evaluated by measuring the satellite's longitudinal drift after a solar year, which results in 5475 orbits. The result is acquired by simulating the satellite for one orbit at epoch then for another orbit after one solar year, which is depicted in Fig. 4.10 as the red and blue ground tracks, respectively.

Table 4.6: Keplerian orbital parameters for orbit 3.

Parameter	**Value**
Altitude	493.2 km
Inclination	48°
Eccentricity	0.001

It is found that the longitudinal drift for a solar year is 0.74°, or 83 km, westwards that results in a change in nodal regression of 0.000 14° per orbit, which is deemed negligible. The resultant error is due to the nodal frequency not precisely being 15 accurate to more than 2 decimals, as it is decided under the author's discretion that an orbital altitude cannot be maintained to metre-accuracy.

Recall λ_S, the longitudinal difference of two successive passes, whereas the longitudinal difference of two adjacent passes through the equator for an RGT orbit is:

$$\delta_{\oplus} = \frac{360^\circ}{N \cdot D}$$

As the satellite crosses the equator $N \cdot D$ times in one repeat cycle. The grid interval, $\delta_{\oplus}$, for the RGT orbit at the equator is calculated as 24°, which is 1° larger than the SA EEZ. Therefore, the ascending and descending passes will roughly intersect either side of the EEZ with a 20° look angle. As the ground tracks repeat, certain areas of the EEZ will never be sensed and a constellation is required to sense the entire EEZ.

4.3.4 Comparison

For the remainder of the thesis, a specific orbit must be chosen in order to conduct further analysis. As such, the aforementioned three orbits, namely: ISS, SSO, and RGT will be compared by means of:

1. respective day coverage (DC) and night coverage (NC) area,
2. area of interest (AoI) revisit time,
3. dark gaps (DG), and
4. radio coverage (RC).

For the remainder of this thesis, a constellation of 10 satellites is chosen as their look-angles overlap and a subsequent pass can inspect the same area. Lastly, it should be noted that eclipse times will not be compared as the ISS and RGT orbital planes' angle changes with respect to the Sun. As such, their worst case eclipse times are to be used for further analysis.

4.3.4.1 Day and Night Coverage

The orbits' DC and NC is a function of each satellite in the constellation's AA. It was decided to inspect each satellite individually for unbiased results for a 120 day period. This period is double that of $T_{\overline{\circlearrowleft}}$ to minimise periodic effects.

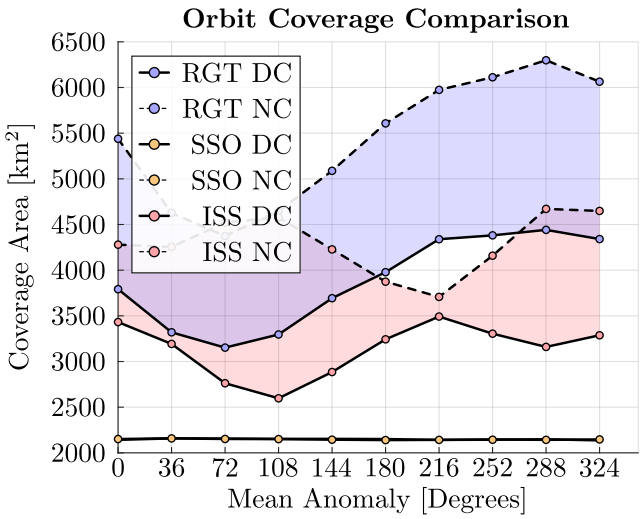

Figure 4.11: Constellation DC and NC Comparison.

The DC and NC comparison between the respective orbits is depicted in Fig. 4.11, where the blue, red and yellow plots indicate the RGT, SSO and ISS orbits, respectively, and the solid as dashed lines indicate DC and NC, respectively. The RGT and ISS orbits observe the most EEZ area, even though it oscillates. The mean anomaly, ν, of each satellite is incremented by $\frac{360^\circ}{N_{\text{sat}}}$, which is indicates the pearl-string configuration. In contrast, the SSO observes roughly half that of the aforementioned orbits but the coverage remains constant for each satellite in the orbit.

4.3.4.2 Dark Gaps

Next, each constellation's DGs are investigated. This is achieved by comparing the frequency at which the constellation senses the SA EEZ during daytime for a solar year. The results are presented in Fig. 4.12, where a pass is considered a sighting when the satellite passes between 07h00 and 17h00, where the blue, red and yellow curves indicate the RGT, SSO and ISS orbits, respectively.

It is clear that the RGT and ISS orbits are underperforming in comparison to the SSO. The SSO constellation senses the coast at least 12 times per day in contrast to the RGT and ISS orbits that have respective DGs of ten and nine days. However, both the RGT and ISS orbits observe the EEZ nearly double that of the SSO. Furthermore, it should be noted that imaging data is auxiliary to the AIS data, therefore, the RC, in addition to the AoI coverage, should be investigated before a final conclusion can be formulated.

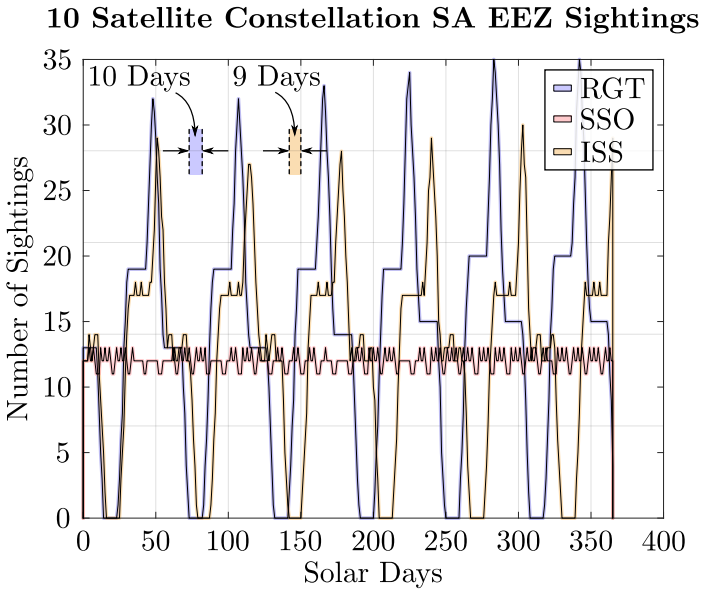

Figure 4.12: Daily SA EEZ sighting and DG comparison between the respective constellations.

4.3.4.3 Area of Interest

The AoI is chosen as a $0.1°\times0.1°$ square within the mainland EEZ at a latitude between -35 and -37, as its revisit-time is important for data-validation. The simulated results coincide with Fig. 4.12 and are presented in Fig. 4.13, where the blue, red and yellow plots indicate RGT, SSO and ISS orbits respectively. The maximum revisit times are indicated with a dashed line with the respective orbit-colour. Consequently, for 16 of the 60 days, an AoI will not be able to be inspected should data validation be required.

Notably, if misclassification of a vessel occurred, the constellation can focus on the AoI to reinspect said area. However, this will not be possible for the RGT and ISS orbits on the final day of DC before a DG; consequently, during night-time, only RC can be used for vessel detection.

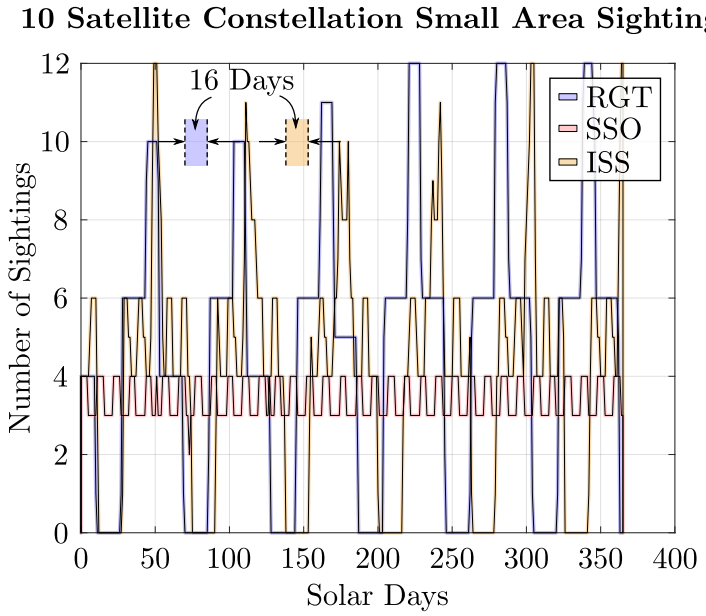

Figure 4.13: Constellation AoI daily revisits and DGs.

4.3.4.4 Radio Coverage

Finally, the RC for each constellation is evaluated to determine AIS and data downlink capabilities. The results were acquired using the orbital parameters listed in Tables 4.3 to 4.6 and is presented in Fig. 4.14 and Table 4.7. For radio communication, the daily revisits, revisit time and coverage time must be investigated to get a good idea of its performance. Furthermore, the look angle for the antennas are calculated using Eq. (2.1) as RC is assumed to be possible above an elevation of 0°.

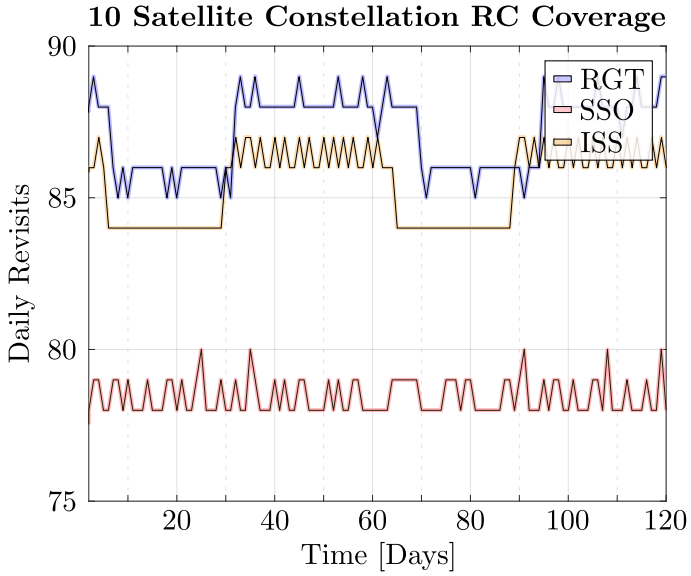

Figure 4.14: RC's revisit time for respective constellations.

The daily revisits, depicted in Fig. 4.14, show the RGT, SSO, and ISS results in blue, red, and yellow, respectively. The RGT and ISS marginally outperform the SSO and the difference is deemed negligible. However, when inspecting Table 4.7, the coverage times for the RGT and ISS orbits is 25% more than the SSO orbits due to its lower inclination angle. This implies that these orbits see larger areas of the coast, therefore, has a better chance at intercepting AIS-signals and can download more data to a ground station, as will be discussed in Sec. 4.4.2. Lastly, the SSO constellation has the lowest revisit time due to its large inclination angle. This implies that processed data can be relayed sooner.

Table 4.7: Respective constellations' revisit time (RT) and coverage time (CT).

Orbit	**RT [Hour]**	**CT [Days]**
RGT	9.97	111.98
ISS	9.64	113.96
SSO	7.24	86.69

4.3.4.5 Conclusion

Taking these four factors into consideration, it is clear that the SSO is superior regarding daily AoI imaging and with lower revisit times, whereas the RGT and ISS orbits cover far more area in a solar year that will result in higher data-integrity and more reliable AIS-data. Since frequent AIS message reception is required to track vessels and image-data is used to verify it, an RGT was chosen for this thesis. This would allow more AIS messages to be received, but impairing DGs as a result.

The RGT orbit can be improved by adding an additional orbital plane orthogonal to the suggested one. This is achieved by introducing a 180° nodal regression difference with the goal to reduce the DGs. This was generated using STK and is depicted in Fig. 4.15 using one satellite in each respective plane, more satellites will cause minor shifts in the ground track and only two is required to show the illumination difference. As one plane is good lighting conditions, the other is in a DG. This is deemed future work and will not be discussed in this thesis.

As the RGT constellation does not image in consistent lighting conditions, the time of day at which the constellation senses the EEZ should be investigated. The time difference between observations is inspected by means of simulation. Both STK and the MATLAB simulations are implemented and compared to identify a time-trend, where STK is set to use a J4Perturbation propagator that does not consider atmospheric drag, solar radiation pressure, or third body gravity. This propagator is used for modelling an orbit that is maintained by orbital manoeuvrers and is deemed as the ground truth with which to compare the MATLAB simulation. However, for the constellation to be RGT the orbit altitude had to be adjusted to 494.36 km.

(a) (b)

Figure 4.15: Orthogonal RGT orbit planes to reduce DG. **(a)** shows the satellites orbiting Earth and (b) is its projection onto a 2-D plane.

This is a small change and can be corrected with in-orbit manoeuvrers should the orbit not be RGT.

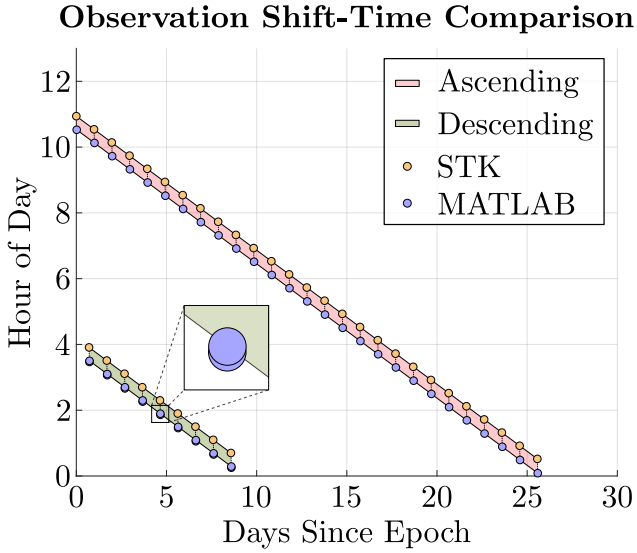

Figure 4.16: Comparison between STK and MATLAB SA EEZ observation times.

The elements listed in Table 4.6 were used to initialise the time-of-day simulations using one satellite with the results for 26 solar days are depicted in Fig. 4.16. One satellite is used for clarity and only 26 days were chosen as the results showed a linear relationship, where the red and green lines indicate the ascending and descending passes, respectively. The time difference between an ascending and descending pass for a 10 satellite constellation is listed in Table 4.7 as RT and cannot be calculated using Fig. 4.16 as it is the result of one satellite. Finally, the blue and yellow dots resemble MATLAB and STK results, respectively.

Both the MATLAB and STK simulations only sense the mainland EEZ to avoid confusion when inspecting the result. When the archipelago is added there are many more observations that do not make intuitive sense, unless when inspecting

the ground tracks. Consequently, there are fewer observations than in Figs. 4.11 to 4.13 and the MATLAB simulation has two visits on the descending pass as the mainland EEZ is intersected twice during a descending pass, as per Fig. 4.17. The black lines are the satellite's ground tracks, which is enlarged to show the RGT. The EEZ is indicated with a blue polygon and the coverage sweeps with a red polygon for 120 day period.

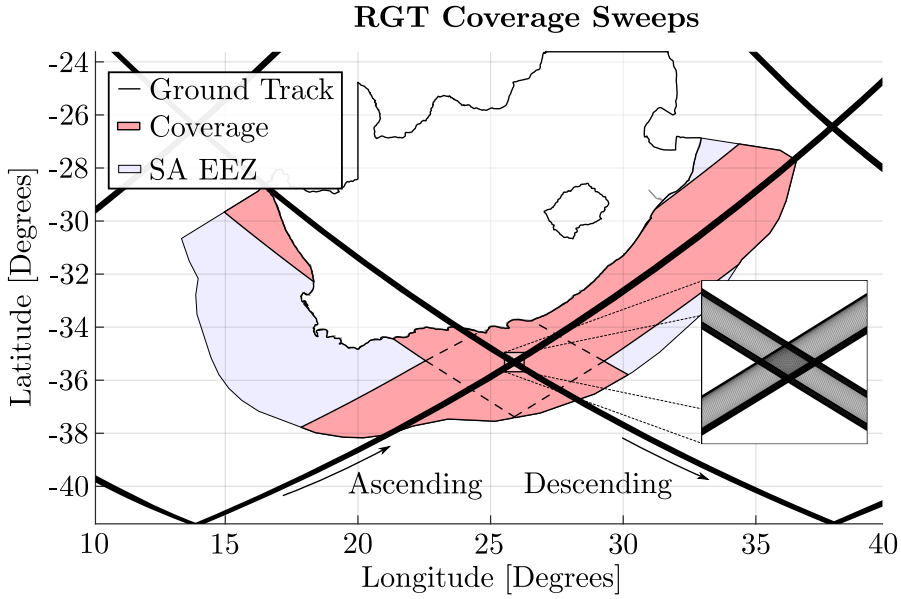

Figure 4.17: RGT cover sweeps of the mainland EEZ of a 120 day period.

Finally, the satellite constellation will sense the SA EEZ slightly earlier each day, as depicted in Fig. 4.16. The 25 min delay between the constellations in Fig. 4.16 is due to a 90 min epoch and 1.43 km orbital altitude difference. Nevertheless, the time-trends roughly coincide and indicate similar linear relationships of -1470.05 s and -1467.40 s for the MATLAB and STK results, respectively. As these values are similar, the general trend is calculated as the average being -1468.72 s. As such, each day the constellation will sense the SA EEZ 25.5 min earlier.

The general trend is an irrational number indicating that the satellite will not observe the EEZ with the exact same lighting conditions. However, similar lighting conditions are not required to identify vessels. Furthermore, the satellite has a $T_{\overline{\circlearrowleft}}$ of ≈ 60 days of which 14 days will be in low-light conditions, or form the DG. When introducing 10 satellites into the orbit the gap between successive passes becomes smaller and the DG is reduced to 10 days.

4.4 AIS Feasibility

CubeSats with onboard S-AIS receivers are susceptible to missing AIS packets as a consequence of the SOTDMA protocol, interference, and long-distance communication. This introduces a probability of overlooking vessels in the CubeSats' FoV

radio-horizon. Theoretically, this could impede the detection of radio-silent vessels in the EEZ because non-radio-silent vessels will be misclassified.

This section will elaborate on the methodology used to evaluate the feasibility of S-AIS packet reception in the SA EEZ and elaborate on the difficulties such as:

1. Greater communication distances at low elevation angles,
2. Atmospheric losses and system noise, and
3. Small satellites having wide antenna beam-widths.

4.4.1 Statistical Approach

Firstly, a statistical approach will determine the maximum number of vessels in the CubeSat's FoV based on a message collision approach. Initially, the satellite's antenna is assumed to have isotropic radiation, therefore, all the vessels within the FoV are considered. Thereafter, a simulation will evaluate the effectiveness of the RGT orbit to determine the likelihood of vessel detection based on link-budget analysis.

The likelihood of detecting an AIS packet is based on a statistical model introduced by Cervera et al.[16]. For this model, a message is successfully received when it does not collide with another message, as depicted in Fig. 2.3. Consequently, the number of message-collisions per AIS-frame depends on the number of vessels in the CubeSat's FoV, in addition to the vessels' reporting interval. This method makes the following assumptions:

1. Only cargo and fishing (Class A) vessels exist (database constraint),
2. Vessel locations are sampled from a probability distribution,
3. All vessels broadcast using the same reporting interval; vessels navigate at the same velocity,
4. A packet is successfully detected if it is broadcasted whilst no other vessel is transmitting,
5. Message delays, path loss, and interference do not exist, and
6. The vessels broadcast on both channels AIS independently.

The assumption that all the vessels broadcast at the same interval is based on Fig. 3.2 and to simplify the proposed analytical solution, as the majority of the messages have a short reporting interval. Sec. 4.4.2 elaborates with a more realistic reporting interval approach. Consequently, Eq. (4.4) evaluates the probability, P_d, that a packet-conflict occurs among N vessels in $M(N)$ SOTDMA regions, broadcasting for τ (26.6 ms) seconds in a Δt reporting interval for the duration of T_v. For this subsection, the reporting interval is chosen as 6 s, as most deep-sea vessels broadcast

in this interval when inspecting Table 2.1. The CubeSat's visibility, T_v, is determined by its orbital parameters and vessel location [16].

$$P_d = 1 - \left[1 - \left(1 - \frac{N}{M(N)}\frac{\tau}{\Delta t}\right)^{M(N)-1}\right]^{\frac{T_v}{\Delta t}} \tag{4.4}$$

Consequently, $\left(1 - \frac{N}{M(N)}\frac{\tau}{\Delta t}\right)^{M(N)-1}$ is the probability that no packet conflicts occur, considering all the SOTDMA-cells with their respective vessels. Furthermore, the time when a vessel can be sensed depends on its distance from the satellite's ground track. As such, the vessel under analysis transmits $T_v/\Delta t$ packets during the CubeSat's overpass and the probability of detecting a vessel is calculated given its location within the CubeSat's FoV and the number of vessels.

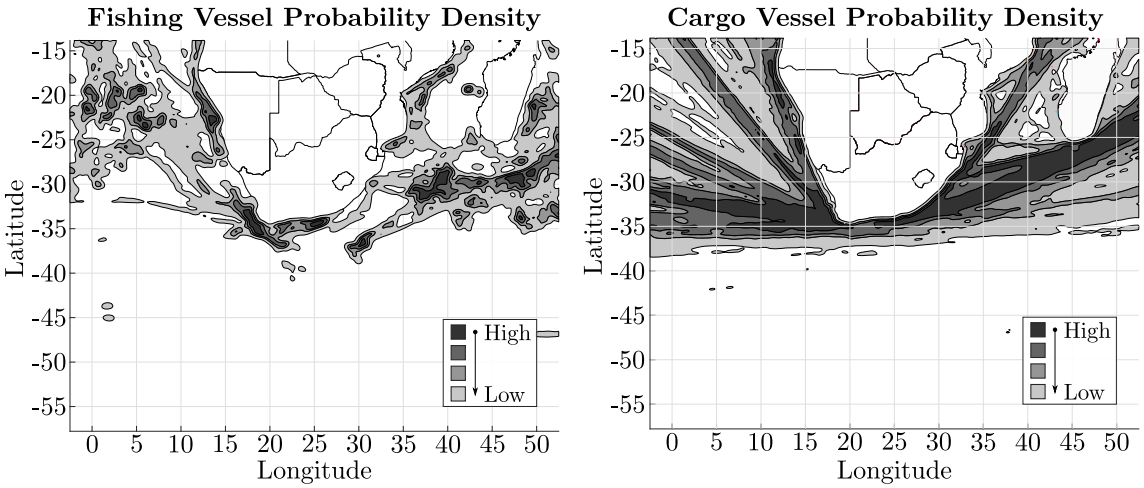

Figure 4.18: Generated vessel contour plots in the typical footprint of a 500 km altitude satellite for the duration of one month.

For the statistical analysis, the vessels were sampled from a realistic fishing and cargo vessel density map depicted in Fig. 4.18. These maps are courtesy of the *CSIR* team that works on the *OCIMS*-project. A probability density function (PDF) was generated using the vessel-map, where vessel positions are binned each month in a $0.1^\circ \times 0.1^\circ$ area. For display purposes, the densities in Fig. 4.18 are convoluted with a Gaussian distribution of a 10-bins variance. Consequently, the contour plot intersects the SA border.

Sampling vessel locations from the PDF was achieved by uniformly sampling points in a 3-D space with the same bounds as the PDF. Thereafter, all the points that lie below the PDF are valid vessel locations and used as samples. From this the number of SOTDMA-cells, $M(N)$, was determined by generating N vessels from the PDF in the satellite's FoV using algorithm 4.2, where the FoV-radius is roughly 2500 km and the typical vessel VHF communication distance is 72 km [16].

Algorithm 4.2: Number of SOTDMA-regions in the FoV of the CubeSat.

Input: $N_{\text{ships}}, FoV_{\text{radius}}$
Output: N_{regions}

```
for n ← 1 to N_ships step 1 do
    i ← 1;
    while i ≤ n do
        vessels_i ← sample_distribution;
        if vessels_i in FoV and not vessels_i on land then
            i ← i + 1;
    N_regions ← 0;
    while vessels is not null do
        i ← 1;
        // All the points are random, choose the first one.
        while i ≤ length(vessels) do
            if arclength(vessel_1, vessel_i) ≤ 72 then
                remove(vessel_i);
            else
                remove(vessel_1);
                i ← i + 1;
        N_regions ← N_regions + 1;
```

To elaborate on the aforementioned algorithm: array-indexing start at one; the last element is the array's length. Furthermore, it is assumed that the order in which the vessels are removed has a negligible effect due to the 5000 samples. This number was empirically chosen such that the vessels bound by the EEZ exceeds the usual amount of roughly 800. It corresponds with the vessels in the SA EEZ as seen in Fig. 3.2 and in the case of 5000 vessels in the FoV, the number of vessels bound by the EEZ has a mean of 900.

The time-step that was used to determine the number of SOTDMA-cells is depicted in Fig. 4.19. The CubeSat's FoV is highlighted in orange and is distorted due to spherical-to-Cartesian projection. For clarity's sake, only 2000 samples are displayed in this figure with a cargo-to-fishing vessel ratio of 5:1. This ratio is an informed estimation by means of visual assessment of the website `www.marinetraffic.com`. Lastly, there are a negligible number of vessels in the Islands' EEZ, although this should be monitored.

Four regions within the CubeSat's FoV were chosen to determine T_v. These regions are logarithmically spaced with the smaller intervals towards the edge of the FoV, as this is where the largest change in distance occurs. This is expressed in Fig. 4.20a,

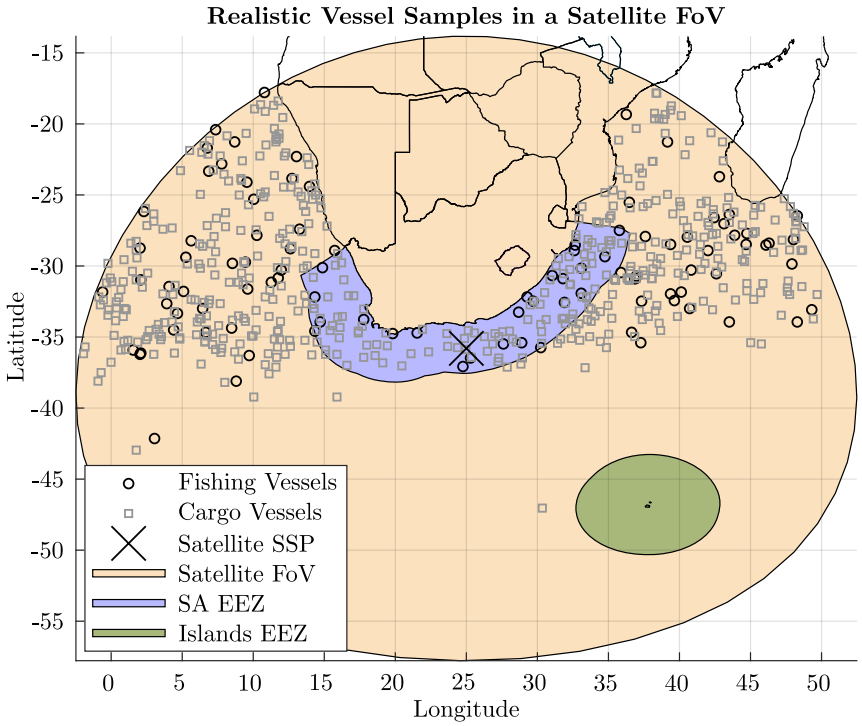

Figure 4.19: 493.2 km altitude satellite's FoV with a realistic vessel-distribution.

where a vessel closest to the satellite's ground track can be sensed for the longest duration and is depicted in green, whereas the region that is sensed the smallest amount of time is indicated with red.

Consequently, T_v is calculated by assuming that the CubeSat's velocity, v_s, remains constant in its circular orbit and is calculated by using the vis-viva equation, expressed in Eq. (4.5), as $7.62\,\mathrm{km\,s^{-1}}$. $\mu_\oplus = 3.986 \times 10^{14}\,\mathrm{m^3\,s^{-2}}$ is Earth's standard gravitational parameter, and H is the orbital altitude, 493.2 km.

$$v_s = \sqrt{\frac{\mu_\oplus}{R_\oplus + H}} \tag{4.5}$$

The distance that the satellite can travel with which to intercept an AIS-broadcast, assuming a communication elevation angle of 0°, is calculated using Eq. (2.6) as 4862.53 km. Therefore, the longest duration a vessel can be sensed is $\frac{4862.5}{7.62} = 638.4\,\mathrm{s}$. Referring to Fig. 4.20a, the satellite's FoV is logarithmically divided into n sections, where each section is seen for T_v seconds as indicated in the figure and depends on the orthogonal distance ℓ. Finally, P_D is calculated for the different sections of the FoV and is shown in Fig. 4.20b. A vessel far away from the ground track has a much smaller chance of being detected.

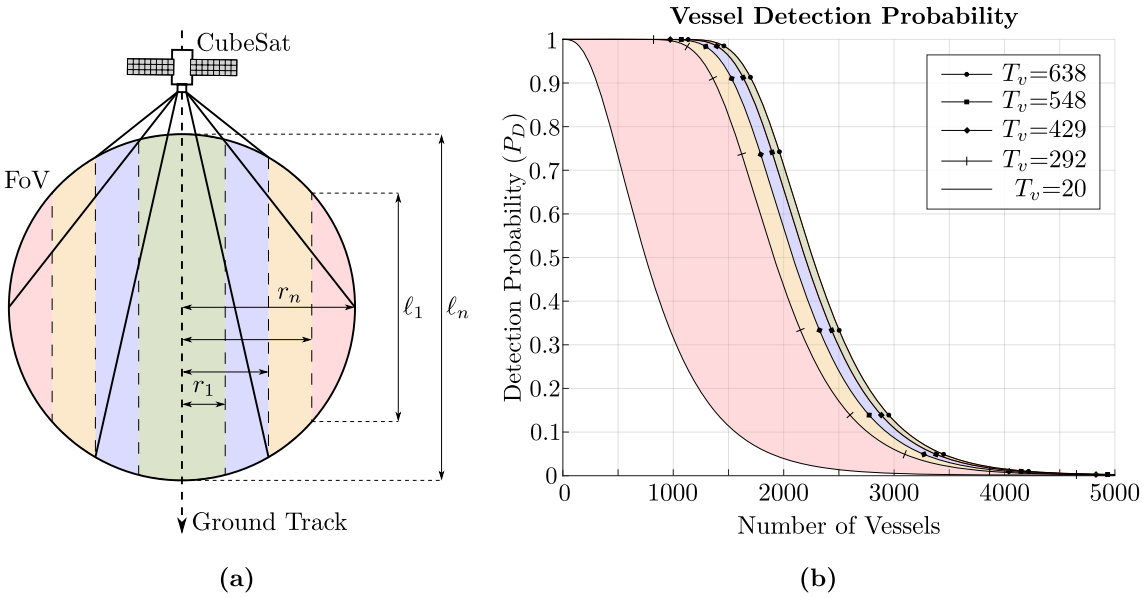

Figure 4.20: Statistical approach to AIS reception capabilities.

4.4.1.1 Conclusion

The further away a vessel is from a satellite's ground track, the less probable it is to detect it. Additionally, if there are more than 5000 vessels in the FoV broadcasting every 6 s there is a near-zero per cent chance of detecting a vessel due to packet clashes. However, due to signal loss, obstacles and non-isotropic antennas, the satellite's FoV is effectively reduced as there will be fewer vessels detected. Furthermore, all the vessels broadcasting every 6 s is a pessimistic assumption and the ideal case would be for vessels in the *red-region* to broadcast every 6 s and vessels in the *green-region* to broadcast every 180 s, referring to Fig. 4.20. This will ensure a near 100% detection rate.

It should be noted that the assumptions used in deriving Eq. (4.4) are pessimistic, for example, that packet collisions result in loss of data and that all the vessels transmit in the same interval. In a realistic environment, signal strength plays an important role in the detection of vessels. This section did not consider signal strength and the subsequent subsection will further discuss these impacts.

Finally, it is noted that there are few vessels in the archipelago EEZ and it is recommended to launch the satellite constellation into a 39° orbit with one satellite in a 51.3° ISS orbit to survey the aforementioned area. This will result in much more image and radio coverage of the mainland EEZ.

4.4.2 Simulation Approach

The previous subsection verified that the orbit altitude influences the number of vessels in the FoV. This subsection will elaborate on the previous statistical analysis and on the made assumptions. A packet is now classified to be successfully received by a satellite if its signal-to-noise ratio is deemed satisfactory. Furthermore, an actual AIS dataset will be used as ground truth for messages transmitted by vessels, as generating realistic AIS data lies outside the scope of this thesis.

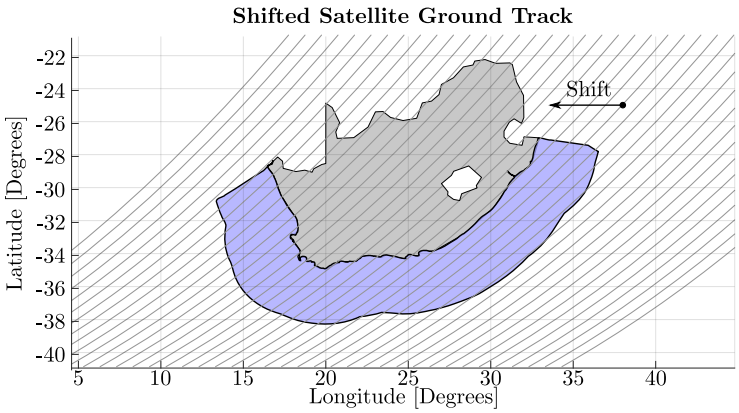

Figure 4.21: AIS simulation's ground track repeated 41 times with each ground track shifted 1° for every iteration.

This is achieved by link-budget analysis on the communication link between the vessels and satellites. A link-budget is an audit of all the transmission power gains and losses in a telecommunication system, which will be elaborated upon in Sec. 4.4.2.1. Furthermore, decoded AIS data is used to test the link budget, in addition to generated ground tracks of the RGT orbit using the SGP4 model. The elements described in Table 4.6 is used for this analysis as the satellite passes along the east coast of SA on its ascending pass.

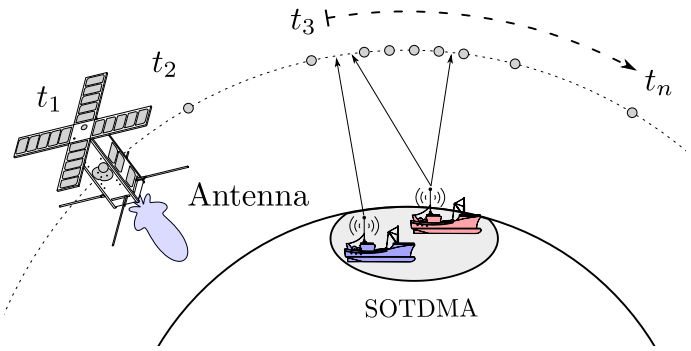

Figure 4.22: AIS feasibility simulation environment description.

This methodology is described as per Fig. 4.22, where the satellite ground track is represented by varying time-steps t_1 to t_n, as described in Sec. 4.1, and the blue and red vessels are within the SA EEZ, depicted by the grey bound. The vessels transmit

between discrete time-steps, therefore these messages are binned accordingly if the transmitting vessel lies within the coverage of the satellite. Lastly, the ground track is shifted eastward 40 times and the time of pass is distributed throughout the day with 10 equally spaced steps, as depicted in Fig. 4.21. Therefore, a dataset is processed 410 times to utilise all the transmissions broadcasted throughout the day.

4.4.2.1 Communication Links

The link budget is one of the important components in determining the performance of the antenna [31]. The only antenna characteristics considered for this thesis is the gain, dimensions, and half-power beamwidth (HPBW), as the antennas are assumed to be commercially available and will require no matching and current balancing networks. Furthermore, it is assumed that the antennas are not affected by other components. The HPBW is the angular separation between two identical points of its radiation-pattern where the amplitude is 3 dB below the boresight gain; the boresight gain is the maximum gain.

Because AIS operates in VHF, the atmospheric and precipitation losses are small. The largest atmospheric loss is the Faraday Rotation that causes linearly polarised radio waves to rotate as a function of its wavelength when passing through the ionosphere. This is caused by the inhomogeneities of electron density and results in amplitude and phase fluctuations termed scintillations [46] . Therefore, the satellite will require a circularly polarised antenna. After each vessel has been parsed into the model, the distance and the elevation to the satellite is calculated. This is calculated based on the satellite's position at the respective time the AIS message was sent. The distance and the elevation is used to calculate the free-space losses and antenna gains, respectively.

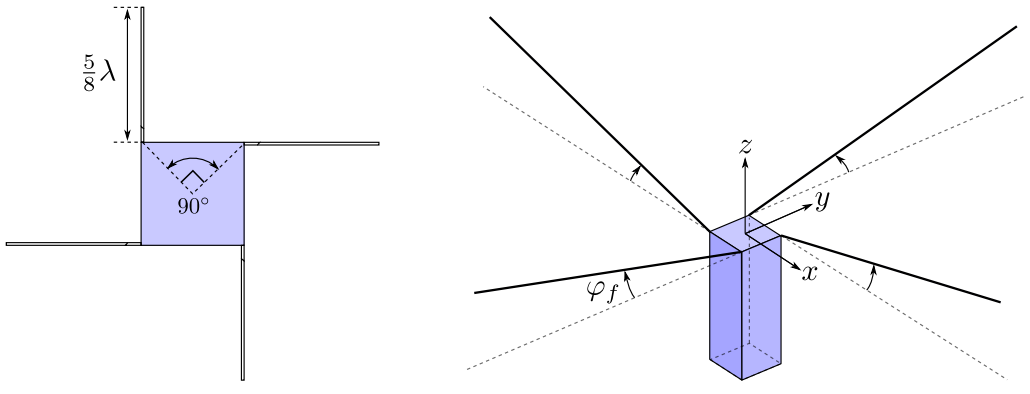

Figure 4.23: Simple VHF Crossed Monopole Antenna on a 3U CubeSat.

A helical antenna is described by its length, diameter, number of turns, and its

ground plane. The only bound for a helical antenna is:

$$0.8 \leq \frac{C}{\lambda} \leq 1.2$$

Where $C = \pi D$ that results in the smallest possible diameter at 161.976 MHz to be 0.471 m. Furthermore, a rule of thumb for the antenna's ground-plane is to be 0.8λ, which results in 1.5 m at the aforementioned centre frequency. Consequently, these dimensions are deemed too large to feasibly deploy on a 6U CubeSat and will not be discussed in this thesis.

A good alternative to a helical antenna is a crossed-monopole antenna, which can more easily be deployed from a 6U CubeSat. Each $5\lambda/8$ monopole is deployed 90° from each other from the CubeSat with the signal received delayed by a 90° phase delay. As such, the phased monopoles are circularly polarised. This results in a 3 dB loss in signal and with a resulting antenna gain of 5 dB. This is a sophisticated circularly polarised antenna design that uses a sequential phase feeding technique. The design consists of two pairs of complementary dipole antennas located parallel to each other on a square-shaped substrate [31]. Each arm is designed with a 90° phase difference to feed the circularly polarised antenna.

Thin and flexible tape-spring deployable monopole antennas are often used on CubeSats, therefore, the option is limited to a deployable crossed-monopole antenna depicted in Fig. 4.23 [31]. The model that will be used for this thesis is simplified and based on perfect electrical conductors. Furthermore, all the antenna models are simulated using FEKO. Therefore, when doing link-budget analysis, antenna losses will be exaggerated.

Links are described in decibels (dB), which is a logarithmic scale; a 3 dB increase results in doubling the power. Furthermore, the transmission power is proportional to the data-rate and is inversely proportional to the square of the distance, as expressed in Eq. (4.7). Consequently, high-gain antennas will reduce the required transmission power by orders of magnitude.

The gain of an antenna is inversely proportional to its HPBW: if an antenna focuses all of its power in a narrow beam, the link is more efficient, however, the satellite must point the beam accurately. Moreover, the gain of an antenna is proportional to its area and its gain can be increased by roughly 6 dB by doubling its diameter [31]. Lastly, the antenna size is proportional to the frequency.

Defining the Link-Budget: As previously mentioned, the link-budget is a accounting of transmission gains and losses that will now be elaborated upon: firstly, the energy per received bit in a transmission is expressed as:

$$E_b = \frac{C}{R}$$

Where C, or P_r, is the received signal strength and R is the data-rate. Furthermore, the noise power is denoted:

$$N = kTB$$

Where $k = 1.3806 \times 10^{-23}\ \mathrm{m^2\,kg\,s^{-2}\,K^{-1}}$ is Boltzmann's constant, T is the receiver's noise temperature, and B is the channel's bandwidth. As such, the link budget can be written as:

$$\frac{C}{N} = \frac{E_b}{N_0} \times \frac{R}{B} \tag{4.6}$$

Where N_0 is the noise power spectral density. Finally, the communication link budget can be described as:

$$\frac{E_b}{N_0} = \frac{P_t G_t G_r L_{\text{tot}} L_\ell}{kTR} \tag{4.7}$$

Where P_t is the transmitted power, G_t and G_r are the respective gains for the transmitting and receiving antennas, L_{tot} includes all the losses from: connectors, atmospheric propagation, ionosphere, and rain, and L_ℓ is the propagation losses in free space which is calculated as:

$$L_\ell = \left(\frac{4\pi r}{\lambda}\right)^2$$

Where r is the distance from the transmitter to the receiver and λ is the carrier frequency's wavelength. Consequently, lower frequencies have smaller propagation-losses due to their longer wavelengths, and, therefore, require lower gains, whereas higher frequency antennas are smaller and more compliant with CubeSats to down-link data. Lastly, the losses expressed in Eq. (4.7), L_{tot}, are is elaborated upon in Eq. (4.8).

$$L_{\text{tot}} = L_{\text{TX}} \times A_{\text{AG}} \times A_{\text{RAIN}} \times L_{\text{POL}} \times L_{\text{POINT}} \times L_{\text{RX}} \tag{4.8}$$

Where:

- L_{TX} is the transmitter feeder losses caused by wiring, duplexers, and filters,
- A_{AG} is the clear-sky atmosphere and ionosphere attenuation that excludes Faraday Rotation,
- A_{RAIN} is the attenuation caused to clouds and precipitations,
- L_{POL} is the antenna polarisation mismatch losses, albeit linear, circular left and right hand,
- L_{POINT} is the antenna pointing losses, and
- L_{RX} is the receiver feeder losses.

Rain-attenuation is calculated using the specific attenuation and the effective rain path length. The attenuation is computed using the yearly rainfall-rate, R_P in $\mathrm{mm\,h^{-1}}$, that is assumed to be $P = 0.01$ for SA. The effective path length, L_E,

is computed combining the effect of the terrain height, elevation angle, and the longitude and latitude coordinates. However, rain-attenuation becomes negligible below frequencies of 1 GHz and will not be used for link-budget analysis in the VHF spectrum.

4.4.2.2 Satellite Reception Link

The end-fed crossed monopole antennas to be used for the satellites are assumed to be of length $5/8\lambda$. Monopoles of these lengths radiate the most energy in the horizontal direction; orthogonal to the antenna. However, AIS-message collisions are more probable if the radio-horizon is included, as determined in Sec. 4.4.1. Therefore, it was decided to tilt the VHF monopoles forward as an attempt to narrow the HPBW. Furthermore, each monopole is quadrature-fed resulting in each beam transmitting 90° out-of-phase to make the antenna circularly polarised to compensate for Faraday Rotation. This is because the vessels transmit linearly polarised signals.

The forward-tilting of the crossed monopole antenna is illustrated in Fig. 4.24a, where φ_f is described in Fig. 4.23 and is the angle by which the monopoles are tilted forward. This was achieved using FEKO's parameter sweep function to iteratively change the angles by which the monopoles are tilted and storing the boresight gain. From this figure it can be seen that an angle of 15° results in a satisfactory 5.6 dBi antenna gain; effectively reducing the HPBW. Although, the HPBW is 60° and is deemed relatively large, as the Earth angle, $\lambda_\oplus$, for a 493.2 km altitude orbit is 68°. This implies that vessels on the radio-horizon should be suppressed.

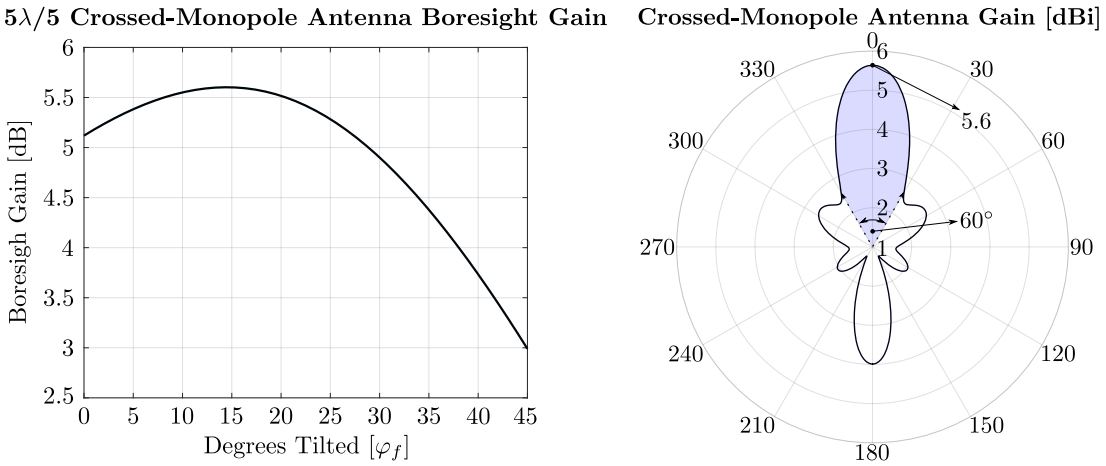

Figure 4.24: Crossed monopole antenna resultant parameter sweep and resultant radiation pattern.

4.4.2.3 Vessel Transmission Link

Typically, a vessel's AIS antennas and its corresponding equipment are not defined in the ITU standard. Generally, there are two types of AIS antennas in common use: a $\lambda/2$ and a $5\lambda/8$ end-fed monopole with gains ranging from 2 dBi–4.5 dBi [16]. Therefore, this thesis assumes that vessels use a $5\lambda/8$ monopole antenna that will be used for analysing the communication link, as it is the most common antenna installed on current AIS-equipped vessels. Furthermore, the antenna line-losses are estimated to be 3 dB with the antennas usually placed 10 m high [20], [21].

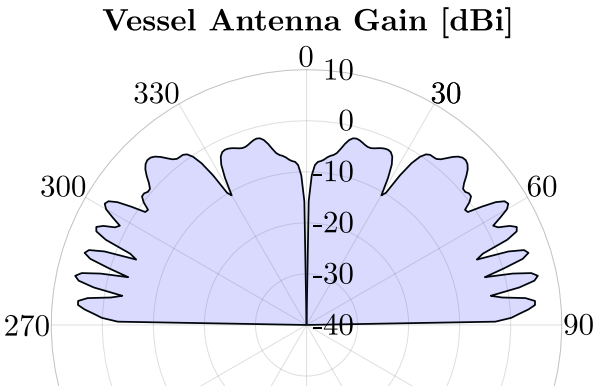

Figure 4.25: Simulated vessel $5/8\lambda$ monopole-antenna gain with backscatter from the ocean.

This antenna was simulated using FEKO with an infinite ground plane placed 10 m below the antenna with salt-water electrical properties. It is assumed that the dielectric properties for the ocean at 161.975 MHz is as follows: a relative permittivity, ϵ_r, of $80\,\mathrm{F\,m^{-1}}$, a dielectric loss tangent, $\tan\delta$, of 5.625, and a mass density, ρ, of $1029\,\mathrm{kg\,m^{-3}}$ [47]. These properties were only used to more accurately represent the radiation pattern of a vessel at sea and will not be further discussed in this thesis. The resultant radiation pattern for a vessel is depicted in Fig. 4.25, where it is evident that the ocean disrupts transmissions. Furthermore, between elevation angles of 60° to 90°, the antenna gain is below 0 dBi.

Lastly, a vessel in the deep sea is subject to large ocean waves that will roll and pitch the vessel's antenna, as seen in Fig. 4.26. Furthermore, the communication line-of-sight might be obscured by the waves resulting in a communication elevation angle of larger than 5°. However, for this thesis it is assumed that the angle θ_s, referring to Fig. 4.26, remains 0° that will result in a calm ocean.

4.4.2.4 Simulation Results

As the antenna gains are known, the system losses will now be investigated. This will include the AIS receiver to be used on the satellite, the assumed atmospheric losses and system noise.

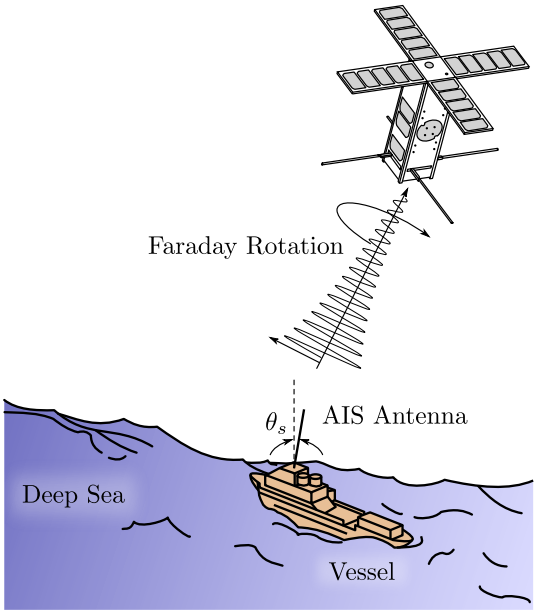

Figure 4.26: Deep sea vessel scenario with satellite flying overheard. The communication EM waves are depicted to lose amplitude and rotate as it passes through the atmosphere.

As both the receiving and transmitting stations were discussed, the total system losses, expressed in Eq. (4.8), can be calculated. This is done as follows on a logarithmic scale:

$$\begin{aligned} L_{\text{tot}} &= 20\log\left(L_{\text{TX}} \times A_{\text{AG}} \times A_{\text{RAIN}} \times L_{\text{POL}} \times L_{\text{POINT}} \times L_{\text{RX}}\right) \\ &= 3 + (1 + 0.4 + 0.2) + 0 + 3 + 0 + 2.5 \end{aligned}$$

Where the atmospheric losses include Tropospheric attention for a 5° communication elevation and also gain uncertainty. The total system losses is 10.1 dB

The chosen AIS receiver for the preliminary mission design is specified in Table 4.8. The receiver fits inside 1U and is capable of decoding weak messages when large Doppler frequency offsets are present [48]. Therefore, two vessels that broadcast at the same time can be differentiated from one another should they lie far enough from enough other. This technique will not be discussed in this thesis. Furthermore, the receiver is capable of receiving messages at −118 dBm and uses a standard CubeSat bus-voltage of 4.5 V–40 V.

Assuming that an AIS-receiver is optimally designed with a noise figure of 2 dB, a sensitivity of −118 dBm with a 1% PER is feasible [20]. The antenna noise temperature is dependent on precipitation, noise from the ionosphere and Earth. For this configuration the Sun- and Moon-bodies will not be considered:

$$T_A = T_{RAIN} + T_{SKY} + T_{EARTH} \approxeq 350\,\text{K}$$

Table 4.8: Satlab Polaris AIS receiver adapted from [48]

Parameter	**Specification**
Storage	1.13 GB
Power Usage	1.35 W
Sensitivity	−118 dBm
Operating Temperature	−40 °C–85 °C
Mass	0.185 kg
Noise Figure	2 dB

Finally, the total noise at the receiver's output is expressed as:

$$T_{RX} = \frac{T_A}{L_{\mathrm{RX}}} + 290\left(1 - \frac{1}{L_{\mathrm{RX}}}\right) T_R$$

Where T_R is the receiver's noise temperature expressed as:

$$T_R = 290\left(10^{F/10} - 1\right)$$

Finally, the total system noise is calculated as 493.4 K.

Lastly, the required signal strength is calculated using the receiver's sensitivity. This is usually the minimum input signal, S_i, required to produce a valid output signal. It has a specific SNR-ratio and is defined as the product of the minimum SNR-ratio and the mean noise power, as expressed in [49]:

$$S_i = kBF\frac{C}{N}\left(T_{\mathrm{A}} + T_{\mathrm{rx}}\right)$$

Where T_A and T_{RX} are the equivalent noise temperatures of the source and the input of the receiver in Kelvin, B is the bandwidth in Hertz, F is the receiver's noise figure, and $\frac{C}{N}$ is the required SNR at the output, which is calculated as 16.8 dB. Lastly, the free-space loss, L_ℓ, is calculated as a function of the vessel's position relative to the satellite with the maximum distance being 2556.3 km.

The methodology to used calculate the vessel-detection probability from Cervera et al. [16] is used. The probability of the onboard detector making an incorrect decoding is the probability of a bit error, denoted P_e and called the bit-error-rate (BER), which for one GMSK bit is the same as that of one MSK bit that is expressed as [50]:

$$P_e\left(\mathrm{GMSK}\right) = \frac{1}{2}\mathrm{erfc}\left(\sqrt{\frac{E_b}{2N_0}}\right)$$

Where *erfc* is the error function, which will not be discussed in this thesis, and is used to determine the packet-error-rate (PER) for each vessel, and $\frac{E_b}{N_0}$ is calculated using Eq. (4.6) and Eq. (4.7). Furthermore, this is used to calculate the PER of a vessel's AIS-message as:

$$\mathrm{PER}\left(n, i\right) = 1 - \left[1 - \mathrm{BER}\left(n, i\right)\right]^L$$

For n vessels transmitting N messages, of index i, that is L bits long. Finally, this is used to determine the probability, $P_d(n)$, that vessel n is detected as follows:

$$P_d = 1 - \prod_{i=1}^{N} \text{PER}\,(n, i)$$

Finally, the vessel-detection probability for each vessel is computed as expressed in Eq. (4.9). It should be noted that vessels broadcasting from different SOTDMA-cells are deemed independent events.

$$P_d = \frac{1}{N_{\text{ships}}} \sum_{n=1}^{N_{\text{ships}}} P_d\,(n) \tag{4.9}$$

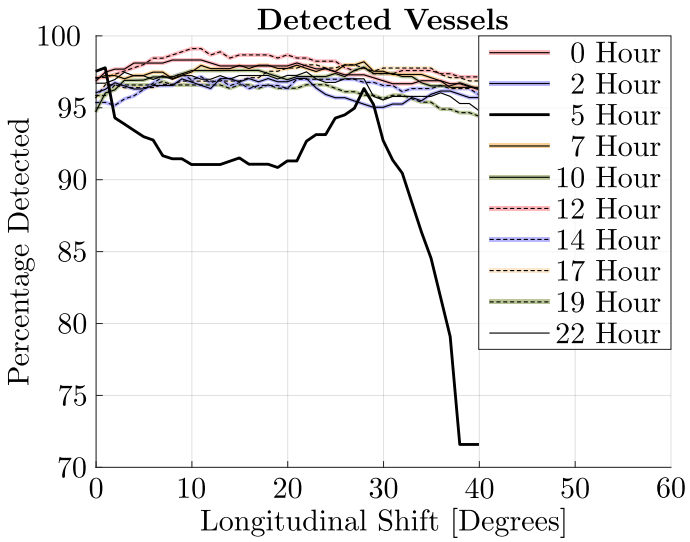

Figure 4.27: AIS message-detection probability given the communication link.

The results are depicted in Fig. 4.27 and 95% of the messages are received for the augmented simulation with the shifted ground tracks. However, during 05h00 there is a significant reduction in the received messages. Upon further inspection of the database, it was noted that very few messages were sent out at this time, with the majority of the vessels anchored port. This resulted in the 05h00 plot being biased, however, still has a detection rate of above 70% and is deemed as an outlier case. Finally, to conclude on this result, during the 410 simulations a total of 4 605 670 messages of the 4 776 759 total messages were successfully received, which results in a 96.4% reception rate.

Finally, the vessel-detection PDF is shown in Fig. 4.28. It indicates that there is a 0% probability of detecting vessels on the radio horizon. This is due to increase communication distance, the chosen satellite antenna configuration, vessel-antenna ocean backscatter, and the small period in which these vessels are observed. Furthermore, as the vessels are closer to the satellite's ground track, the probability

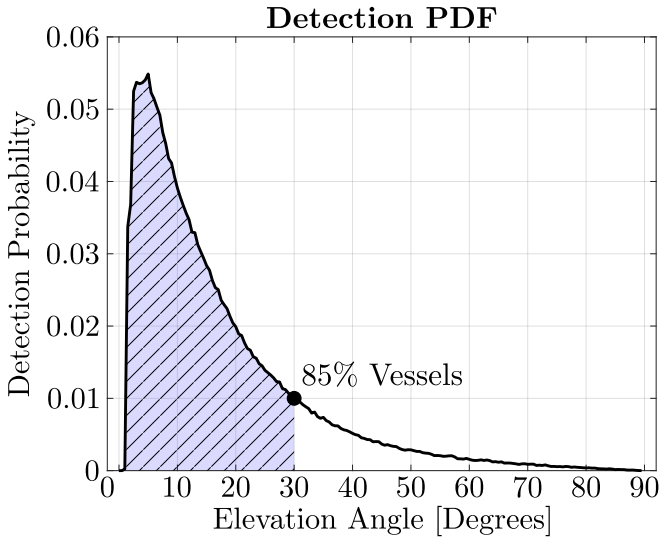

Figure 4.28: AIS message distribution given the number of messages sent per elevation angle and the link margin between the vessel-to-satellite.

of vessel-detection tends to 0% because the area near the ground track is much smaller when compared to the entirety of its AA. Consequently, there is a much smaller chance for a vessel to be located there. Penultimately, the blue hatched region shows that 85% of the vessels are detected below a 30° elevation and that no vessels are detected below a 2.5° elevation. Finally, it is assumed that a vessel's antenna does not have zero gain at a 90° elevation, as in a realistic environment the angle θ_s will vary and the back-scatter from the ocean will be detectable from the satellite.

4.4.2.5 Conclusion

The simulation approach used link-budget analysis that proved promising results with real data. Additionally, realistic assumptions were made regarding the transmission losses and BER. It is shown that at least 95% of the messages could be detected successfully. However, this simulation can be improved by allowing vessels to tilt or lean in the ocean. It was shown that large ocean waves could restrict elevation at which communication is possible. Additionally, it could serve beneficial should the vessel broadcast whilst being tilted as the satellite is directly above it; the link would be stronger was the vessel not tilted.

Furthermore, it is shown that it is more probable to detect vessels on the satellite's radio horizon. Therefore, a different antenna configuration should be investigated with a lower boresight gain and higher gain on the radio-horizon. The ideal case for AIS reception would be for vessels along the ground track to broadcast once every 3 min and vessels on the radio-horizon to broadcast every 6 s, as interference will be minimised. However, very little vessels broadcast the long-range protocol AIS-message 27, referring to Fig. 3.2a, that will only aid message reception should

the vessel lie near the satellite's ground track. Consequently, this message has a near-0% reception rate, should a vessel broadcast this message on the satellite's radio-horizon.

4.5 Conclusion

The first part of the chapter discussed the simulation environment successfully developed for this thesis. It is capable of simulating a constellation of satellites with specified orbital parameters and a payload look-angle. The numerical considerations are discussed to reduce execution time, allowing for larger simulations. However, the simulation excluded AIS-data that can be used to generate the best orbit using a cost-function. Furthermore, was this included, the vessel's future positions could be estimated when an image of their supposed location is sensed.

Furthermore, the time of passes was added using an intuitive plot to inspect the times at which the satellites sense the EEZ. Lastly, the satellite pointing introduced in appendix A can be used to expand the simulation environment to point to areas of interest during a satellite-pass for EC results rather than AA results. This will allow the satellite to point sense areas not yet inspected.

Three different orbits were compared, of which the RGT-constellation proved the most promising. This constellation has the longest revisit time that can be improved upon by introducing two orthogonal orbiting planes. However, it has the most coverage area and consistent RC of the SA EEZ. Notably, the string-of-pearl formation flying was investigated as a best effort to reduce the DG and was chosen above a trailing formation, which augments the satellites as one satellite with an effective larger swath-width and longer sensing time.

The second part of the chapter investigated AIS reception capabilities given the selected orbit. It conducts a probabilistic approach whether a vessel can be detected given the time the satellite observes the coast each pass. Furthermore, it introduces the problem that vessels from different SOTDMA-cells to broadcast simultaneously. This only becomes problematic when there are more than 3000 vessels in the satellite's FoV, all of which are broadcasting every 6 s. Fortunately, current AIS-receivers can distinguish vessels that broadcast simultaneously if they are far enough apart by using the Doppler frequency shift.

Thereupon, a communication link-analysis is performed by adding two antenna designs and real AIS-data to a simulation. The vessel's antenna is assumed to remain fixed in space by not tilting sideways; a calm ocean is assumed for this analysis. Furthermore, the backscatter from the ocean is investigated that degrades the signal strength over the horizon and only a 2.5° communication elevation is realisable. It is assumed that the CubeSat is unable to deploy a complex antenna solution, therefore, cannot use a helical antenna. Instead, a crossed-monopole antenna is suggested with its arms tilted 15° forward to focus the beam towards the satellite's

nadir. These antennas were simulated to determine the link's antenna gains as the satellite flies over, assuming that the satellite is always nadir-pointing.

The link analysis showed that there is a 95% message-reception rate with a near 100% reception probability above an elevation of 2.5°. This is a combination of the short period that the satellite senses the vessels below this elevation and the degraded vessel-antenna radiation patterns due to backscatter. Furthermore, 85% of the vessels are detected below and elevation of 30°. Therefore, a different antenna with a stronger gain on the horizon should be considered.

This chapter delivered promising results regarding AIS-reception given the selected RGT orbit that will allow for high data integrity as it has the most EEZ coverage. For this application, the EM samples captured by the AIS-decoder can be discarded and only the vessel positions, MMSI numbers, orientation, and speed need to be stored to predict future locations. This will allow the onboard storage to be effectively used and is deemed future work.

5. Image Processing

This chapter will discuss the proposed methodology to process remote images and is summarised in Fig. 5.1. Firstly, the image has to be pre-processed to acquire a salient image-composite that emphasizes regions of interest (RoI). This comprises the spectrum-selection, land-masking and a detector algorithm. The detector should identify RoIs within the image that may contain vessel-candidates. The detector should be chosen such that all the vessels in the image must be a subset of the RoIs. Next, the RoIs are extracted by thresholding the image-composite and grouping pixels to form binary large objects (BLObs). A BLOb is a group of connected pixels in an image that share a common property. However, their boundaries must be refined because thresholding is a course means of segmentation and will contaminate its shape.

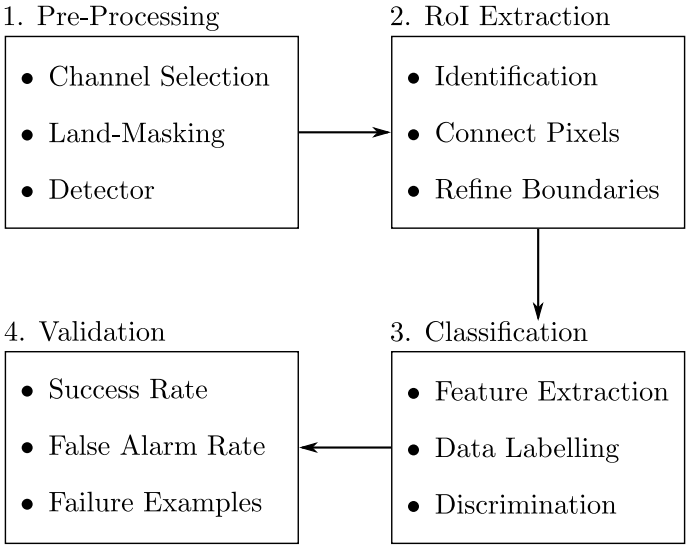

Figure 5.1: Image processing chapter summary - each heading is a section to follow. The chapter is structured such that the vessel-extraction process can be easily followed.

Penultimately, the BLObs must be classified as either vessel or non-vessel objects. This is accomplished by extracting features from each BLOb. As the satellite images used in this thesis are unlabelled, vessel and non-vessel objects must be manually labelled to identify features that strongly resemble each class. Finally, stages one to three, referring to Fig. 5.1, will be evaluated by determining the success and failure rates attempting to identify vessels similar to the examples depicted in Fig. 5.2.

The off-colour satellite image of Singapore, captured by SumbandilaSat, contains the most vessels of varying sizes and intensities, anomalies, and false alarms in the

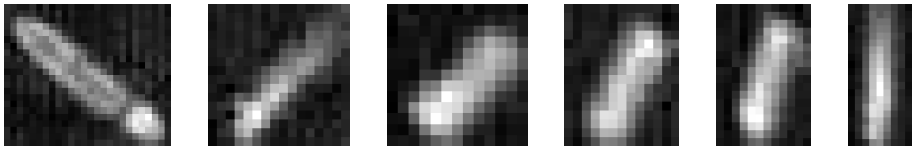

Figure 5.2: Six vessel examples with a 6.25 m GSD resolution. These images are captured by SumbandilaSat in 2009.

dataset. It was therefore decided to base feature extraction of the vessel and non-vessel candidates on this image. The image is off-colour as satellite's red colour sensor was inoperative during sensing. Furthermore, this image is JPEG-compressed; therefore, contains lossy-compression remnants visible in the horizontal en vertical axes that will contaminate its features and is further discussed in Sec. 5.3.

As vessel-features are based on the image of Singapore, the minimum image GSD for this thesis is chosen as 6.25 m GSD. At this resolution, small vessels become difficult to distinguish from complex sea surfaces and small clouds at a human level. Clear vessel candidates at this resolution is shown in Fig. 5.2 and they have distinct shape-features. It is also noted that the textures for each of the vessels differ, apart from a clear contrast with the background. However, the following vessel-detection difficulties in optical imagery were identified (see Appendix C) and are supported by Kanjir et al. [37]:

1. False alarms caused by difficult environments, from this point onwards referred to as *clutter*: complex sea states, clouds, islands, ports, noise and land-artefacts.
2. Vessel-reflectivity variations due to different illumination conditions and vessel-hull colours.
3. Vessels are indistinguishable from their wakes in most 5 m GSD optical PAN images.
4. Algorithm robustness strongly depends on the training data, which is based on SumbandilaSat's images.

5.1 Pre-Processing

This section will elaborate on the process of removing large objects from an image-composite, followed by filtering it with a detector algorithm. Conversely, this stage will introduce false alarms to be extracted along with the vessels. However, the goal of the pre-processing stage is to ensure that all the vessels will be included along with the false alarms.

Notably, vessel-detection algorithms designed for calm seas become vulnerable when introduced to difficult environments which is further discussed in Sec. 5.4. An exam-

ple of a vessel's reflectivity variations is depicted in Fig. 5.3, where **(a)** is a 15×15 pixel example of a vessel with an illuminated bridge-castle, depicted as blue, and forecastle, depicted as red, with a dark deck that blends in with the surrounding clutter. Furthermore, a 19×19 pixel vessel-example with a well-illuminated deck is shown in **(b)**. Conversely, the two illuminated areas of the vessel may appear as two small, convex and compact clouds and the vessel can be flagged as two false alarms. To detect the wrongly classified vessel in Fig. 5.3, the algorithm will require more spatial information regarding the texture in the vessel's proximity, which falls outside the scope of this thesis.

(a) **(b)**

Figure 5.3: Vessel reflectivity variation caused by different illumination.

5.1.1 Image-Composite

An image composite is created by combining two or more images; it reduces the dimensionality of the data whilst keeping important information from each dimension. Therefore, it was decided to mix the red, green and blue (RGB) channels to produce an image-composite to reduce computation and improve vessel extraction rather than processing the individual bands separately [51]. These spectra were chosen due to a lack of multispectral images containing many vessels and false alarms, in addition to the vessel features being based on the Singapore image.

An image-composite is stored as an unsigned 8-bit integer in a $L \times W$ array, where L and W are the number of columns and rows, respectively. The first entry, $(0, 0)$, is in the top-left and the y-axis increments downwards as depicted in Fig. 5.4. Lastly, the value stored at each entry is the grey-level intensity.

$$I(j,i) = \begin{array}{c} \\ j \downarrow \\ \\ \\ \\ \end{array} \overset{i \rightarrow}{\begin{array}{|c|c|c|c|} \hline 0 & 0 & 1 & 1 \\ \hline 0 & 0 & 1 & 1 \\ \hline 0 & 2 & 2 & 2 \\ \hline 2 & 2 & 3 & 3 \\ \hline \end{array}}$$

Figure 5.4: Image data format.

The contrast between vessels and their environment is not always obvious and can

lead to misdetections. As an attempt mitigate the number of false alarms, Yu et al. in [52] suggests an RGB-stretching algorithm to increase the contrast between ocean and non-ocean, shown in Eq. (5.1), and is limited to a value of 255, where α is chosen as 1.2 and ε is introduced to prevent dividing by zero. The functions R, G, and B denote each respective pixel's red, green, and blue value for each respective channel at positions j and i. For this thesis, RGB-stretching is used to create an image-composite, $\boldsymbol{P}_{\text{LM}}$, for land-masking rather than RoI extraction as its non-linear properties will cause a detector algorithm to produce many false alarms.

$$\boldsymbol{P}_{\text{LM}} = \begin{cases} \frac{\alpha R(j,i)B(j,i)}{G(j,i)+\varepsilon} & \text{if } B\left(j,i\right) \leq G\left(j,i\right) \\ \frac{\alpha R(j,i)G(j,i)}{B(j,i)+\varepsilon} & \text{if } B\left(j,i\right) > G\left(j,i\right) \end{cases} \tag{5.1}$$

A second image composite, $\boldsymbol{P}_{\text{DET}}$, is generated to best highlight RoIs for the detector algorithm. The Luma coding, used in PAL and NTSC systems, is used to generate a greyscale composite with the R and G channels Gaussian filtered to highlight anomalies in the ocean[1]:

$$\boldsymbol{P}_{\text{DET}} = \boldsymbol{g} * \left[0.299R\left(j,i\right) + 0.587G\left(j,i\right)\right] + 0.114B\left(j,i\right)$$

Where $\boldsymbol{g}$ denotes a Gaussian filter with a standard deviation of 10-pixels to enlarge smaller anomalies and make them easily detectable for the detector algorithm. This is to compensate for vessels with bright and dim regions that might segment during thresholding that will be discussed in Sec. 5.2. To preserve texture information, a third image-composite is created, $\boldsymbol{P}_{G}$, that follows the methodology for $\boldsymbol{P}_{\text{DET}}$ but is not Gaussian filtered.

5.1.2 Land-Masking

Land-masking is required because vessel detectors produce false alarms when applied to land [37]. $\boldsymbol{P}_{\text{LM}}$ is used to remove large regions, such as formations of clouds and land. Alternatively, one can detect coastlines and compare it to a ground truth using non-affine transformations but falls outside the scope of the thesis. False alarms are unavoidable and the goal of this process is to include all the vessels as RoIs for classification as discussed in Sec. 5.3.

To improve computation time and algorithm-robustness, $\boldsymbol{P}_{\text{LM}}$ is subsampled by selecting every fourth pixel, assuming that large-object information is not lost. Thereafter, the image-composite is median filtered with a 9×9 window. It includes pixels within a 100 m range of the pixel under inspection for a GSD of 6.25 m. Median filtering, depicted in Fig. 5.5, is a simple way of homogenously filtering an image as

[1]The greyscale for the SumbandilaSat images are generated as: $\boldsymbol{P}_{\text{DET}} = 0.114B\left(j,i\right) + \boldsymbol{g} * \left[1.164G\left(j,i\right)\right]$ to compensate for the missing R-channel. Green is Gaussian filtered to better highlight anomalies in the ocean

opposed to [53]. Gaussian filtering highlights small regions, whereas median filtering blends regions in an image for improved thresholding. It is a computationally inexpensive method of homogenising an image.

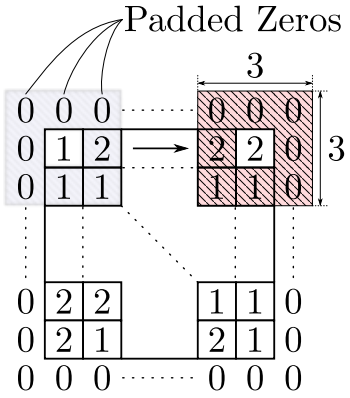

Figure 5.5: Median filter example with a 3×3 kernel filtering an image with intensities $\{0, 1, 2\}$. The filter is sliding over the image as indicated by the arrow, going from a blurred blue kernel towards a clear red kernel. The image is padded with zeros depending on the kernel size. In this example, the *red* kernel is evaluating the values $\{0, 0, 0, 0, 0, 1, 1, 2, 2\}$, where the new pixel value is the median of 0.

A median filtered image has a less noisy grey-level histogram, therefore, the foreground can more easily be separated from the background. After median filtering $\boldsymbol{P}_{\mathrm{LM}}$, an adaptive threshold is applied, followed by morphologically filtering the resultant-composite with a 10×10 star kernel to remove noise and small areas. Thereafter, the remainder of the non-ocean pixels are grouped together using a method described in Sec. 5.2.2 and the groups smaller than $1000\,\mathrm{m}^2$ are removed. Whereas, the ocean-pixel groups smaller than $50\,\mathrm{m}^2$ are removed from the mask. These values are calculated based on the image's GSD . Finally, the mask is upsampled to the original resolution and applied to $\boldsymbol{P}_{\mathrm{DET}}$ before filtering it with a detector.

Thresholding is used in remote-sensing applications for cloud and land removal because they exhibit significance in most reflective bands [37]. Histogram-based segmentation, known as Otsu's method or adaptive thresholding, is used for land-masking and it involves iterating through all the possible threshold values. Finally, the image is thresholded when the maximum *between-class* variance occurs:

$$\sigma_B^2 = \max_{T_L \in \{1,\ldots,L\}} \left[W_b W_f \left(\mu_b - \mu_f\right)^2 \right]$$

Where:

$$W_b = \frac{\sum_{i=1}^{T_L-1} H\left(i\right)}{L^2} \qquad W_f = \frac{\sum_{i=T_L}^{L} H\left(i\right)}{L^2}$$

$$\mu_b = \frac{\sum_{i=1}^{T_L-1} i \times H\left(i\right)}{\sum_{i=1}^{T_L-1} H\left(i\right)} \qquad \mu_f = \frac{\sum_{i=T_L}^{L} i \times H\left(i\right)}{\sum_{i=T_L}^{L} H\left(i\right)}$$

Where the background and foreground weights and means are denoted W_b and W_f, and μ_b and μ_f, respectively. The current iteration of the threshold is denoted T_L and the maximum grey level is denoted L. The image is thresholded where σ_B^2 occurs. Unfortunately, this method is not sufficiently sophisticated to separate land and clouds in areas of both high and low contrasts **"cite –Kanjir2018"**. Lastly, the mask is morphologically opened with a 5×5 star kernel to remove isolated pixels and retain diagonal shape information.

5.1.3 Detector

The detector algorithm generates a saliency map to identify RoIs within an image. Visual saliency measures the degree with which regions attract human attention to a scene [53]. Two detectors were considered for this thesis, namely the:

1. phase spectrum of the Fourier transform (PFT), and the
2. cell-averaging constant false alarm rate (CA-CFAR) filter.

The PFT has low computational complexity [53] and is described as:

$$\boldsymbol{S} = \boldsymbol{g} * \|\mathcal{F}^{-1}\left(e^{j\cdot\boldsymbol{p}}\right)\|^2$$

Where $\mathcal{F}$ is the Fourier transform, $\boldsymbol{p}$ is its respective phase spectrum, and $\boldsymbol{S}$ is the final saliency map. This method emphasises large intensity changes within an image; it is capable of highlighting clear-vessel areas, although it fails when a vessel is poorly illuminated and highlights the clutter surrounding it. Instead, this method has to be used to identify seeds for region growing and will have several false alarms.

The second considered detector algorithm, the CA-CFAR, assumes homogeneous clutter and provides a comparison statistic [54]. This detector is robust and is based on the CFAR detector, which will not be discussed in this thesis [55]. This detector can utilise statistic information of target and ocean clutter and is depicted in Fig. 5.6.

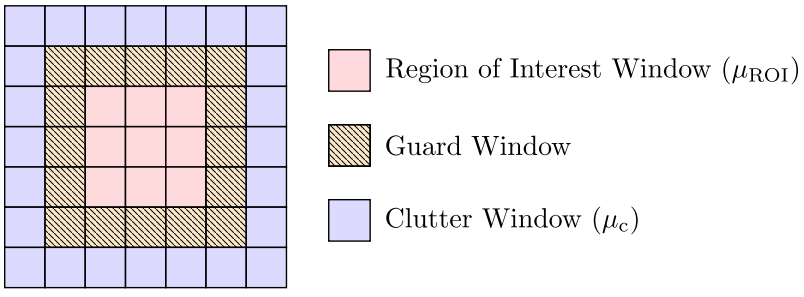

Figure 5.6: The CA-CFAR window configuration adapted from [54].

The detector is a square-matrix that is convolved with an image and generates two responses. The first response, μ_{RoI}, calculates the mean grey intensity within the RoI-window. The second response, μ_{c}, calculates the clutter's mean grey intensity

outside the RoI-window given a specific guard-window. The guard window is used to prevent the filter from including the inspection area in the clutter mean. Therefore, its pixels are ignored should the objects under evaluation be larger than the ROI window. Finally, the CA-CFAR is used to element-wise calculate an image-composite's power-ratio:

$$\boldsymbol{P}_R = \frac{\boldsymbol{\mu}_{\text{RoI}}}{\boldsymbol{\mu}_{\text{c}}}$$

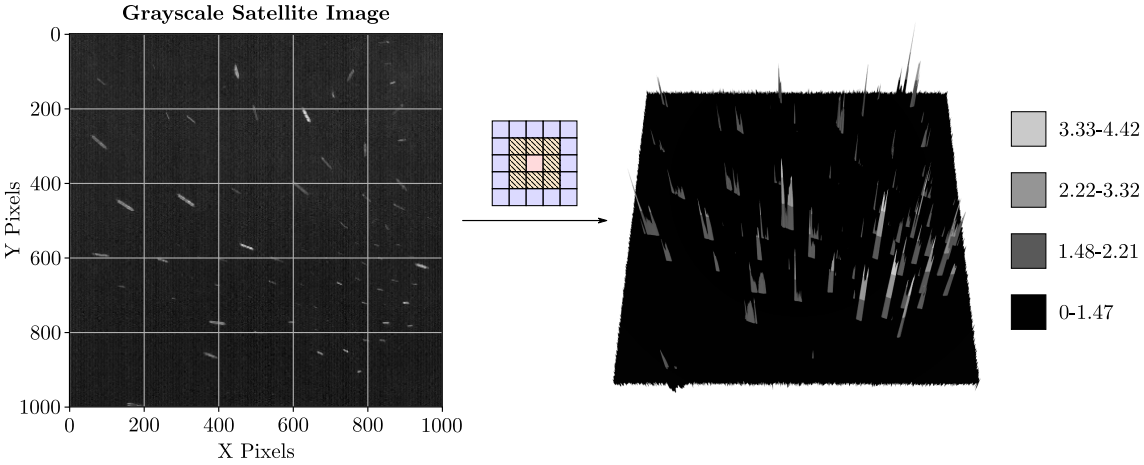

Figure 5.7: Greyscale satellite image CA-CFAR window response. Notably, there are CCD-bias remnants in the satellite image that appear as vertical lines induced onto the image as a result of the line-scan operation. The discrete CA-CFAR response is shown on the right-hand side that is used to empirically choose a threshold.

An example of the CA-CFAR filter response is depicted in Fig. 5.7 and is interpreted as the pixel-cluster intensity, μ_{RoI}, relative to its environment, μ_{c}. The size of the filter is chosen as a 27×27 kernel with respective window sizes of 3, 10, and 2, indicating a 3×3 RoI-window, 10-pixel-boundary guard window and a 2-pixel-boundary for the clutter window.

The RoI is chosen as small as possible to retain spatial information, the guard window is chosen large enough to separate the clutter from the RoI, and a 2-pixel clutter boundary provides sufficient information of the environment's grey-intensity. Furthermore, Fig. 5.7 shows that complex sea states' power ratio reduces to a value of one as noise is filtered out. Lastly, effects such as the CCD-bias offset is deemed negligible after filtered with a CA-CFAR.

A comparison between the PFT and CA-CFAR is shown in Fig. 5.8. The CA-CFAR result contains all the vessels in RoI with more false alarms. Conversely, the PFT misses actual vessels and only highlights clear vessel targets with less false alarms and rejects homogenous textures better. Moreover, the results from the CA-CFAR is more intuitive than the PFT, as pixel-cluster brightness relative to its environment is more clear. Therefore, it was decided to use the CA-CFAR for the remainder of this thesis.

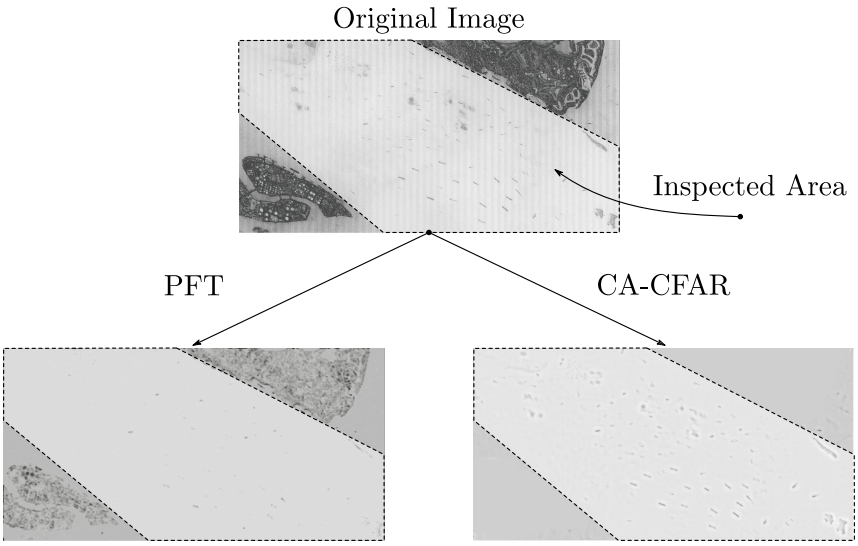

Figure 5.8: Two considered saliency maps. All the images are solarised with the Sabattier effect for clarity, the original image is the grey-scaled input image, the PFT and CA-CFAR image-composites are scaled between 0 and 255 to display the values as a greyscale image. The CA-CFAR example has been land-masked so only the vessel-candidates are under inspection.

5.2 Vessel Candidate Extraction

This section elaborates extracting vessels from RoI based on its number of pixels and grey intensities relative to its proximity. This thesis proposes a coarse-to-fine vessel detection strategy that will involve a candidate extraction and edge-refining stage. The extraction phase, depicted in Fig. 5.9, is a crucial step as it influences the vessel-classification's effectiveness and if it performs poorly it will invalidate RoI features. The vessel extraction phase focuses on step five in Fig. 5.9.

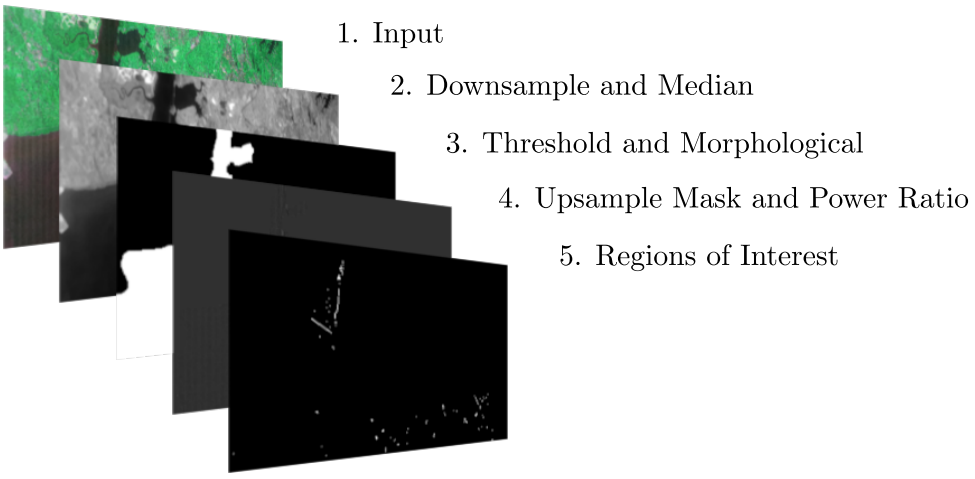

Figure 5.9: Summary of the pre-processing methodology.

5.2.1 Identification

The vessel regions are salient after the detector algorithm has been applied to it. Therefore, vessel-candidates can be obtained by coarse image segmentation with a proper threshold. It is assumed, and supported by empirical analysis, that RoIs containing a vessel will be 200% brighter than its environment.

However, the saliency map is thresholded at 1.5 to produce a binary image, $\boldsymbol{B}_{\text{DET}}$, that consists of regions that is 50% brighter than its proximity. This value is an intuitive guess, as bright parts of a vessel are much brighter than 100% of its proximity, but a value of 50% was chosen to retain more shape-information. Lastly, the binary image is morphologically closed if the GSD is less than 10 m with the following kernel:

$$\kappa = \begin{bmatrix} 0 & 0 & 1 & 0 & 0 \\ 0 & \mathbf{1} & 1 & \mathbf{1} & 0 \\ 1 & 1 & 1 & 1 & 1 \\ 0 & \mathbf{1} & 1 & \mathbf{1} & 0 \\ 0 & 0 & 1 & 0 & 0 \end{bmatrix}$$

If the GSD is larger than 10 m, the image is dilated with κ to connected nearby pixels. This will increase the number of false alarms but improve detection of smaller vessels. The star-kernel, κ, was chosen instead of a square kernel to avoid losing shape-information. Furthermore, κ is an adaptation of the normally used star-kernel with the addition of four 1's, indicated with bold numbers, around the centre to grow pixels in close-proximity diagonally.

By grouping relatively bright pixels, a vessel's wake will be included and it will contaminate a small vessel's features, effectively increasing the probability that the vessel will be rejected during the classification phase. This will occur when it abruptly changes its course, resulting in a shape with a much larger convex hull than its actual area. A vessel's wake can be used to determine its heading but falls outside the scope of this thesis.

5.2.2 Connect Pixels

This subsection will elaborate on the chosen methodology to group pixels in a binary image. For this thesis, pixels are considered connected based on their eight-neighbouring pixels as depicted in Fig. 5.10. Alternatively, vessels can be connected based on their four-neighbouring pixels, omitting pixels on its diagonal. However, vessels are generally oblique and this method will increase computation time.

An adapted connected-component labelling (CCL) was developed to group isolated binary pixels as BLObs, whilst discarding regions exceeding a pixel-number threshold. The algorithm is depicted in Fig. 5.10 and described in algorithm C.1, it sweeps across a binary image from left to right, top to bottom. Therefore, the pixels beneath and to the right of the inspected pixel are not assessed and the area of inspection is

L-shaped. Afterwards, the pixels are grouped based on the values generated by S, as expressed in algorithm C.1. CCL applies a label to pixels in each other's proximity. However, the execution time lengthens with the number of labels. Usually, a concave shape will have more labels than a convex shape given the same number of pixels.

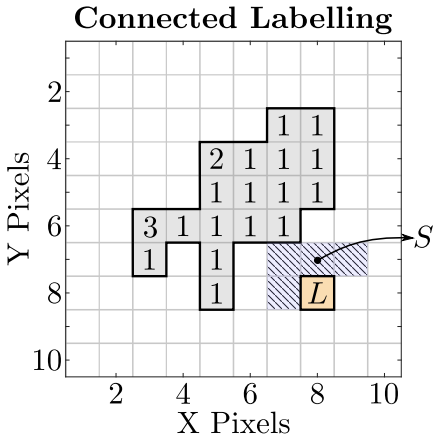

Figure 5.10: Connected component labelling process, where the pixel under inspection, depicted as a yellow pixel and denoted L, is equal to the smallest value in set S that encompasses all the unique values in the hatched, blue, L-shaped region. It contains the west, north-west, north and north-east neighbouring pixel labels. This set is updated as the sliding window, the L-shaped box, moves across the binary image. If S is empty then L incremented by 1. Therefore, in this example, L will be equal to 4 and the two BLObs will identified by pixels having labels $\{1, 2, 3\}$ and $\{4\}$.

The labels of an inspected area are discarded if its number of pixels fall below 10 or is larger than $458 \times 68 \times 1.2 \approx 950$ for a GSD of 6.25 m. This value is based on the largest vessel to date, the Mont oil tanker, with a 20% tolerance to compensate for its wake and possible noise. Thereafter, the brightest pixel in each BLOb is used as a seed for a region growing algorithm to refine its shape and is discussed in the next section.

5.2.3 Refined Segmentation

The global threshold segmentation results are coarse due to edge localisation errors that are compounded by the distortions caused by channel-mixing and the detector algorithm. Therefore, a refined segmentation is desirable for shape and local textures analysis. Such a technique uses relative pixel positions accompanied by their grey-level similarities, known as *region-growing* and is depicted in Fig. 5.12. A similar algorithm was implemented on PoSat-1 to detect cloud-candidates in remotely sensed images.

Remote images of the ocean typically have a grey-level distribution with little variation. Consequently, an obvious edge exists between a bright vessel and its environ-

ment that can be region-grown to stop at its edge. However, this will include the wake of a vessel as part of the BLOb, see Fig. 5.15.

The region-growing is performed on an image-composite that consists of $\boldsymbol{P}_{\mathrm{G}}$ overlaid with a Gaussian filtered image-composite, using a 3×3 kernel, that consists of $\boldsymbol{P}_{\mathrm{G}}$'s highlighted edges, generated using the Sobel-operator, and $\boldsymbol{B}_{\mathrm{DET}}$ to increase the RoIs' contrast with its environment [55]. This will impel the region-growing to stop at the vessels' contour. The image-composite's dimensions have an aspect ratio of 1:1 and the largest dimension of the corresponding BLOb is used to determine the new image-composite's size. Should the dimension be less than 100 pixels, it is incremented by 10 pixels.

The resultant image-composite is imposed onto $\boldsymbol{P}_{\mathrm{G}}$ and the process is described in Eq. (5.2) where S is the Sobel-operator defined as the magnitude of $\boldsymbol{P}_{\mathrm{G}}$'s filter response to two 3×3 kernels that approximates its j- and i-gradients as:

$$\boldsymbol{G}_i = \begin{bmatrix} -1 & 0 & +1 \\ -2 & 0 & +2 \\ -1 & 0 & +1 \end{bmatrix} * P_{\mathrm{G}}(j,i) \qquad \text{and} \qquad \boldsymbol{G}_j = \begin{bmatrix} -1 & -2 & -1 \\ 0 & 0 & 0 \\ +1 & +2 & +1 \end{bmatrix} * P_{\mathrm{G}}(j,i)$$

Where the Sobel-operator is defined as:

$$S \circ P_{\mathrm{G}}(j,i) = \sqrt{\boldsymbol{G}_i^2 + \boldsymbol{G}_j^2}$$

$$\tilde{P}_{\mathrm{G}}(j,i) = P_{\mathrm{G}}(j,i) + \boldsymbol{g} * [S \circ P_{\mathrm{G}}(j,i) + 0.5 \cdot B_{\mathrm{DET}}(j,i)] \tag{5.2}$$

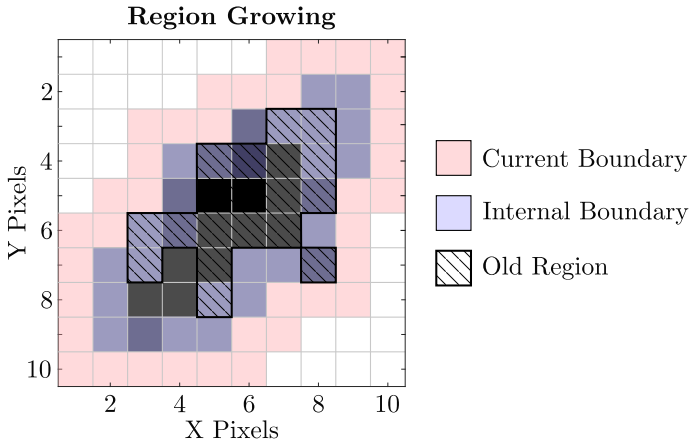

Figure 5.11: Region growing with lenient stopping criteria applied to a grey BLOb with four intensity levels. The region is grown to the internal boundary (IB), indicated with a blue tint. The next pixel to be added is chosen from the current boundary (CB), indicated with a red tint. The original BLOb is depicted as the hatched region.

Each BLOb's brightest pixel in $\tilde{\boldsymbol{P}}_{\mathrm{G}}$, as per Eq. (5.2), is used as a seed for the region-growing. The algorithm grows outwards in an eight-connected pixel approach and is

depicted in Fig. 5.11. Initially, the current region (CR) and the internal boundary (IB) is the brightest pixel with the current boundary (CB) the eight neighbouring pixels. The algorithm searches the CB for the brightest pixel and adds it to the IB. A pixel is removed from the IB if it is not connected to the CB. The algorithm executes until each pixel has been assigned. Thereafter, the stop-criteria, or segmentation point calculated as depicted in Fig. 5.12.

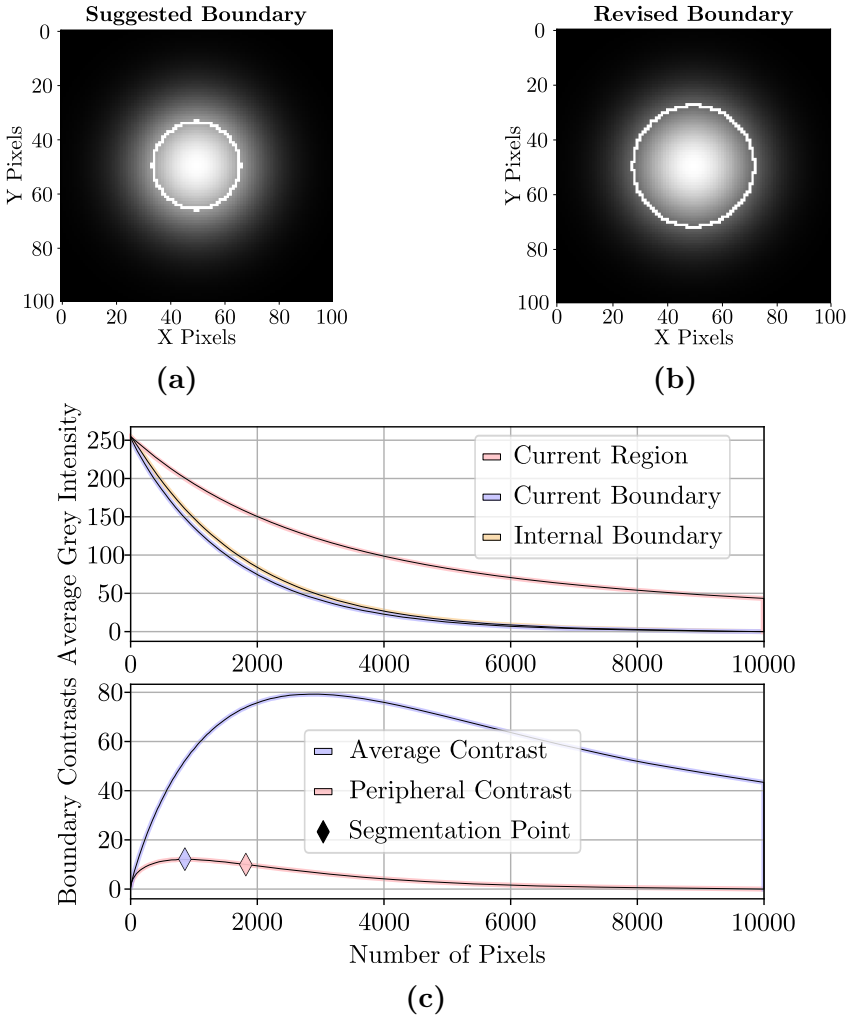

Figure 5.12: Segmentation results for a 100×100 Gaussian with a standard deviation of 17 pixels recreated from [36]: **(a)** Suggested boundary. **(b)** Revised boundary. **(c)** Mapping for the grey levels, PC and AC, obtained during region growing. The segmentation point is indicated with a blue and red ♦ for figures (a) and (b), respectively.

The segmentation described in [36] is chosen to bound a cloud-region. It calculates the difference between the CR and CB, and the IB and CB, referred to as the average- and peripheral-contrast (AC and PC), respectively. The segmentation point is determined by the last PC's local maximum prior to the AC's global maximum, shown as a blue diamond in Fig. 5.12. Notably, when the region-growing is applied

to a 2-D Gaussian in the form:

$$G\left(j,i\right) = 255 \cdot e^{-\frac{j^2+i^2}{2\sigma^2}}$$

As depicted in Fig. 5.12 **(a)**, the grown region does not contain spatial information regarding the region's environment. Therefore, it was decided to modify the stopping criteria to be more lenient and produce the resultant image in Fig. 5.12 **(b)**.

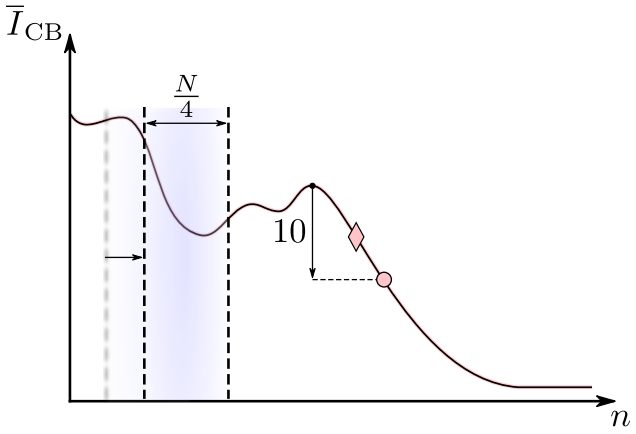

Figure 5.13: Depiction of the sliding window used in the adapted region-growing algorithm.

For vessel detection, the surrounding environment contains spatial information required for classification. Consequently, the manner in which the segmentation point for the region-growing is acquired as depicted in Fig. 5.13, where $\overline{I}_{\text{CB}}$ is the CB's mean grey-intensity and n is the number of image pixels that are grown. The sliding window has length $\frac{N}{4}$ and searches for a local minimum, $\bullet$, with a grey-prominence of 10, where N is the number of pixels in the BLOb. The sliding window's length was chosen to scale with the BLOb-size as the vessels have varying sizes. Finally, the segmentation point, $\blacklozenge$, is at n =90% of the grown pixels at $\bullet$. These values were empirically chosen to best grow a region into the background. The region-growing is restricted from growing the entire $\tilde{\boldsymbol{P}}_{\text{G}}$ as some false alarms have their minimum peak at the end of the CB curve. Lastly, the segmentation point is chosen as 90% of the final value to restrict the algorithm from unnecessarily branching into the background of a noisy or unclear RoI. Clear vessel candidates have a bright and homogeneous texture and it is assumed that if the CB's intensity decreases by 10 within a sliding window of length $\frac{N}{4}$, the algorithm is growing too deep into the environment.

Fig. 5.14 depicts the adapted region-growing performed on an RoI. When clutter is introduced as per (b), the region grows into the background as seen in the bottom-right corner. Lastly, the extracted regions are shown in (c) and it is clear that the object is successfully segmented from the environment and slightly grows into the background. Furthermore, a second object is extracted in the bottom-right corner the is due to clutter and will be discarded as an obvious false alarm.

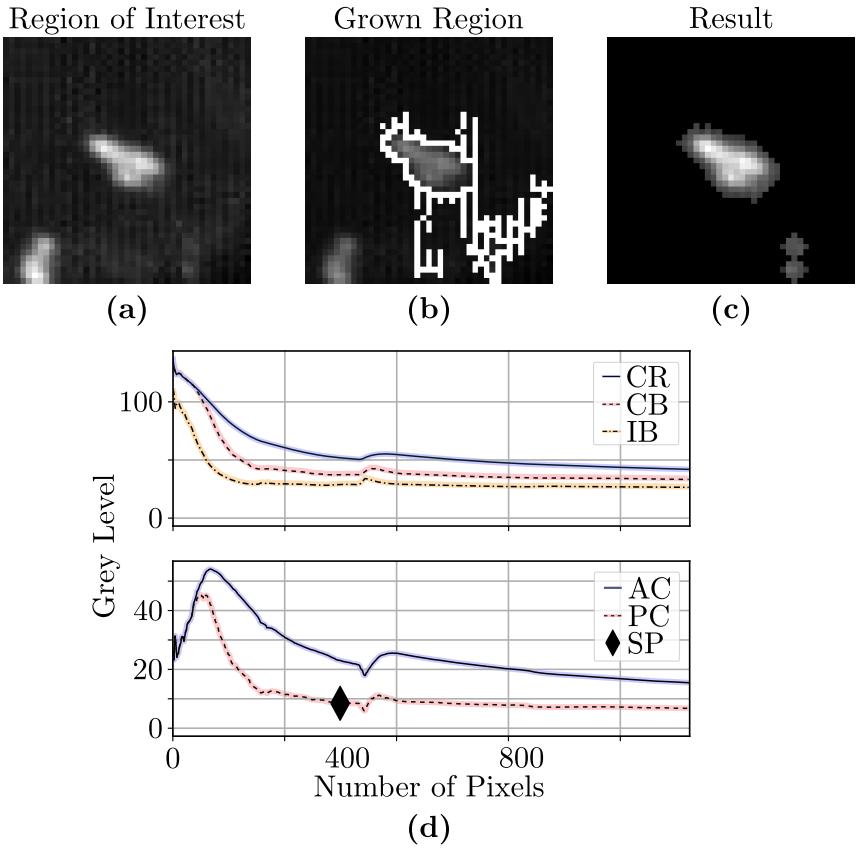

Figure 5.14: BLOb edge refinement.**(a)** is the preliminary identified BLOb, **(b)** is the adapted grown region, **(c)** is the final result after removing the darker pixels and morphologically refining the edge, and **(d)** is the region-growing grey levels.

Principal component analysis (PCA), explained in the next paragraph and is also used to extract a BLOb's shape features and orientation, is performed on all the pixels brighter than one standard deviation from the RoI's mean intensity, $\bar{I} + \sigma_{II}$. These pixels are chosen as they represent the RoI's orientation, which in the case of vessels is similar to a multivariate Gaussian distribution. This is used to calculate the mean, $\overline{I}_{\mathrm{PCA}}$, and standard deviation, $\sigma_{\mathrm{II,PCA}}$, of the pixels' grey-intensities that lie within one standard deviation of the second principal component (semimajor axis, $\boldsymbol{\nu}_2$) of the first principal component (major axis, $\boldsymbol{\nu}_1$) acquired from PCA and is depicted in Fig. 5.15. Penultimately, the pixels that fall below $\bar{I}_{\mathrm{PCA}} - \sigma_{II,\mathrm{PCA}}$ are removed from the BLOb. Finally, the resultant BLOb is morphologically opened and dilated with a 3×3 star-kernel to connect isolated pixels from the aforementioned process and is depicted in Fig. 5.15. Should two new BLObs exist, they are treated as two new RoIs and the process is repeated.

PCA is a mathematical tool used to extract a linear components of an orthogonal basis set in the order of largest variance. This is achieved by considering all the

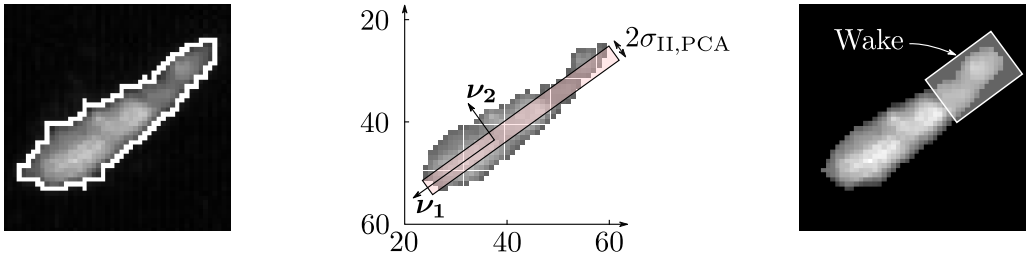

(a) **(b)** **(c)**

Figure 5.15: PCA applied to the resultant grown region. The grown region's IB is shown in **(a)** as a white pixel border. **(b)** depicts the pixels that have been removed from grown region based on their intensity values. The principal components are indicated with two vectors, $\boldsymbol{\nu}_1$ and $\boldsymbol{\nu}_2$, with the vector-length corresponding with the variance. The pixels used to calculate the $\overline{I}_{\text{PCA}}$ and $\sigma_{II,\text{PCA}}$ lie within the red box that stretches out one standard deviation of the second principal component, $\boldsymbol{nu}_2$. The refined RoI is shown in **(c)** where the vessel's wake is notably part of the RoI and indicated with a white box.

BLOb's j-, j_b, and i-coordinates, i_b, to calculate their co-variance matrix:

$$\boldsymbol{C} = \begin{bmatrix} \text{cov}\left[\boldsymbol{j_b}, \boldsymbol{j_b}\right] & \text{cov}\left[\boldsymbol{j_b}, \boldsymbol{i_b}\right] \\ \text{cov}\left[\boldsymbol{i_b}, \boldsymbol{j_b}\right] & \text{cov}\left[\boldsymbol{i_b}, \boldsymbol{i_b}\right] \end{bmatrix}$$

Where each respective covariance matrix-entry is calculated as:

$$\text{cov}\left[\boldsymbol{j}, \boldsymbol{i}\right] = \frac{1}{N-1} \sum_{n=1}^{N} \left(j_n - \overline{j}\right)\left(i_n - \overline{i}\right)$$

Where N is the number of pixels and the overline denoting the respective means. The covariance is used to calculate the principal components by calculating the covariance matrix's eigenvalues. The eigenvalues are a measure of each principal component's variance and is calculated as:

$$|\boldsymbol{C} - \lambda \boldsymbol{I}| = 0$$

Whereas, the eigenvectors indicate the direction of variance for each eigenvalue and is calculated as:

$$\boldsymbol{C\nu} = \lambda \boldsymbol{\nu}$$

Where λ denotes the eigenvalues, $\boldsymbol{I}$ the identity-matrix, and $\boldsymbol{\nu}$ is the eigenvectors. Assuming no image distortions, a vessel's orientation is calculated as expressed in Eq. (5.3) where $\nu_{1,1}$ and $\nu_{1,2}$ are the respective i- and j-components of the eigenvector with the largest corresponding eigenvalue that lies along the vessel's body.

$$\varphi_v = \arctan\left(\frac{\nu_2}{\nu_1}\right) \tag{5.3}$$

5.3 Vessel Classification

Unique vessel-features have to be identified to discriminate them from their environment, mainly comprising clouds, ocean waves, and land-remnants. This section will elaborate on the chosen methodology for vessel-classification. Eight unique vessel-features, that will be discussed in Sec. 5.3.1, were identified as follows:

f_1 - Number of pixels,	f_5 - Luminosity,
f_2 - Eccentricity,	f_6 - Correlation,
f_3 - Compactness,	f_7 - Contrast, and
f_4 - Convexity,	f_8 - Energy

It is not feasible to detect vessels smaller than 20 m using a 6.25 m GSD and the GSD should be a third of the vessel size to successfully detect it [56]. Therefore, as the resolution degrades the vessel-dimensionality will appear more dispersed and less eccentric. Distinctive vessel-features encompasses their long and thin shape and high inertial ratio that is used to eliminate obvious false candidates [55]. Notably, a vessel's most dominant features are its shape and its textural features will be used to distinguish it from clutter. Rotation-invariant descriptors were considered but misclassified concave shapes. Therefore, the vessel orientation, φ_v, is used to extract features f_2, f_5, f_6, f_7, f_8.

5.3.1 Feature Extraction

The features can be divided into four shape and four textural descriptors. This subsection will elaborate on how to extract the aforementioned features.

5.3.1.1 Shape Features

After image segmentation, shape analyses is performed to remove obvious non-vessel RoI such as large or small islands and clouds. Zhu et al. suggests in [55] that vessels have an eccentricity of 1.35 and can be used to distinguish a vessel from a false alarm. Eccentricity in this chapter differs from the rest of the thesis: eccentricity is a shape length divided by its width. In the dataset generated for this thesis, as discussed in Sec. 5.3.2, the vessel- and non-vessel-classes have respective eccentricities of 2.6 and 1.9. Therefore, when introduced to a difficult environment with a GSD of 6.25 m, different features will be required, . Referring to Fig. 2.9, small clouds are the most difficult to distinguish from vessels due to their textural-variance, random grey distributions, and no definite shape [55].

The vessel's length-width-ratio is approximated by the PCA's eccentricity, which is the magnitude of the first principal component divided by the second. Additionally, it is used to determine the orientation of the BLOb and can be compared to the AIS data to identify vessels. The compactness gives a measure on the vessel's circularity

and is defined as:

$$f_3 = \frac{(\text{Perimeter})^2}{4\pi f_1}$$

Where the perimeter is calculated as the number of pixels not having eight neighbouring pixels. Lastly, the fourth chosen shape-descriptor is the BLOb's convexity that is its area, or the number of pixels, divided by its convex hull and is depicted in Fig. 5.16. The convex hull was calculated using Python 3.6's `skimage` package called `convex_hull_image`.

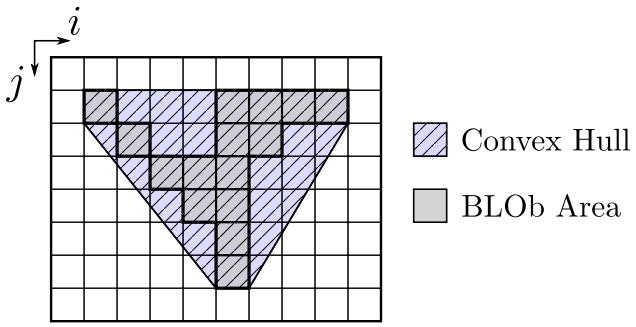

Figure 5.16: Convex hull of a BLOb. The BLOb's area is depicted in grey and the convex hull area is indicated with an overlaid hatched region where the difference is indicated with a blue tint.

5.3.1.2 Textural Features

A RoI's luminosity its brightness along its first principal component, ν_1, relative to its proximity. The luminosity, ι, is defined as:

$$\iota = \frac{\overline{I}_\sigma^2}{\overline{I}_\varrho}$$

Where $\overline{I}_\sigma$ is the object's mean intensity within the red box as depicted in Fig. 5.15b and $\overline{I}_\varrho$ is the mean grey-intensity of the pixels that lie outside this box.

The texture is essential when small greyscale-image areas are independently processed [57]. The texture features are extracted from a grey-level co-occurrence matrix (GLCM), depicted in Fig. 5.17.

The GLCM is derived from the angular relationships and distances between neighbouring pixel-pairs in the image. It counts the number of unique pair-instances and constructs a new matrix based on their cumulation. The intensities under inspection lie along the j axis and are compared with the intensities on the i axis. Suppose a greyscale image, $\boldsymbol{I}$, with N_G grey levels, its GLCM is a $N_G \times N_G$ matrix denoted $\boldsymbol{P}$. The $(j,i)^{\text{th}}$ entry in a normalised GLCM is $\frac{P(j,i)}{R}$, where R is the normalising factor. Therefore, the GLCM can be seen as a probability matrix in the sense of the number of neighbouring occurrences.

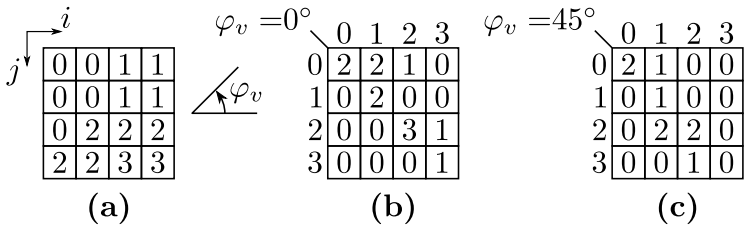

Figure 5.17: GLCM adapted from [57]. **(a)** is an example of a 4×4-image with numbers indicating grey intensities, and matrices **(b)** and **(c)** are generated using matrix **(a)** and are its respective GLCMs for a distance of 1 pixel and angle of 0° and 45°, respectively.

The GLCM angular relationship, denoted φ_v in Fig. 5.17, corresponds with the vessel's orientation expressed in Eq. (5.3). This is used to keep textural information along the vessels body, assuming that it correlates strongly with its orientation. Penultimately, the GLCM is made symmetrical as the direction in which the vessel is pointing towards is unknown as wake detection falls outside the thesis scope. Finally, normalisation is done after the GLCM is made symmetrical.

The final three features are extracted from the GLCM and are: correlation, contrast and energy. The correlation is a measure of the texture's grey-tone linear-dependencies. It describes the correlation between pixel means and whether there is a predictable relationship between the neighbouring pixels. The contrast, also called the inertia, is a measure of rapid change in intensity, whereas the energy is the square root of the texture's angular second moment. These descriptors are formally defined in Eqs. (5.4) to (5.6) where the GLCM's means, μ_x and μ_y, and standard deviations, σ_x and σ_y, are required to calculate feature f_6 and defined as:

$$\mu_x = \sum_{j=1}^{N_G}\sum_{i=1}^{N_G} i \cdot P(j,i) \quad \text{and} \quad \mu_y = \sum_{j=1}^{N_G}\sum_{i=1}^{N_G} j \cdot P(j,i)$$

$$\sigma_x^2 = \sum_{j=1}^{N_G}\sum_{i=1}^{N_G} P(j,i)\,(i-\mu_x)^2 \quad \text{and} \quad \sigma_y^2 = \sum_{j=1}^{N_G}\sum_{i=1}^{N_G} P(j,i)\,(j-\mu_y)^2$$

$$f_6 = \frac{1}{\sigma_x \sigma_y}\sum_{j=1}^{N_G}\sum_{i=1}^{N_G} \frac{P(j,i)}{R}\left[(i-\mu_x)(j-\mu_y)\right] \tag{5.4}$$

$$f_7 = \sum_{j=1}^{N_G}\sum_{i=1}^{N_G} \frac{P(j,i)}{R}(j-i)^2 \tag{5.5}$$

$$f_8 = \sqrt{\sum_{j=1}^{N_G}\sum_{i=1}^{N_G}\left[\frac{P(j,i)}{R}\right]^2} \tag{5.6}$$

5.3.2 Data Labelling

This subsection discusses the required labelling-process that was undergone to automate vessel-classification. Each feature-set requires a class with which to identify trends for vessel and non-vessel RoIs to improve discrimination accuracy.

For this process, 1129 RoIs were classified within the Singapore image. These RoIs were extracted and classified manually using a Python interface. The labelling process was repeated until satisfactory classification was achieved; after each iteration, the author evaluated the results by assessing the entire image's classified vessel RoIs.

The process was performed as illustrated in Fig. 5.18, where the input image is a subset of the Singapore image to reduce memory usage. The RoIs are manually labelled under the author's discretion; each RoI is extracted, along with its eight features, numbered 1-8 in Fig. 5.18, to act as a classification-aid. Three label options are presented: *no*, *maybe* and *yes*. Options *no* and *yes* adds the BLOb under inspection to the non-vessel, class 1, and vessel, class 0, classes, respectively. *Maybe* is selected if the RoI is indistinguishable, upon which the RoI is discarded to prevent corrupting distinctive vessel or non-vessel features.

Afterwards, classified vessels are highlighted in the image and inspected to assess the training set's accuracy. Referring back to Fig. 5.18, the vessel RoIs are indicated in green, whilst the non-vessel RoIs are indicated in red. Notably, the region highlighted with a white oval is an example of an obvious misclassification made by the author as this is an island. Training sets are discussed in the next section. Notably, each iteration yielded different results with the obvious RoI remaining constant and unclear RoI varying. Consequently, an automated classification will have similar accuracy when assessing RoIs with high certainty for obvious vessels and low certainty for unclear RoIs.

Upon satisfactory completion, 632 vessel and 497 non-vessel RoI were identified. The non-vessel RoIs mainly consisted of land, ports, clouds, waves and noise. Notably, no RoI were discarded in the final training set.

5.3.3 Discrimination

Classical image processing techniques used in Sec. 5.2 lack robustness when used for object classification in complex remote sensed images [52]. Therefore, for this thesis a supervised binary classification machine learning technique, called a support vector machine (SVM), is used to classify RoI to best resemble the training set acquired in the previous subsection. Supervised machine learning techniques require data with which to train a model (SVM), called a training set.

Labelled features can further be evaluated to determine their significance. The features are summarised in Table 5.1, where distinctive features have means separated

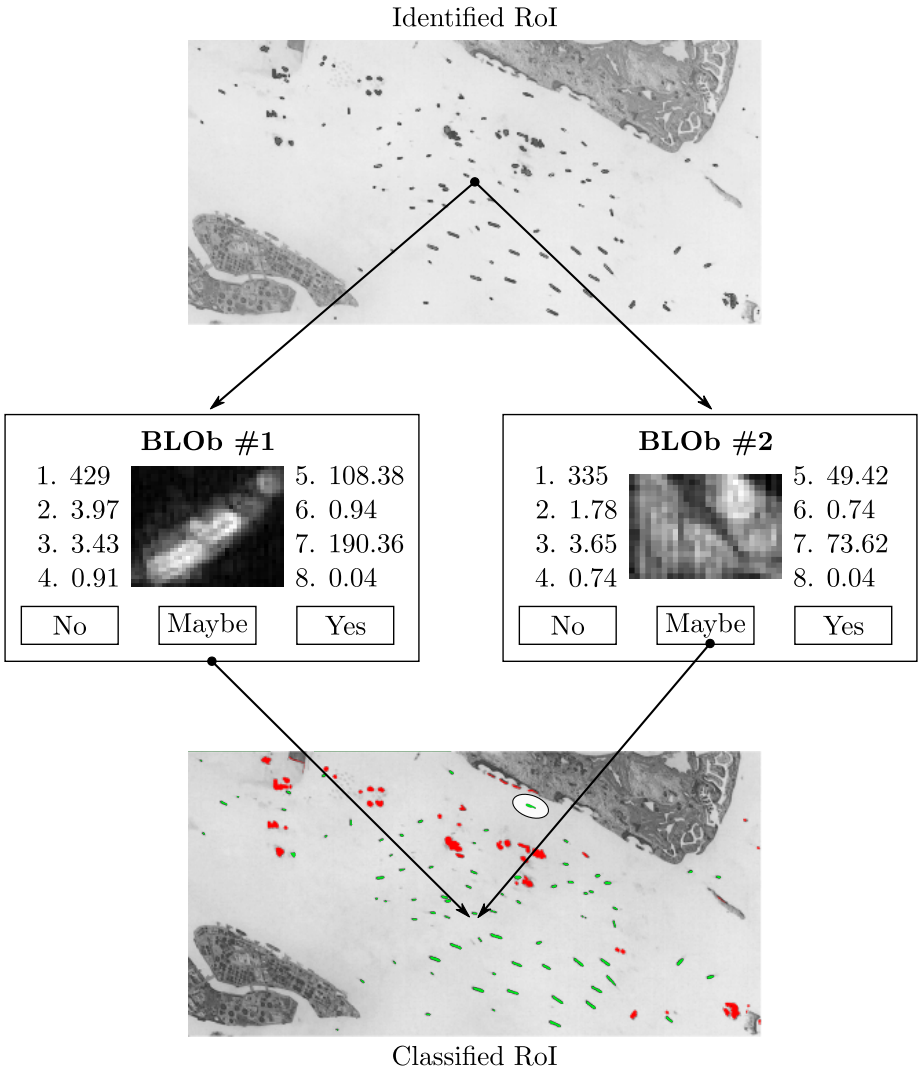

Figure 5.18: Depiction of the RoI-Classification process.

by at least one standard deviation. Consequently, the most distinctive features are f_5 and f_6, even though they overlap they can be classified using other features. Ideally, features should have little variance for it to be easily separable. Lastly, the features' range can vary significantly and should be normalised. Table 5.1 was inspected to manually generate a second feature set with reduced interclass variance by transforming the initial feature set using non-linear transformations, elaborated in Fig. 5.19.

Furthermore, it was decided to train an SVM on the initial set, from this point onwards referred to as the linear set, and the non-linear feature-set, to compare their results. The non-linear feature set was deduced from empirical analysis under the author's discretion as best to mitigate interclass variance. The figures in Fig. 5.19 demonstrate non-linear combinations of the aforementioned transformations. It was chosen the keep the distinctive feature f_6 and a feature that was found to scale with the other features, f_1, and to combine the remaining features into groups of four.

Table 5.1: Statistical feature description. The features are divided into vessel (V) and non-vessel (N) features where range is denoted D, the mean is denoted with an overline, and the standard deviation is denoted with σ.

Feature	D_V	D_N	$\bar{V}$	$\bar{N}$	σ_V	σ_N
f_1 - Number of Pixels	604	1704	123.00	122.51	104.92	174.79
f_2 - Eccentricity	6.01	14.11	2.55	1.90	1.15	1.48
f_3 - Compactness	4.38	12.36	2.08	2.00	0.75	1.53
f_4 - Convexity	0.299	1.00	0.94	0.93	0.04	0.11
f_5 - Luminosity	273.66	269.33	101.26	73.76	44.99	36.00
f_6 - Correlation	0.53	1.20	0.87	0.79	0.08	0.16
f_7 - Contrast	965.33	1055.00	130.99	110.65	112.87	110.92
f_8 - Energy	0.10	0.10	0.06	0.06	0.02	0.02

Notably, all of the features significantly overlap because small and large vessels form part of the same set, with f_6 overlapping the least.

Referring to Fig. 5.19, **(a)** is the normalised compactness, f_3/f_2, as a function of the number of pixels, f_1. **(b)** is the natural logarithm of the normalised convexity with an offset of $\varepsilon = 1 \times 10^{-4}$ to remove all the convexities having a value of 1 because they are indistinguishable and associated with smaller candidates. **(c)** combines the natural logarithm of luminosity, f_5 as a function of the normalised compactness. Finally, **(d)** is the correlation, f_6 as a function of the textural distance measure, $\ln(f_7/f_8)$. This feature is non-intuitive with no interpretation but better separates the classes, according to the author's understanding.

An SVM transforms the features into a higher dimensionality and finds a separating hyperplane with the maximum distance between classes of data. An initial guess is that vessel-features are simple; therefore, a linear kernel-function was chosen that uses a radial basis function kernel instead of a linear one, as the prior yielded improved results. A discussion elaborating on the different kernel functions will not be in this thesis.

A linear SVM was implemented using the Python 3.6 `sklearn`-package's `SVC` with the parameter `kernel='linear'`. The data frame is normalised before parsing it to the SVM classifier to improve training time under the assumption that the features are independent. However, as the features in Table 5.1 exhibit interclass variance, a more sophisticated classifier will be required to maximise the distances to the SVM's hyperplane but falls outside the thesis scope. Machine learning enables a more robust solution and future work is required for refining a solution that will produce improved results.

A supervised machine learning method's effectiveness is evaluated using a F1-score

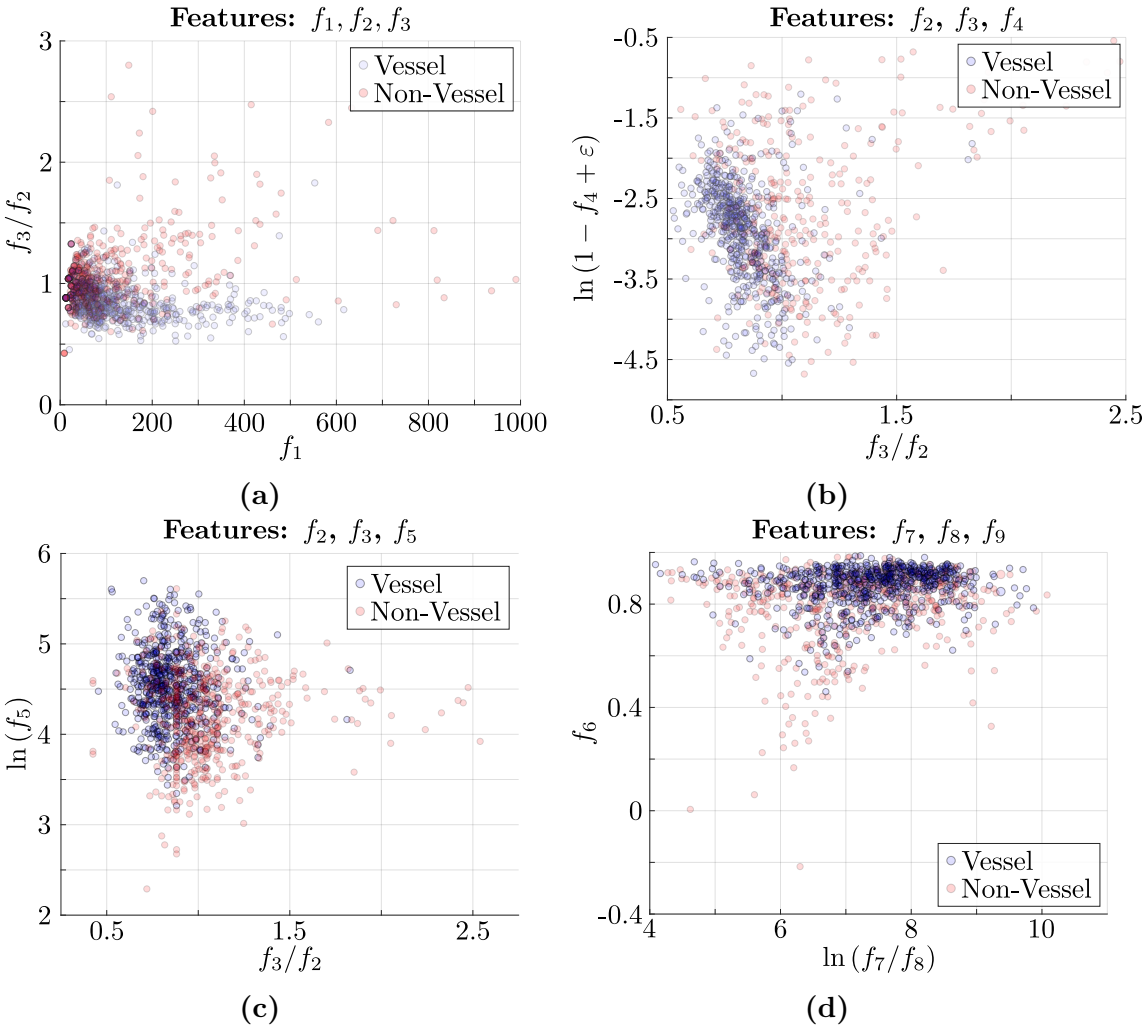

Figure 5.19: Non-linear feature sets depicting class overlap.

(Fisher score) and a confusion matrix. The F1 score is calculated as:

$$\text{F1-Score} = \frac{2 \times \text{precision} \times \text{recall}}{\text{precision} + \text{recall}}$$

Where:

$$\text{Precision} = \frac{TP}{TP + FP} \quad \text{and} \quad \text{Recall} = \frac{TP}{TP + FN}$$

With TP, FP, and FN denoting the true positives, false positives, and false negatives, respectively, where positive and negative denote classes 1 and 0. Precision is an indication on how accurate the positives are, whereas recall indicates the positives correctly predicted. Finally, the F1-score conveys the overall performance as a balance between the precision and recall. Lastly, a confusion matrix is a summary of the classifier's results as:

$$\boldsymbol{C}_M = \begin{bmatrix} TP & FP \\ FN & TN \end{bmatrix}$$

Furthermore, the SVM's accuracy is evaluated by using five-fold cross-validation, which is deemed an acceptable amount for a training set consisting of 1129 examples. If the training-set was larger, more cross-validation could have been performed for a better estimation of the classifier's accuracy. Moreover, cross-validation is used to estimate the effectiveness of a machine learning model on unseen data. It generally results in a less biased and optimised estimate than the F1-score.

Cross-validation is achieved by shuffling the dataset randomly into five groups. Each unique group is either a hold-out or test dataset. The remaining groups are used as training datasets. A model is fitted onto the training sets and evaluated on the test set. This resulted in the linear and non-linear feature sets having accuracies of 0.69 ± 0.14 and 0.71 ± 0.16, with F1-scores of 0.68 and 0.71 with respective a confusion matrices of:

$$\boldsymbol{C}_{\mathrm{M,L}} = \begin{bmatrix} 376 & 171 \\ 177 & 407 \end{bmatrix} \quad \text{and} \quad \boldsymbol{C}_{\mathrm{M,NL}} = \begin{bmatrix} 405 & 142 \\ 186 & 398 \end{bmatrix}$$

These results show that the non-linear feature sets perform better and that fewer vessels get misclassified as non-vessels. However, more non-vessels get classified as vessels which is deemed acceptable, as more TPs will assist point set registration algorithms to best compare RoI's locations to vessels' locations acquired from AIS-data. Point set registration algorithms align two sets containing points and estimates the transform from one to the other. It can be used to determine the locations of vessels that do not broadcast AIS messages but will require less FP and FN. This is deemed as future work and will not be further discussed in this thesis.

Feature ranking was investigated to inspect whether the linear SVM's feature-weights influences the features' significance. An SVM's predictor is briefly described as:

$$f(\boldsymbol{x}) = 0.5 \left[\operatorname{sgn}\left(\boldsymbol{w}^T \phi\left(\boldsymbol{x}\right) + \boldsymbol{b}\right) + 1\right]$$

Where $\boldsymbol{w}$ and $\boldsymbol{b}$ are the respective weights and biases for features, $\boldsymbol{x}$. The function ϕ maps the training data into a higher dimensional space and will not be discussed in this thesis [58]. The linear and non-linear feature sets' weights, $\boldsymbol{w}$, is depicted in Fig. 5.20 and Fig. 5.21. Consequently, the normalised compactness is an influential feature as it has the largest weight. However, it is noted that the number of pixels has a small weight in both cases, although, upon removal degrades the accuracy. For the remainder of this thesis, the non-linear feature set is used.

Consequently, this feature-set does not contain excess information to poorly train a classifier. Feature weights do not provide information regarding the relationship between features [58], however, their coefficients correlate with their impact. Inspecting Figs. 5.20 to 5.21 show that the linear feature set mainly discriminates vessels over non-vessels. The non-linear feature set has large weights for both classes and is less dominated by a single class.

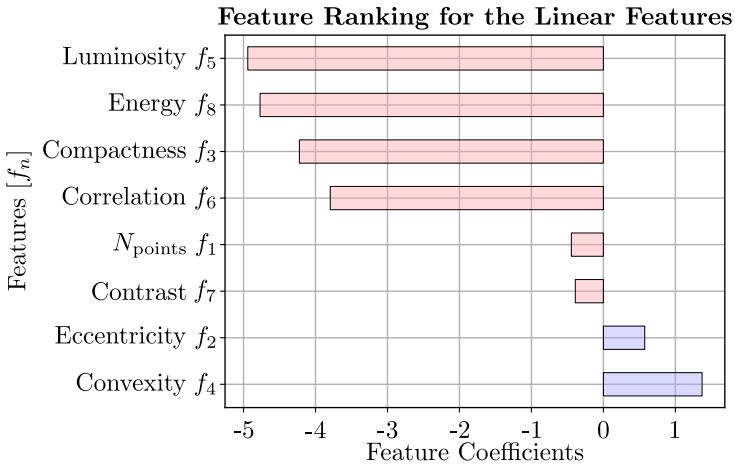

Figure 5.20: SVM linear feature weights.

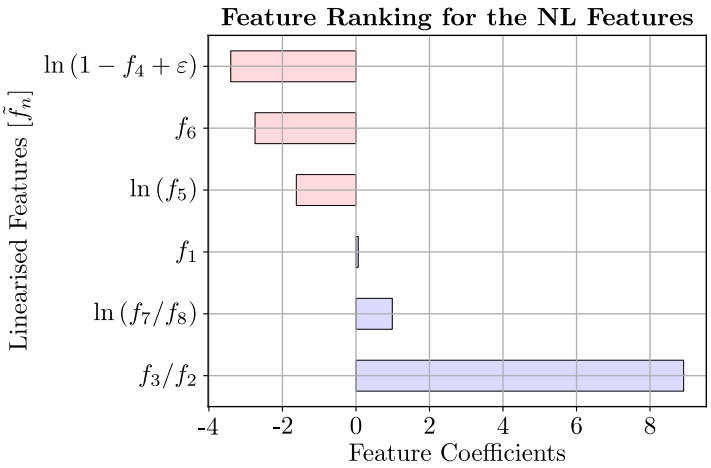

Figure 5.21: SVM non-linear feature weights.

5.4 Validation

This section will elaborate on the vessel-detection algorithm's effectiveness when introduced to different scenarios. Since the algorithm was handcrafted for the off-colour image-composite of Singapore it has to be tested on unseen data. The algorithm was evaluated on the dataset described in chapter 3 that contains five different image sensors with all having different GSDs due to imager-pointing and different hardware.

First, the land masks are investigated to determine their accuracy on difficult images depicted in Fig. 5.22. When introduced to an image with low contrast where land and ocean have similar colour and illuminance, as per Fig. 5.22a, land-masking neglects land areas and masks the ocean region. This is because the surface is not sufficiently homogenous and a more robust method is required than median filtering the image. Moreover, as depicted in Figs. 5.22b to 5.22c, the ocean is bright due to sunglint and the algorithm wrongly identifies the ocean area. Furthermore, upon

inspecting the land-mask applied in Fig. 5.22c, it was found that the land-mask was also applied to the wrong part of the image. This is because the left part of the ocean is illuminated by sunglint and the masking-algorithm inherently assumes that the darker region is land.

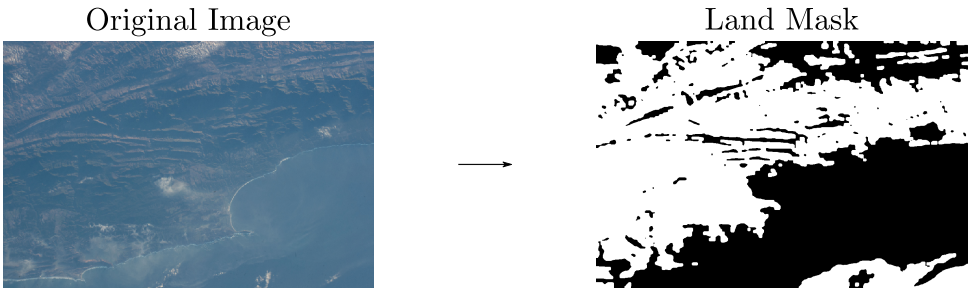

(a) ISS052-E-2625 image validation check.

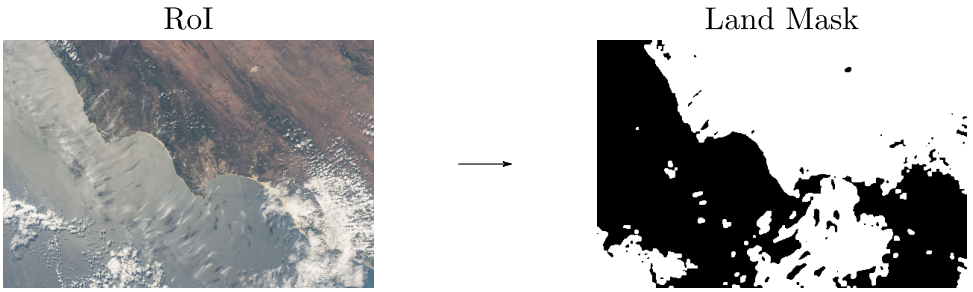

(b) ISS050-E-11672 image validation check.

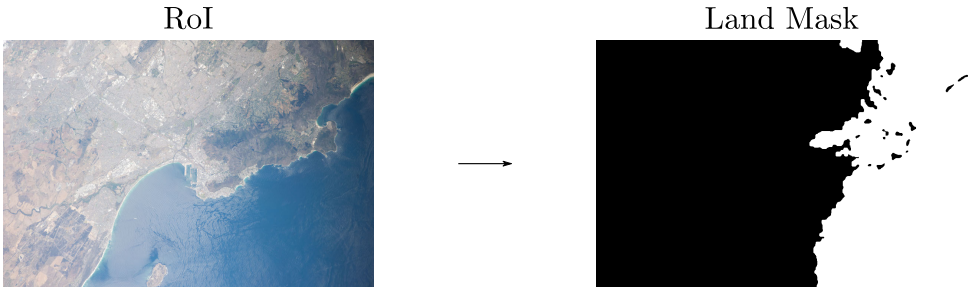

(c) ISS038-E-15450 image validation check.

Figure 5.22: Land mask validation

Secondly, vessel detection accuracy is inspected as depicted in Fig. 5.23. Each image was investigated to determine the causes of misdetections and false alarms. Furthermore, the algorithm underperforms when introduced to lower GSDs. This is because the classifier is not trained on lower resolution textures and the lower contrast images. It was noted that in Fig. 5.23a ports are misclassified and that vessels with a low contrast were overlooked, that can be improved upon in future research.

Fig. 5.23b shows that the land-detection is capable of removing islands with bright clouds imposed onto the image. However, one vessel was missed because of its convex and small shape. Furthermore, false alarms exist on the island borders that could have been avoided, was the land-mask larger. Figs. 5.23c to 5.23d show obviously

missed vessels indicated with white circles because the detection algorithm is not sensitive enough. After inspection, it was found that the vessels were only 10%-40% brighter than their environments and were not detected in the extraction phase. When applied to ISS042-E-24794, shown in Sec. 3.2.4, the land-mask is applied correctly, although, no vessels are detected due to the same reason.

5.5 Conclusion

The image processing is possible when applied to SumbandilaSat images to identify vessels using a hand-fit the algorithm, however, suffered when introduced to foreign environments.

As per Table 1.1, most vessels are small in comparison with cargo vessels or frigates and a satellite will require a small GSD to sense them. Moreover, a smaller GSD implies more detail and a larger variety of textures. This will enable discrimination between small vessels and their complex environment. However, a smaller GSD is coupled with an increased processing time to acquire the same information with more certainty than using a smaller GSD. Furthermore, it will reduce the satellite's swath width and data acquisition will take longer; effectively increasing the temporal resolution. Although, the suggested low inclination of 48° will result in a constellation sensing SA's EEZ more frequently than an SSO and would compensate for its narrower swath width.

The validation phase is used as an aid for the conclusions and will be omitted from the paragraphs to follow. This phase evaluated the algorithm on edge-case images that were chosen based on knowledge regarding the algorithm's functionality. These images contained sunglint, bright clouds, clutter and low contrast vessels. Remote images from the ISS and nSight-1 were used to compare results from the handcrafted algorithm to that of SumbandilaSat's images. Predictably, results from SumbandilaSat outperformed the results acquired from the other images. This section will furthermore elaborate on each of the previous sections' effectiveness in the paragraphs to follow:

Pre-Processing: The land-mask was chosen to be generated from the image by applying an adaptive thresholding technique based on the image's brightness. It assumes only two different areas within an image. This will fail if an image has a third area, for example, sunglint illuminating a part of the ocean or bright clouds forming over the land the ocean. Furthermore, only the RGB channels were used to create a standardised greyscale image. It is recommended to use statistical methods, such as linear discriminant analysis, to combine multispectral bands into an image-composites to best highlight vessel-regions.

As this thesis focuses on the SA EEZ, it is recommended to store a land-mask of SA's coast and use the satellite's position, attitude and GSD to determine which

part of the mask to apply to the image. This will prevent the pre-screening phase from misclassifying land and ocean parts of the image to produce more accurate results. Furthermore, proper land-mask will prevent ports from being misclassified as vessels. Moreover, it is recommended to grow the mask to exclude regions nearby the coastline as it is assumed that illegal fishing from large vessels will not occur near the coast or ports. Penultimately, a second mask is recommended to best remove clouds from an image-composite before attempting to extract RoIs, as clouds are the main reason for false alarms.

Finally, the detector algorithm works well on a homogenous ocean. However, when sunglint is introduced the vessels are not much brighter than their proximity, yet clearly separable. Therefore, an adaptive CFAR algorithm is recommended that uses the sun-angle to scale the power-ratio accordingly. Furthermore, the CA-CFAR response has low power-ratio values surrounding vessels. Consequently, the image-gradient can be incorporated into an adaptive CFAR algorithm.

Vessel Candidate Extraction: Upon inspecting misclassified vessels, it was found that a low contrast vessel may segment to appear like two false alarms after the power-ratio image-composite is thresholded. Therefore, an improved vessel extraction is proposed to rather extract RoIs with a lower threshold. This will introduce more false alarms but can be mitigated by removing the BLObs whose brightest pixel does not meet the power-ratio cut-off of 1.5. This method will not discard low contrast vessels, in addition to retaining more shape information and improving region-growing effectiveness as it is dependent on the BLOb size.

Furthermore, the CCL can be improved to not only discard candidates that exceed pixel-number thresholds but also approximate the candidate's convexity as a function of the number of labels and pixels. It is recommended to implement such a threshold as the algorithm can have long execution times when attempting to connect pixels of a very concave shape.

Vessel Classification: The Singapore image is JPEG-compressed and, therefore, lacks details a 6.25 m GSD image should contain causing the region growing to grow into the background. Therefore, identifying smaller vessels become problematic as the image lacks the required shape and textural information. Moreover, it is recommended to disregard smaller vessels because they have much higher feature variances and causes the linear classifier to misclassify obvious larger vessels. Furthermore, the classifier was overfitted with the Singapore-image which lead to unforeseen errors when introduced to other images containing different elements. Overfitting occurs when a classifier is too closely trained to a specific training set that it will fail to classify RoI in other images.

The selected features are prominent vessel-features, however, no features of the non-vessel class are extracted. It is recommended to extract features from the non-vessel

class to reduce interclass variance, in addition to investigating other textural features. Moreover, if the imager-hardware is known, ideal vessel-images with different illuminations can be used as a ground-truth to compare texture covariance matrices with RoIs as a classification technique.

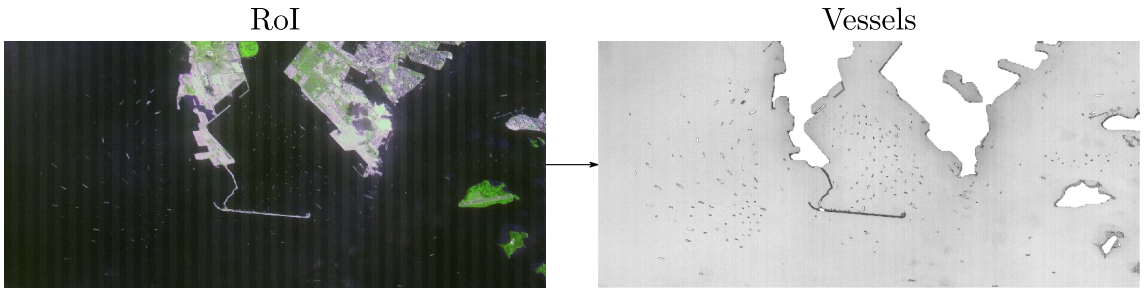

(a) Singapore image validation check.

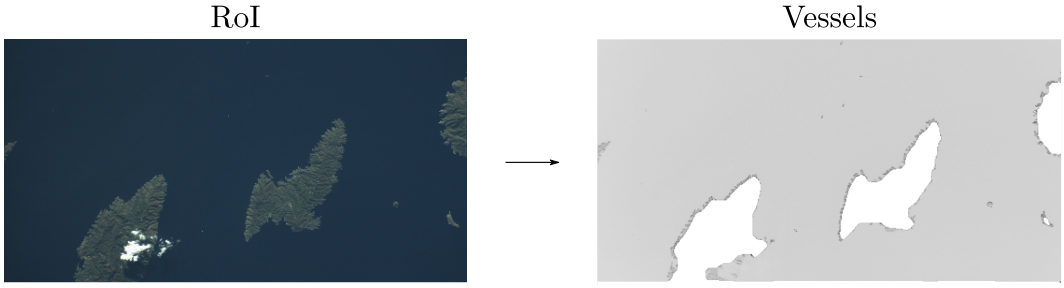

(b) nSight-1 image validation check.

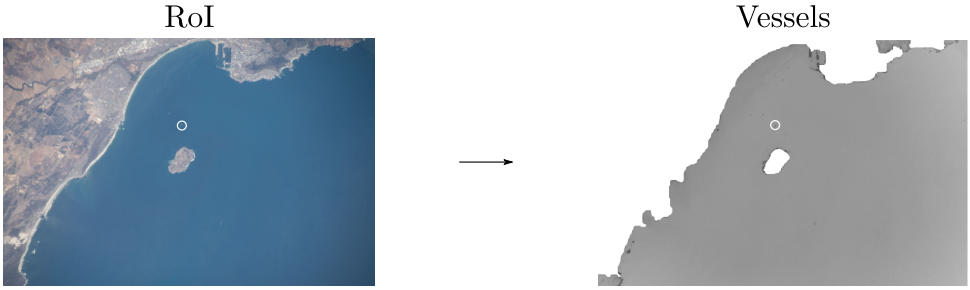

(c) ISS055-E-6893 image validation check.

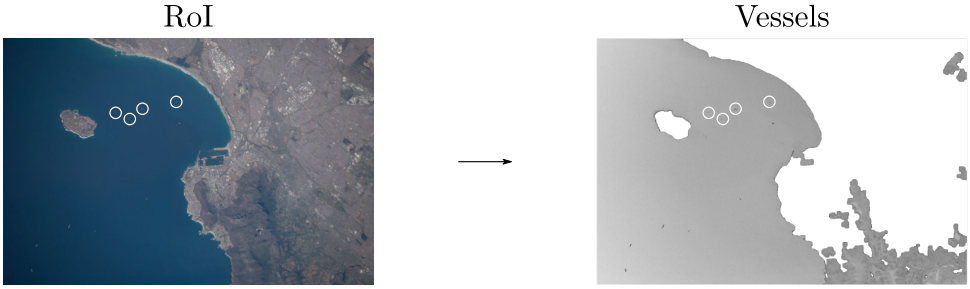

(d) ISS042-E-24792 image validation check.

Figure 5.23: Vessel detection validation.

6. Conclusion

This chapter will discuss the outputs of this thesis and the effectiveness of the used methodologies. This thesis presents a study for detecting illegal vessels in the SA EEZ using a satellite solution. It elaborates on the required satellite constellation required for the most consistent coverage for both an AIS and imager payloads. Furthermore, it inspects methods with which to extract vessel-candidates from remote images using classical computer vision techniques.

This thesis elaborates on whether a 6U CubeSat constellation is capable of detecting the aforementioned vessels. This chapter will discuss the thesis' successful outcomes, shortcomings and possible future work; this thesis has no known disputes.

6.1 Accomplishments

A database was collected through collaboration, sorting through online repositories, and with the courtesy of the SA industry, that contains the necessary information on which to build sensible assumptions for this thesis. The database contains multi-spectral and RGB imaging data with recorded satellite-sensor logs during imaging. Additionally, images in the dataset contain vessels of various shapes and sizes in complex environments with which to validate detection-algorithm robustness. Lastly, it also contains a collection of raw NMEA messages on which to base AIS assumptions, and a *vessel-heat-map* that is used to generate vessel-location coordinates. This dataset can be used to extend the work in this thesis.

A simulation environment was developed that is capable of simulating a constellation of satellites in a string-of-pearls configuration given an epoch, Keplerian orbital parameters, and a set of latitude and longitude coordinates that define a polygon to inspect. It is capable of successfully calculating the total coverage area, time and trends given the constellation's look-angle. The results were compared with STK, which is regarded as a ground truth as it is commercially available simulation software widely used by the space industry, with the differences documented and deemed negligible. Furthermore, numerical adaptations were implemented that resulted in less accurate coverage to reduce computation time at the cost of a negligible accuracy of less than 5%. Lastly, the satellite's swath width and look-angle was determined using commercially available hardware and is deemed to be realistic.

The AIS message reception was investigated to determine the effects that the number of vessels in the satellite's FoV have on its reception capabilities. The number of vessels was sampled from a realistic vessel distribution rather than uniformly sampling the locations, as this will result in more SOTDMA-regions and will produce

inaccurate results. Thereafter, the communication link was investigated to determine the effect that the satellite's antenna choice has on the message reception given the percentage chance for bits to be corrupted during a weak transmission. This is based on a commercially available AIS receiver that can be included onboard the satellite. It was found that 85% of the detected vessels lie between the elevation angles 2.5° and 30°. This is an optimistic result, as it did not account for vessel-tilting due to large deep-sea waves. Consequently, it is recommended for a satellite to have an antenna configuration with a larger gain on the radio horizon to increase message-reception capabilities. These vessels are seen for the shortest amount of time and their messages demand priority over vessels that are seen long enough to intercept at least two messages. This assumed that the satellite will mainly be nadir-looking when searching for vessel signals and will require more power when communicating with a ground station, as its boresight gain will be reduced.

Given the hardware and antenna configuration suggested for this thesis, the satellite feasibility is documented in appendix B. The preliminary mission analysis indicates that the mission is feasible for a 6U CubeSat constellation, however, the satellites might require additional data-storage.

Finally, onboard image processing techniques are investigated. This thesis breaks the methodology down into a three-step process. Firstly, the image is to preprocessed to remove large objects and generate a saliency map to easily identify RoIs. Thereafter, the RoI is extracted and refined with the obvious false alarms being removed. Finally, eight features are extracted from each RoI with which to discriminate the vessels from non-vessel objects. However, precise classification is difficult as hand-selected features cannot be adapted to varying satellite imaging illumination conditions introduced by a 48° inclination orbit. Furthermore, the vessel-features were manipulated using non-linear operations to reduce interclass variance so that a linear SVM can more easily separate the classes. Thereafter, a dataset was generated with which to train an SVM that encompassed a labelling process, that was done best to the author's ability. The entire process worked with a 71% accuracy.

6.2 Shortcomings

This section will elaborate on the chosen methodologies and their effectiveness. The results are evaluated and alternative approaches are considered and discussed.

The collective dataset contains realistic data that are not labelled. This can introduce potential errors as the labelling has to be done manually and the author is prone to misclassify regions of an image. Furthermore, free labelled remote images are not easily acquired. This could have been avoided had the author collaborated with the local authorities, in addition to having a ground truth number for the number of legal vessels in the SA EEZ. Furthermore, the dataset allows for assumptions on which to base augmenting images for better test-data. This will allow mock images to be generated with a specific number of vessels with known locations, as well as a known percentage of cloud coverage. Using this, the image processing algorithms will have better benchmarks and different extraction techniques could have been compared.

The simulation engine was adapted to have variable time-steps that restrict the extraction of accurate eclipse times. The SGP-4 model returns a boolean-flag at each time-step that indicates whether the satellite is in eclipse, however, if the time steps are too large, the eclipse times will become too inaccurate for analysis. Furthermore, the position of the Sun is also known and can be used to calculate the Sun-vector towards the satellite which can be used in image processing to compensate for sunglint in images. Lastly, the FoV was calculated as the satellite's maximum look-angle for imaging. A more accurate EC representation can be achieved by using the satellite pointing discussed in appendix A to point the satellite, with a specific slew-rate, towards locations in the EEZ. Additionally, a country, in the northern hemisphere, with a similar longitude than SA can be added to the simulations. This will allow the satellite constellation to sense a different region when SA is in a DG. Lastly, the satellites should prioritise regions within the EEZ based on the MPA and where illegal fishing is more likely to occur.

The link budget analysis assumed for the ocean to remain perfectly still. This will bias results and it is recommended to introduce an ocean model to introduce vessel-tilt. Furthermore, this can be used to generate DEM to restrict communication, should a wave be in the way.

Finally, regarding the image processing, it is difficult to handcraft a single algorithm to work for different illumination-conditions. Additionally, the images' brightness and contrast could be adapted to emulate different hours of the day. This would enable the measuring of an image's detection accuracy given different hours in a day. This can be used to determine what hour the images will be too dark to process, rather than the winter solstice. Furthermore, it is recommended to design an algorithm on simpler images with no false alarms and introduce them at a time

to build a case for each false alarm into the software. Regarding the land separation, it is recommended to use an accurate land-mask of SA to overlay onto the images as the satellite's position is known within 1 km. However, this will require coast-line detection algorithms but will reduce land-remnant false alarms.

Lastly, the manner in which the different wavelength channels are mixed to create an image composite is based on regular greyscale images. It is recommended to use statistical methods, such as latent Dirichlet allocation, to find the best channel-combination to separate RoI containing vessels from their environments. Furthermore, it is recommended to separate the small vessels from the large vessels, as the smaller vessels hinder the SVM's classification and cause obvious large vessels to be misclassified. Additionally, the false alarm set mainly containing clouds, land-remnants, and clutter should also be separated into different classes, as each subclass exhibits strong trends when inspecting the features listed in appendix C.

6.3 Future Work

This section will elaborate on the thesis' findings and how it can be furthered in research. This section will list possible future work in descending order of importance, as per the author's discretion:

1. **Improve Satellite Pointing Accuracy:** This thesis shows that a pointing error of approximately 1 km may be present in CubeSats if the satellite is not in eclipse. This is based on how accurate a satellite's sensor measurements are to feed into the attitude estimators. It is recommended to extract vessel locations from image-data to match their positions with their estimated positions acquired from interpolating the AIS-data. The point clouds can be compared by using methods such as *iterative-closest-point* algorithms. Furthermore, should a large enough constellation be used where three satellites have coverage of the SA EEZ at any time, vessel locations can be triangulated from their signals as per [59]. This will allow for images to be georeferenced before they are downloaded and improve remote sensing capabilities.

2. **Improve simulation software:** Improvements can be made by adding the AIS-simulation to the coverage simulation. This will allow for a testing-environment with which to build vessel-location interpolating algorithms as the satellite orbits over the EEZ. Furthermore, the satellite should be pointed towards dense vessel areas. The entire AIS dataset can be used to augment a one-day dataset that can be used as ground truth. This can be achieved by only extracting the most complete vessel positions and manually interpolating it.

3. **Hardware Implementation:** Once satisfactory image processing results are acquired, it should be implemented onboard a microcontroller or FPGA to measure its computation time and power usage. An FPGA is recommended

as remote sensed images' pixels lie in the range of millions of pixels and due to hardware resource limitations, large remote sensing images must be split into small slices. This can be used to determine whether a satellite will have enough time to process all the data before it revisits the EEZ. Additionally, if an FPGA is used, the data can be fed to the algorithms in line-scan operation to further reduce computation time. Lastly, additional machine learning techniques are to be investigated, such as convolutional neural networks.

4. **Conduct Research on a Broader EM Spectrum:** It is recommended to investigate thermal infrared images, in addition to night-time images of the EEZ, and their ability to detect vessels during night-time. Notably, the microwave wavelength band is good for clutter rejection, as depicted in Fig. 3.5h, and should be investigated. Should it be possible, the DG become irrelevant and the suggested orbit is ideal for surveying SA's EEZ. Lastly, when CubeSats have hyperspectral imagers; hyperspectral-data containing vessels should be inspected to best combine their channels to generate image composites to best detect vessels.

5. **Inspect Inter-satellite Communication:** If satellites can share information, they can better focus on areas not yet surveyed in the EEZ or rescan areas that had cloud coverage and produced many false alarms. Furthermore, the vessel locations detected by individual satellites can be shared with the constellation to best analyse their behavioural patterns. If collaborating with local authorities, oil-rigs and water buoys can be equipped to detect AIS messages and relay the positional-data to the satellites. Lastly, the satellites crossed-monopole antennas could be rotated to change the radiation pattern to be more directional when surveying dense vessel areas.

6. **Vessel Behavioural Analysis:** Penultimately, after AIS data is acquired from the satellites, vessels that switched off their beacons that are spotted again can be investigated to best determine their most probable routes and can be used to inspect areas within the coast where these vessels might have disappeared. This should include the detection of falsified MMSI numbers. Furthermore, vessels following non-conventional routes or perform curious manoeuvrers can be investigated with satellite imagery. Lastly, vessels of interest can be identified, such as foreign fishing or refrigerated cargo vessels on the border of the EEZ.

7. **In-depth Mission Design:** Finally, an in-depth satellite mission design should be conducted to determine the full mission feasibility. This will include computer models of the satellite design for platform stability and inertia testing, hardware testing and complete mass, link, power, and thermal budgets.

Bibliography

[1] (2015). Fisheries, South African Government, [Online]. Available: https://www.gov.za/about-sa/fisheries (visited on 2018) (cit. on pp. 1, 3).

[2] J. Baker. (2018). Transparent transshipping: detecting illegal fishing with satellite data, Ship Technology, [Online]. Available: https://www.ship-technology.com/features/global-fishing-watch (visited on 2019) (cit. on p. 1).

[3] M. Carlowicz. (2013). Something Fishy in the Atlantic Night. P. Przyborski, Ed., Nasa Earth Observatory, [Online]. Available: https://earthobservatory.nasa.gov/features/Malvinas (visited on 2019) (cit. on p. 1).

[4] Bengis and Others v Government of South Africa and Others; In re: Bengis and Others v Government of South Africa and Others (16884/2013, 2199/2014) [2016] ZAWCHC 14; [2016] 2 All SA 459 (WCC) (24 February 2016) (cit. on p. 1).

[5] S. J. Frantzman. (2018). Avoiding Detection: The Team Tracking Iran's Attempt to Cloak its Oil Exports, The Jerusalem Post, [Online]. Available: https://www.jpost.com/Middle-East/Avoiding-detection-The-team-tracking-Irans-attempt-to-cloak-its-oil-exports-570236 (visited on 2019) (cit. on p. 1).

[6] S. Kings. (Apr. 2016). SA All at Sea Over Illegal Fishing, Mail & Guardian, [Online]. Available: http://www.sun.ac.za/english/faculty/milscience/sigla/Documents/05%20May%202008%20SA%20all%20at%20sea%20over%20illegal%20fishing.pdf (visited on 2019) (cit. on p. 2).

[7] (2019). Fisheries protection vessels, [Online]. Available: https://www.daff.gov.za/Branches/Fisheries-Management/Monitoring-Control-and-Surveillance/FISHPVESSELS (visited on 2019) (cit. on pp. 2, 7).

[8] (2019). Patrol forces, [Online]. Available: http://www.navy.mil.za/equipment/patrol.htm (visited on 2019) (cit. on p. 2).

[9] D. Shipyards. (Feb. 2018). Cape Town (DSCT) Receives Project Biro Order from Armscor, [Online]. Available: https://www.damen.com/en/news/2018/02/damen_shipyards_cape_town_dsct_receives_project_biro_order_from_armscor (visited on 2019) (cit. on p. 2).

[10] R. Campbell. (2019). Building of new ships for south african navy has started, [Online]. Available: https://www.engineeringnews.co.za/article/the-building-of-the-new-ships-for-south-african-navy-has-started-2019-03-08 (visited on 2019) (cit. on p. 2).

[11] S. Kings. (2016). SA at Sea over Illegal Fishing in its Waters, Mail & Guardian, [Online]. Available: https://mg.co.za/article/2016-05-19-00-sa-at-sea-over-illegal-fishing-in-its-waters (visited on 2019) (cit. on p. 2).

[12] L. Boonzaier, S. Harper, D. Zeller, and D. Pauly, "Fisheries Centre Research Reports 20(5), A Brief History of Fishing in the Prince Edward Islands, South Africa, 1950-2010," Fisheries Centre, University of British Columbia, 2012, pp. 95–101. DOI: ISSN1198-6727. [Online]. Available: http://www.seaaroundus.org/doc/publications/chapters/2012/Boonzaier-et-al-Prince-Edward-Is.pdf (visited on 2019) (cit. on p. 3).

[13] (2019). EEZ Tools and Data, Food and Agriculture Organization of the United Nations FishStat Database, [Online]. Available: http://www.seaaroundus.org/data/#/eez (visited on 2019) (cit. on p. 4).

[14] J. Carson-Jackson, "Satellite AIS – Developing Technology or Existing Capability?" *Journal of Navigation*, vol. 65, no. 2, pp. 303–321, 2012, ISSN: 0373-4633. DOI: 10.1017/s037346331100066x (cit. on p. 4).

[15] L. Engelbrecht. (2011). SA Looking to Monitor EEZ, Defence Web, [Online]. Available: https://www.defenceweb.co.za/sea/sea-sea/sa-looking-to-monitor-eez/ (visited on 2019) (cit. on p. 4).

[16] M. A. Cervera and A. Ginesi, "On the performance analysis of a satellite-based AIS system," in *2008 10th International Workshop on Signal Processing for Space Communications*, IEEE, 2008, pp. 1–8, ISBN: 978-1-4244-2572-3. DOI: 10.1109/SPSC.2008.4686715. [Online]. Available: http://ieeexplore.ieee.org/document/4686715/ (cit. on pp. 7, 11, 12, 59, 60, 69, 71).

[17] M. Schmidt. (2017). Lots more fish to fry if SA's exlusive econimic zone is extended, Business Live, [Online]. Available: https://www.businesslive.co.za/fm/features/2017-06-01-lots-more-fish-to-fry-if-sas-exclusive-economic-zone-is-extended/ (visited on 2019) (cit. on p. 7).

[18] International Telecommunication Union, *Technical Characteristics for a Universal Shipborne Automatic Identification System using Time Division Multiple Access in the VHF Maritime Mobile Band, Recommendation ITU-R M.1371*, Radiocommunication Sector of ITU, 1998. [Online]. Available: https://www.itu.int/dms_pubrec/itu-r/rec/m/R-REC-M.1371-0-199811-S!!PDF-E.pdf (visited on 2019) (cit. on pp. 8, 9, 10).

[19] C. Iphar, A. Napoli, and C. Ray, *Detection of false AIS messages for the improvement of maritime situational awareness*, 2015. DOI: 10.23919/OCEANS.2015.7401841 (cit. on p. 9).

[20] International Telecommunication Union, *Report ITU-R M.2123, Long Range Detection of AIS Messages Under Various Tropospheric Propagation Conditions*, M Series, Radiocommunication Sector of ITU, 2007. [Online]. Available: https://www.itu.int/dms_pub/itu-r/opb/rep/R-REP-M.2123-2007-PDF-E.pdf (visited on 2019) (cit. on pp. 9, 69, 70).

[21] ——, *Report ITU-R M.2169, Improved satellite detection of ais*, Mobile, radiodetermination, amateur and related satellite services, M Series, Radiocommunication Sector of ITU, 2009. [Online]. Available: https://www.itu.int/dms_pub/itu-r/opb/rep/R-REP-M.2169-2009-PDF-E.pdf (visited on 2019) (cit. on pp. 11, 69).

[22] "DVB-S2X physical layer performance results over realistic channel models," *International Journal of Satellite Communications and Networking*, vol. 28, no. 5-6, pp. 291–315, 2015, ISSN: 15420973. [Online]. Available: http://onlinelibrary.wiley.com/doi/10.1002/sat.964/abstract (cit. on p. 12).

[23] K. Reiten, R. Schlanbusch, R. Kristiansen, F. Vedal, P. J. Nicklasson, and P. C. Berntsen, "Link and doppler analysis for space-based AIS reception," *Proceedings of the 3rd International Conference on Recent Advances in Space Technologies, RAST 2007*, no. January, pp. 556–561, 2007. DOI: 10.1109/RAST.2007.4284055 (cit. on p. 12).

[24] NASA, "State of the art, Small spacecraft technology," 2018. [Online]. Available: https://sst-soa.arc.nasa.gov/ (visited on 2019) (cit. on pp. 12, B-2, B-3, B-6, B-7).

[25] eoPoral. (2018). ZACube-2 (South African CubeSat-2), eoPortal Directory, [Online]. Available: https://directory.eoportal.org/web/eoportal/satellite-missions/v-w-x-y-z/zacube-2#spacecraft (visited on 2019) (cit. on p. 12).

[26] J. Wang, E. Demeulemeester, and D. Qiu, "A pure proactive scheduling algorithm for multiple earth observation satellites under uncertainties of clouds," *Computers and Operations Research*, vol. 74, pp. 1–13, 2016, ISSN: 03050548. DOI: 10.1016/j.cor.2016.04.014. [Online]. Available: http://dx.doi.org/10.1016/j.cor.2016.04.014 (cit. on p. 13).

[27] J. R. Wertz, D. F. Everett, and J. J. Puschell, *Space Mission Engineering: The New SMAD*. Hawthorne, CA: Microcosm Press, 2011, ISBN: ISBN 978-1-881-883-16-6 (cit. on pp. 14, 15, 36, 45).

[28] D. A. Vallado and W. D. Mcclain, *Fundamentals of Astrodynamics and Applications*, First, W. J. Larson, Ed. McGraw Hill, 1997, 950 pp., ISBN: 9780070668348 (cit. on pp. 18, 23).

[29] H. H. Koelle, *Handbook of Astronautical Engineering*, First. McGraw-Hill, 1961, ch. 8, 1863 pp. (cit. on pp. 18, 19).

[30] M. J. Nadoushan and N. Assadian, "Repeat ground track orbit design with desired revisit time and optimal tilt," *Aerospace Science and Technology*, vol. 40, pp. 200–208, 2015, ISSN: 12709638. DOI: 10.1016/j.ast.2014.11.007. [Online]. Available: http://dx.doi.org/10.1016/j.ast.2014.11.007 (cit. on pp. 19, 21).

[31] A. H. Lokman, P. J. Soh, S. N. Azemi, H. Lago, S. K. Podilchak, S. Chalermwisutkul, M. F. Jamlos, A. A. Al-Hadi, P. Akkaraekthalin, and S. Gao, "A Review for Antennas for Picosatellite Applications," *International Journal of Antennas and Propagation*, 2017, ISSN: 1687-5869. DOI: 10.1155/2017/4940656. [Online]. Available: https://doi.org/10.1155/2017/4940656 (visited on 2019) (cit. on pp. 22, 65, 66, B-2, B-4).

[32] D. Selva and D. Krejci, "A survey and assessment of the capabilities of CubeSats for Earth observation," *Acta Astronautica*, vol. 74, pp. 50–68, 2012, 74, ISSN: 00945765. DOI: 10.1016/j.actaastro.2011.12.014. [Online]. Available: http://dx.doi.org/10.1016/j.actaastro.2011.12.014 (visited on 2019) (cit. on pp. 22, B-3, B-5).

[33] Rocket Lab, *Payload user's guide*, version 6.4, ch. 7. Performance Overview, pp. 26–29, 53 pp. [Online]. Available: https://www.rocketlabusa.com/assets/Uploads/Rocket-Lab-Payload-Users-Guide-6.4.pdf (visited on 2019) (cit. on pp. 22, 23).

[34] D. A. Vallado, P. Crawford, R. Hujsak, and T. Kelso, "Revisiting Spacetrack Report #3," version 2, *AIAA Astrodynamics Specialist Conference*, 2006. [Online]. Available: http://celestrak.com/publications/AIAA/2006-6753/AIAA-2006-6753-Rev2.pdf (visited on 2019) (cit. on pp. 22, 23).

[35] F. R. Hoots and R. L. Roehrich, "Spacetrack report, Models for propagation of norad element sets," Spacetrack, 1988, ch. 6, pp. 10–20, 87 pp. [Online]. Available: http://celestrak.com/NORAD/documentation/spacetrk.pdf (visited on 2019) (cit. on p. 23).

[36] I. v. Z. Marais, "On-board Image Quality Assessment for a Satellite," PhD thesis, Stellenbosch University, 2009 (cit. on pp. 24, 87).

[37] U. Kanjir, H. Greidanus, and K. Oštir, "Vessel detection and classification from spaceborne optical images: A literature survey," *Remote Sensing of Environment*, vol. 207, no. December 2017, pp. 1–26, 2018, ISSN: 00344257. DOI: 10.1016/j.rse.2017.12.033 (cit. on pp. 25, 31, 77, 79, 80).

[38] A. Duvenhage. (2018). Ais Decoder, Github, [Online]. Available: https://github.com/aduvenhage/ais-decoder (visited on 2019) (cit. on p. 28).

[39] J. Stevens, J. M. Smith, and R. A. Bianchetti. (2012). Mapping Our Changing World, Department of Geography, The Pennsylvania State University. A. M. Maceachren and D. J. Peuquet, Eds., College of Earth and Mineral Sciences, [Online]. Available: https://www.e-education.psu.edu/geog260/node/1958 (visited on 2019) (cit. on p. 31).

[40] E. S. Agency, *Sentinel-2 Multispectral Instrument*, 2019. [Online]. Available: https://earth.esa.int/web/sentinel/technical-guides/sentinel-2-msi/msi-instrument (visited on 2019) (cit. on p. 32).

[41] News24. (2009). SA satellite finally lifts off, [Online]. Available: https://web.archive.org/web/20090922190753/http://www.news24.com/Content/SciTech/News/1132/b5480c6d12f049289a98e11936bd1522/18-09-2009-08-12/SA_satellite_finally_lifts_off (visited on 2019) (cit. on p. 33).

[42] D. Vallado. (2015). Fundamentals of astrodynamics and applications fourth edition, Celestrak, [Online]. Available: https://celestrak.com/software/vallado-sw.php (visited on 2019) (cit. on p. 37).

[43] Flanders Marine Institute. (2018). Maritime boundaries geodatabase: Maritime boundaries and exclusive economic zones (200nm). version 10, [Online]. Available: https://doi.org/10.14284/312 (visited on 2019) (cit. on pp. 37, 41).

[44] Simera, *Technical Specification Sheet: xScape100*, 2019. [Online]. Available: https://www.simera.com/wp-content/uploads/2018/07/Simera-Sense-xScape100-tech-data-sheet-230718A-1.pdf (visited on 2019) (cit. on p. 43).

[45] D. Vallado and W. McClain, *Fundamentals of Astrodynamics and Applications*, ser. College custom series. McGraw-Hill, 1997, ISBN: 9780070668348. [Online]. Available: https://books.google.co.za/books?id=pGqFPwAACAAJ (cit. on p. 50).

[46] P. Burzigotti, A. Ginesi, and G. Colavolpe, "Advanced receiver design for satellite-based automatic identification system signal detection," *2010 5th Advanced Satellite Multimedia Systems Conference and the 11th Signal Processing for Space Communications Workshop*, 2010, ISSN: 2326-5949. DOI: 10.1109/ASMS-SPSC.2010.5586907. [Online]. Available: https://ieeexplore.ieee.org/stamp/stamp.jsp?tp=&arnumber=5586907 (visited on 2019) (cit. on p. 65).

[47] D. Gadani, V. Rana, S. Bhatnagar, A. Prajapati, and A. Vyas, "Effect of salinity on the dielectric poperties of water," *Indian Journal of Pure & Applied Physics*, pp. 405–410, 2012, ISSN: 0975-1041. [Online]. Available: http://nopr.niscair.res.in/bitstream/123456789/14183/1/IJPAP50(6)405-410.pdf (visited on 2019) (cit. on p. 69).

[48] Satlab, *Polaris 4-Channel AIS Receiver*, version 1, 2017. [Online]. Available: https://www.satlab.com/resources/SLDS-POLARIS-1.0.pdf (visited on 2019) (cit. on pp. 70, 71).

[49] S. O'Neill, *Electronic Warfare and Radar Systems Engineering Handbook*. Naval Air Warfare Center, 2012, ISBN: 9781782665236 (cit. on p. 71).

[50] D. Devi and A. Sharma, "Ber performance of gmsk using matlab," *International Journal of Advanced Research in Computer Engineering & Technology*, vol. 2, no. 4, pp. 1389–1392, 2013, ISSN: 2278-1323 (cit. on p. 71).

[51] Z. Ding, Y. Yu, B. Wang, and L. Zhang, "An approach for visual attention based on biquaternion and its application for ship detection in multispectral imagery," *Neurocomputing*, vol. 76, no. 1, pp. 9 –17, 2012, Seventh International Symposium on Neural Networks (ISNN 2010) Advances in Web Intelligence, ISSN: 0925-2312. DOI: https://doi.org/10.1016/j.neucom.2011.05.027. [Online]. Available: http://www.sciencedirect.com/science/article/pii/S0925231211004590 (cit. on p. 78).

[52] Y. Yu, H. Ai, X. He, S. Yu, X. Zhong, and M. Lu, *Ship Detection in Optical Satellite Images Using Haar-like Features and Periphery-Cropped Neural Networks*, 2018. DOI: 10.1109/ACCESS.2018.2881479 (cit. on pp. 79, 94).

[53] S. Qi, J. Ma, J. Lin, Y. Li, and J. Tian, "Unsupervised Ship Detection Based on Saliency and S-HOG Descriptor From Optical Satellite Images," *IEEE Geoscience and Remote Sensing Letters*, vol. 12, no. 7, pp. 1451–1455, 2015, ISSN: 1545598X. DOI: 10.1109/LGRS.2015.2408355 (cit. on pp. 80, 81).

[54] C. P. Schwegmann, "Advanced ship detection methods in synthetic aperture radar imagery," PhD, University of Pretoria, 2017 (cit. on p. 81).

[55] C. Z. C. Zhu, H. Z. H. Zhou, R. W. R. Wang, and J. G. J. Guo, "A Novel Hierarchical Method of Ship Detection from Spaceborne Optical Image Based on Shape and Texture Features," *IEEE Transactions on Geoscience and Remote Sensing*, vol. 48, no. 9, pp. 3446–3456, 2010, ISSN: 0196-2892. DOI: 10.1109/TGRS.2010.2046330 (cit. on pp. 81, 86, 91).

[56] N. Bannister and D. Neyland, "Maritime domain awareness with commercially accessible electro-optical sensors in space," *International Journal of Remote Sensing*, vol. 36, no. 1, pp. 211–243, 2015. DOI: 10.1080/01431161.2014.990647. eprint: https://doi.org/10.1080/01431161.2014.990647. [Online]. Available: https://doi.org/10.1080/01431161.2014.990647 (cit. on p. 91).

[57] R. M. Haralick, K Shanmugam, and I. Dinstein, "Textural Features for Image Classification," *IEEE Transactions on Systems, Man, and Cybernetics*, pp. 610–621, 1973, ISSN: 2168-2909. DOI: 10.1109/TSMC.1973.4309314. [Online]. Available: https://ieeexplore.ieee.org/stamp/stamp.jsp?tp=&arnumber=4309314 (visited on 2019) (cit. on pp. 92, 93).

[58] Y.-W. Chang and C.-J. Lin, "Feature Ranking using a Linear SVM," in *Causation and Prediction Challenge*, 2008, pp. 53–64 (cit. on p. 98).

[59] D. Mosher. (2018). SpaceX is About to Rocket a Fleet of Satellites into Space that will hunt Smugglers, Pirates, and other Dark Ships, Business Insider, [Online]. Available: `https://www.businessinsider.com/spacex-to-launch-70-satellites-radio-tracking-2018-11?IR=T` (visited on 2019) (cit. on p. 108).

[60] "Satellite orientation and position for geometric correction of scanner imagery.," *Photogrammetric Engineering & Remote Sensing*, vol. 52, no. 4, pp. 491–499, 1986 (cit. on p. A-3).

[61] CubeSpace. (2019). Star tracker, Three reaction wheel controlled ADCS for 3-axis-pointing, [Online]. Available: `https://cubespace.co.za` (visited on 2019) (cit. on p. B-1).

[62] ——, (2016). Cubeadcs 3-axis, Three reaction wheel controlled ADCS for 3-axis-pointing. version 1.0, [Online]. Available: `https://www.cubesatshop.com/wp-content/uploads/2016/06/CubeADCS_3Axis_Specsheet_V1.0.jpg` (visited on 2019) (cit. on p. B-1).

[63] J. Bouwmeester and J. Guo, "Survey of worldwide pico- and nanosatellite missions, distributions and subsystem technology," *Elsevier*, 2010 (cit. on pp. B-1, B-2).

[64] EnduroSat, *S-band transmitter datasheet*, version 1.0, 2019, p. 6, 12 pp. [Online]. Available: `https://www.endurosat.com/modules-datasheets/S-Band_Tx_Datasheet_Rev_01.pdf` (visited on 2019) (cit. on p. B-2).

[65] ——, *X-band transmitter datasheet*, version 1.2, 2019, p. 6, 12 pp. [Online]. Available: `https://www.endurosat.com/modules-datasheets/X_Band_Datasheet_Rev_1.2.pdf` (visited on 2019) (cit. on p. B-2).

[66] E. Coleshill, J. Cain, F. Newland, and I. D'Souza, "NTS-A nanosatellite space trial," *Acta Astronautica*, vol. 66, no. 9-10, pp. 1475–1480, 2010, ISSN: 00945765. DOI: `10.1016/j.actaastro.2009.11.007`. [Online]. Available: `http://dx.doi.org/10.1016/j.actaastro.2009.11.007` (cit. on p. B-3).

[67] I. Vertat and A. Vobornik, "Efficient and Reliable Solar Panels for Small CubeSat Picosatellites," *Hindawi*, 2014 (cit. on p. B-4).

[68] P. Williams, H. Cramp, and K. Curtis, "Experimental study of the radar cross-section of maritime targets," *IEE Journal on Electronic Circuits and Systems*, vol. 2, 4 1978. [Online]. Available: `https://ieeexplore.ieee.org/stamp/stamp.jsp?tp=&arnumber=4808520` (visited on 2019) (cit. on p. B-4).

[69] A. R. Tummala and A. Dutta, "An Overview of Cube-Satellite Propulsion Technologies and Trends," *MDPI*, 2017. DOI: https://doi.org/10.3390/aerospace4040058. [Online]. Available: https://www.mdpi.com/2226-4310/4/4/58/pdf (visited on 2019) (cit. on p. B-6).

A. SumbandilaSat: Case Study

This chapter will discuss the pointing accuracy of a satellite using real data and whether errors are negligible for determining vessel coordinates. The image, shown in Fig. A.1, was captured on 2nd March, 2010 during a descending pass. The ADCS log contains roll, pitch and yaw (RPY) angles sampled each second. Additionally, SumbandilaSat has a line-scan imager with $\times 4$ forward motion compensation, as depicted in Fig. A.2. The satellite pitches 10° toward the target area and starts imaging. It has a positive pitch constant rate during imaging to effectively reduce the ground-velocity of the satellite and grants the imager more exposure time for the line-scan operation.

Figure A.1: Monochrome image-composite of the full image taken of Singapore by SumbandilaSat.

The ADCS log of the satellite is displayed in Fig. A.3, where it is clear that the satellite is performing a pitch at a near-constant rate for target tracking. However, it is noted that the yaw angle deviates with 1.1° and that the rates are not perfectly constant, but meet the hardware's specification. Furthermore, it is assumed that the pointing location on Earth is the centre of each line in the image parallel to the satellite's pitch axis. This only holds true if the satellite does not point more than 20° as discussed in Sec. 4.2.3. However, this can only be done once the image has been georeferenced.

The georeferencing was accomplished by means of rubbersheeting. This is the process of aligning each of the image's corners to a ground truth, effectively inducing projective transformations onto the image. This transform does not preserve paral-

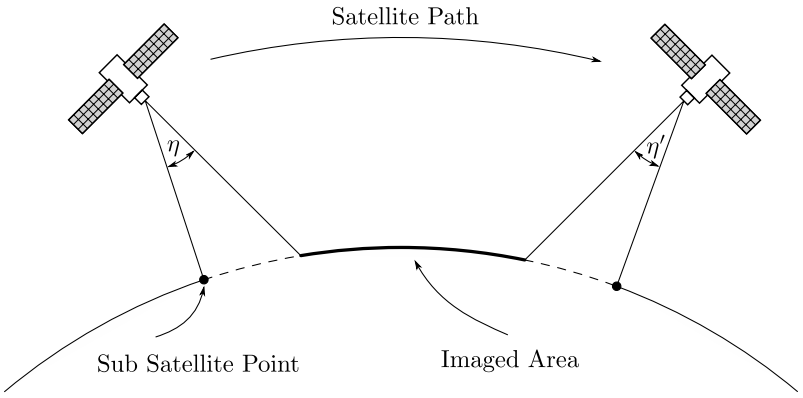

Figure A.2: Depiction of SumbandilaSat forward motion compensation.

lelism, length or angles; therefore, it can be used to apply a perspective distortion to an image. For the case study, Google Earth Pro was used as ground truth and the transformation was applied best to the author's ability. The resultant image is displayed in Fig. A.5a with a white border, the approximate pointing location indicated with a blue line. This is under the assumption that SumbandilaSat's imager is mounted perfectly on the $+Z$-axis.

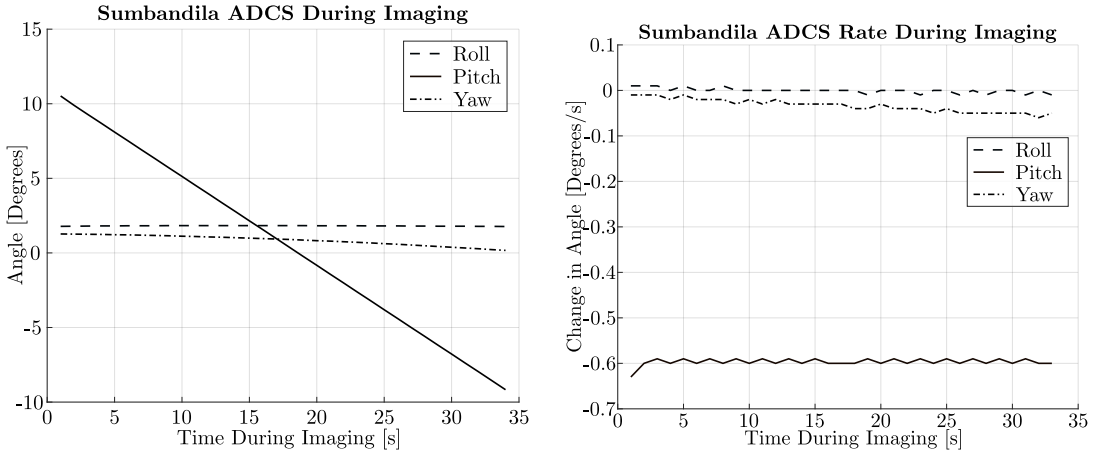

(a) **(b)**

Figure A.3: SumbandilaSat's ADCS during line-scan imaging. **(a)** is SumbandilaSat's RPY angles during imaging. **(b)** is the angular rates during imaging

After each of the corners have been aligned, there were remnants of scaling and rotation distortion present in the image. These distortions are likely due to the dynamics of the system, such as the Earth's rotation and curvature, lens distortion, and a 1.1° change in yaw angle with small deviations in the roll angle, in addition to the pitch rate not being perfectly constant. Ultimately, correcting these effects fall outside the scope of this thesis and can be deemed negligible for vessel detection. Consequently, the assumptions are that SumbandilaSat's yaw angle remains constant during imaging

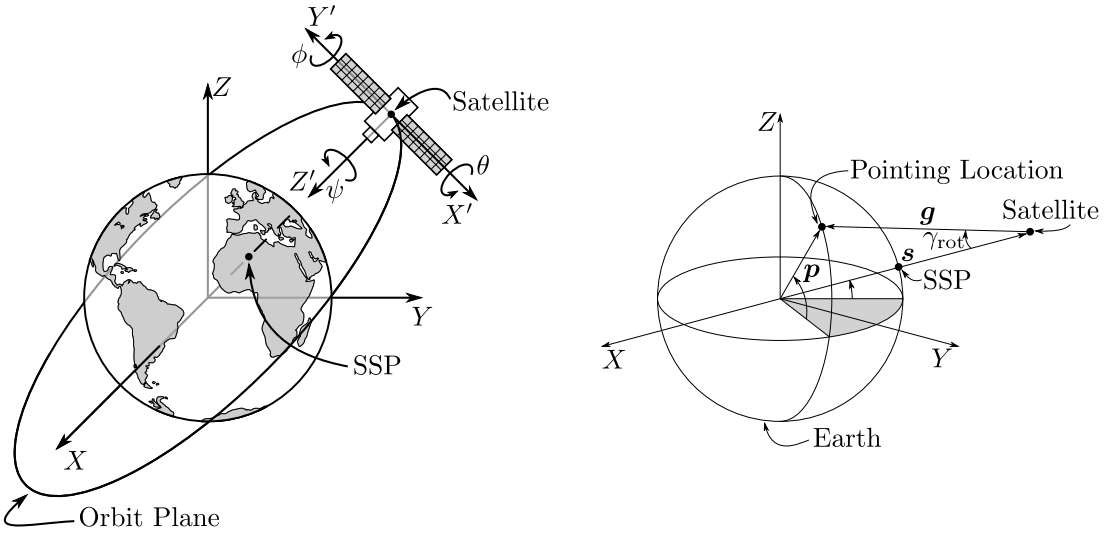

(a) **(b)**

Figure A.4: Description of axes used to transform SumbandilaSat's RPY angles to a location on Earth. **(a)** depicts the Earth Centred Earth Fixed (ECEF) axis with (X, Y, Z) and the Orbit Reference Coordinate (ORC) with (X', Y', Z'). The satellite's Euler rotation angles are shown about each respective axis as a roll (θ), pitch (ϕ), and yaw (ψ). **(b)** depicts the fundamental observation triangle adapted from [60]. It illustrates how to acquire vector $\boldsymbol{p}$ as the sum of vectors $\boldsymbol{s}$ and $\boldsymbol{g}$.

Further investigation was undergone to inspect the satellite's pointing location and how well it coincides with the georeferenced image's centre. The TLE and epoch Unix time of 1 267 495 063 was parsed as parameters for a SGP4 algorithm, described in Sec. 4.1, to determine the satellite's location during imaging. The pointing vector, $\boldsymbol{p}$, describes the corresponding location on Earth where the satellite is expected to point, as described per Fig. A.4. Fig. A.4a illustrates the satellite's RPY angles. The RPY angles are used to calculate vector $\boldsymbol{g}$, as depicted in Fig. A.4b, to calculate $\boldsymbol{p}$. The methodology is described in algorithm A.1 but can be summarised as determining the satellite's look angle, γ_{rot}, as:

$$\gamma_{\text{rot}} = \sqrt{\phi^2 + \theta^2} \tag{A.1}$$

Then, calculate the distance, D, from satellite to its pointing location using Eqs. (2.1) to (2.5). Next, rotate $[0\ 0\ 1]^T$ about the point $\boldsymbol{s}$, with the respective RPY angles, followed by rotating the axes' Z vector to intersect the point $(0, 0, 0)$, which is the centre of Earth. Lastly, the axes' $+X$ axis must be aligned with $+X'$. Finally, evaluate $\boldsymbol{s} + D \cdot \boldsymbol{g}$ to calculate the vector $\boldsymbol{p}$ pointing to the location on Earth.

Lastly, quaternions are used for the axes transformations as only an Euler axis and rotation angle is required. An Euler axis is a unit vector describing the rotation-axis, using the right-hand rule, which is used to describe an orientation with a single rotation. The Euler axis and its corresponding angle is calculated using the

dot- and cross-product rules on two unit-vectors, denoted $\boldsymbol{u}_1$ and $\boldsymbol{u}_2$, described as follows:

$$\gamma = \arccos\left(\frac{\boldsymbol{u}_1 \cdot \boldsymbol{u}_2}{\|\boldsymbol{u}_1\| \cdot \|\boldsymbol{u}_2\|}\right) \tag{A.2}$$

$$\boldsymbol{e} = [e_1 \ e_2 \ e_3]^T = \frac{\boldsymbol{u}_1 \times \boldsymbol{u}_2}{\|\boldsymbol{u}_1 \times \boldsymbol{u}_2\|} \tag{A.3}$$

The Euler angles are converted to a direction cosine matrix (DCM) using a 2-1-3 (pitch, followed by a roll, then a yaw) rotation. For compact notation, the trigonometric functions sine and cosine are written as s and c, respectively, below. The following transformation shows the relationship between the DCM and quaternions, where the RPY angles are indicated with a subscript:

$$\begin{aligned} R_3(\psi) R_1(\theta) R_2(\phi) &= \begin{bmatrix} c_\psi c_\phi + s_\psi s_\theta s_\phi & s_\psi c_\theta & -c_\psi s_\phi + s_\psi s_\theta c_\phi \\ -s_\psi c_\phi + c_\psi s_\theta s_\phi & c_\psi c_\theta & s_\psi s_\phi + c_\psi s_\theta c_\phi \\ c_\theta s_\phi & -s_\theta & c_\theta c_\phi \end{bmatrix} \\ &= \begin{bmatrix} q_1^2 - q_2^2 - q_3^2 + q_4^2 & 2(q_1 q_2 - q_3 q_4) & 2(q_1 q_3 + q_2 q_4) \\ 2(q_1 q_2 + q_3 q_4) & -q_1^2 + q_2^2 - q_3^2 + q_4^2 & 2(q_2 q_3 - q_1 q_4) \\ 2(q_1 q_3 - q_2 q_4) & 2(q_2 q_3 + q_1 q_4) & -q_1^2 - q_2^2 + q_3^2 + q_4^2 \end{bmatrix} \\ &= \mathrm{DCM}(\boldsymbol{e}, \gamma) \end{aligned}$$

With:

$$[q_1 \ q_2 \ q_3 \ q_4]^T = \left[e_1 \sin\frac{\gamma}{2} \ e_2 \sin\frac{\gamma}{2} \ e_3 \sin\frac{\gamma}{2} \ \cos\frac{\gamma}{2}\right]^T$$

The satellite's pointing location result is shown in Fig. A.5b. It is evident that the image is not captured at the desired location. Furthermore, SumbandilaSat has undergone a recorded yaw of 1.27° to 0.17°, however, a roll was undergone that was not recorded in the ADCS log, as the image centre intersects the ground track.

Consequently, the error between the two pointing locations shown in Fig. A.5 is inspected. Fig. A.5a depicts the attempt at rubbersheeting the image. The resultant image is indicated with a white border with its centre highlighted with a blue line, which is SumbandilaSat's expected pointing location. Lastly, the red line is SumbandilaSat's ground track. Fig. A.5b is a visual depiction of the satellite's ADCS log during imaging, where the yellow box is a silhouette of the resultant image. The error is evaluated as the segment length of the great circle that intersects both points. The result, shown in Fig. A.6, shows the error increasing linearly over time. To the author's knowledge, it could be best described with an onboard clock error in addition to an unintentional satellite roll. Fig. A.6a indicates the projected image's centre with a white line and shows the error to the intended pointing location, indicated with a blue line. Fig. A.6b is the pointing error in kilometre as shown in Fig. A.6a.

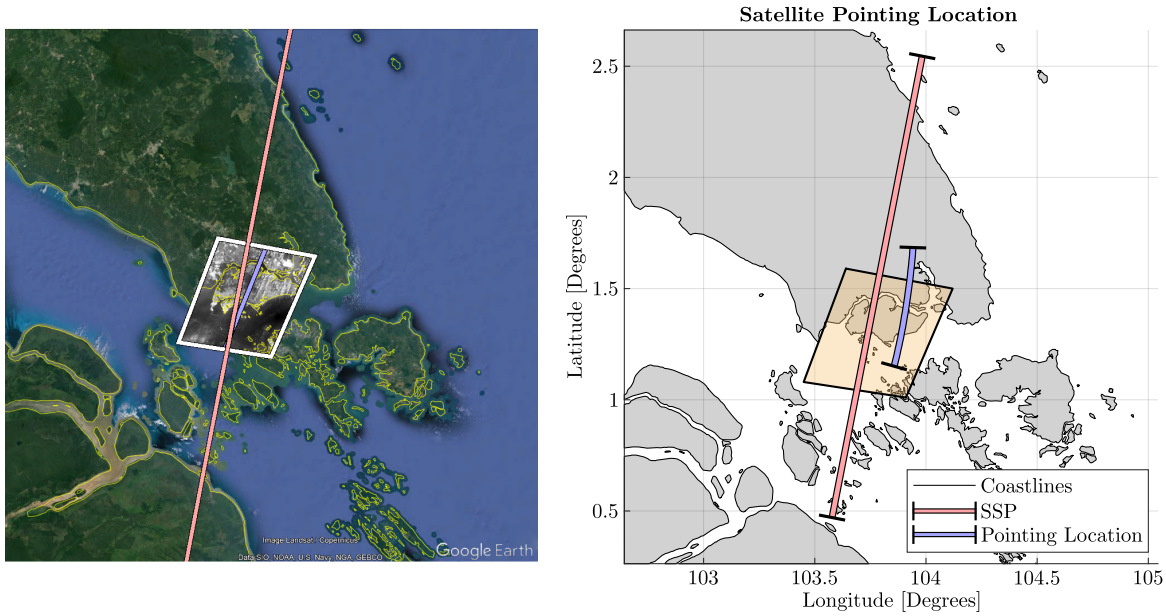

(a) **(b)**

Figure A.5: Comparison between the rubbersheeting resultant image and the ADCS's expected pointing location.

It was discovered that by adjusting the image-epoch time by +2.68 seconds and linearly changing the roll angle from 1.42° to −0.2° over the 33 seconds, a mean error of 1.1 km is obtained as opposed 21.5 km as shown in Fig. A.6. It was noticed that the error obtained in the corrected pointing vector is proportional to the effective look-angle described by Eq. (A.1).

A.1 Conclusion

This case study provided valuable information regarding the georeferencing of vessels within satellite images. Due to pointing errors, the higher the altitude of the satellite, the larger the pointing error will be. Furthermore, the image distortions of satellite imagery were evaluated and it was concluded that image distortions are negligible and lie outside the scope of this thesis.

It is assumed that vessels may lie within 1 km error from where the satellite is pointing. This error will include as the satellite is pointing off-nadir. As such, it will be required to make use of point matching methods to georeference the satellite images onboard the satellite. Furthermore, it is recommended to assess the initial images captured by the satellite to compensate for pointing errors throughout the satellite's lifetime.

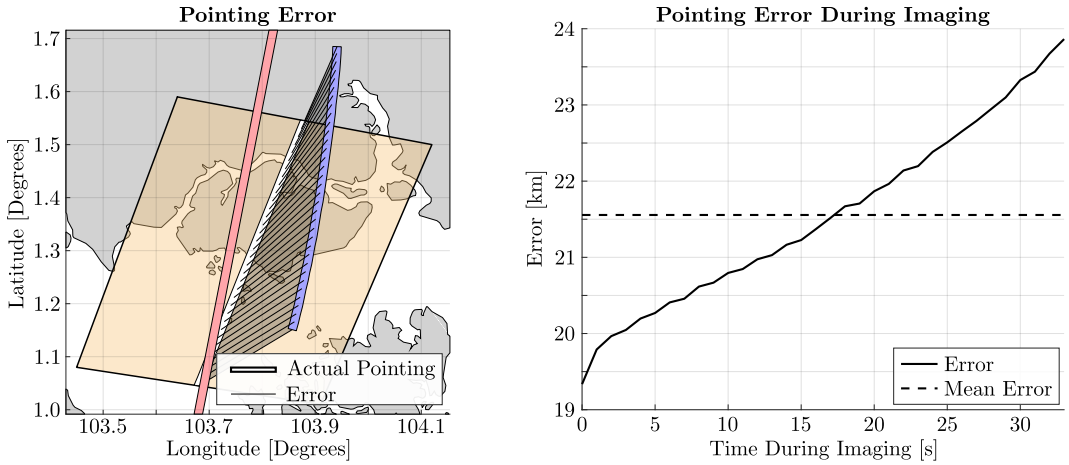

(a) **(b)**

Figure A.6: Error between intended pointing location and actual pointing location.

Algorithm A.1: Calculating SumbandilaSat's pointing location on Earth.

Input: $N_{\text{points}}, \boldsymbol{s}, \phi_{\text{sat}}, \theta_{\text{sat}}, \psi_{\text{sat}}$

Output: $\boldsymbol{p}$

for $n \leftarrow 1$ **to** N_{points} **step** 1 **do**

- $\eta = \sqrt{\theta^2_{\text{sat, n}} + \phi^2_{\text{sat, n}}}$;
- $\boldsymbol{u}_1 = -\text{norm}(\boldsymbol{s}_{\text{n}})$ `// Acquire the +Z vector in ECEF.`
- `// If the look angle is zero, the pointing location is the SSP.`
- **if** $\eta = 0$ **then**
  - $D = \|\boldsymbol{s}_{\text{n}}\| - R_{\oplus}$;
  - $\boldsymbol{g} = D \cdot \boldsymbol{u}_1$;
- **else**
  - $\rho = \arcsin\left(\frac{R_{\oplus}}{R_{\oplus} + \|\boldsymbol{s}_{\text{n}}\|}\right)$;
  - $\varepsilon = \arccos\left(\frac{\sin\eta}{\sin\rho}\right)$;
  - $\lambda = \frac{\pi}{2} - \eta - \varepsilon$;
  - $D = R_{\oplus}\frac{\sin\lambda}{\sin\eta}$;
  - $\boldsymbol{R}_{\text{tot}} = \boldsymbol{R}_3\left(\psi_{\text{sat, n}}\right)\boldsymbol{R}_1\left(\theta_{\text{sat, n}}\right)\boldsymbol{R}_2\left(\phi_{\text{sat, n}}\right)$;
  - $\boldsymbol{g} = \boldsymbol{R}_{\text{tot}} \cdot [0\ 0\ 1]^T$ `// Rotate the +Z axis to pointing location in ORC.`
  - $\boldsymbol{R}_{\text{tot}} = \text{DCM}\left[\text{norm}\left([0\ 0\ 1]^T \times \boldsymbol{u}_1\right), \arccos\left([0\ 0\ 1]^T \cdot \boldsymbol{u}_1\right)\right]$;
  - $\boldsymbol{g} = \boldsymbol{R}_{\text{tot}} \cdot \boldsymbol{g}$ `// Rotate the pointing vector to point towards Earth.`
  - `// Finally, align the x-axes.`
  - $\boldsymbol{X} = \boldsymbol{R}_{\text{tot}} \cdot [0\ 0\ 1]^T$;
  - `// Determine the instanenous orbiting plane in ECEF.`
  - **if** $n = 1$ **then**
    - $\boldsymbol{u}_2 = -\boldsymbol{u}_1$;
    - $\boldsymbol{u}_1 = \text{norm}(\boldsymbol{s}_{\text{n+1}})$;
  - **else**
    - $\boldsymbol{u}_1 = -\boldsymbol{u}_1$;
    - $\boldsymbol{u}_2 = \text{norm}(\boldsymbol{s}_{\text{n-1}})$;
  - `// Acquire SumbandilaSat's +X'.`
  - $\boldsymbol{X'} = \text{norm}\left(\text{DCM}\left[\boldsymbol{u}_1 \times \boldsymbol{u}_2, \frac{\pi}{2}\right] \cdot -\boldsymbol{u}_1\right)$;
  - `// Align the axis of the pointing vector with the +X' vector.`
  - $\boldsymbol{g} = D \cdot \text{DCM}\left(\boldsymbol{u}_1, \arccos\left(\boldsymbol{X'} \cdot \boldsymbol{X}\right)\right) \cdot \boldsymbol{g}$;
- $\boldsymbol{p}_{\text{n}} = \boldsymbol{s}_{\text{n}} + \boldsymbol{g}$;

B. Satellite Mission Feasibility

This chapter will briefly discuss the mission feasibility regarding the assumptions made in chapter 4. It will also elaborate on the storage capabilities for the AIS-data and images, which is further discussed in chapter 5. Furthermore, the satellite's end-of-life analysis lies outside the thesis scope and it is assumed that the satellite can function 5-years in orbit before failing; which will also not be discussed.

B.1 Attitude Determination and Control System

The satellite's attitude determination and control system (ADCS) will impact its ability to geolocate vessels in its images and is discussed in higher detail in appendix A. Its geolocation is the ability to accurately determine the satellite's attitude at the time of measurements and directly impact the quality of the measurements. Therefore, if the satellite is uncertain about its attitude, there will be a pointing error and the satellite will image a location it did not intend to.

The ADCS used for inspection in this thesis is the CubeADCS produced by CubeSpace. The attitude estimation sensors that this system uses has a 3σ accuracy for roll, yaw and pitch of less than 0.1° [61]. Assuming a typical orbit altitude of 500 km, an attitude determination uncertainty of 0.1° for nadir instruments leads to a spatial uncertainty of 1 km [62].

Furthermore, the swath-width of a satellite in this altitude with the Simera Sense HyperScape100 camera is 19.5 km. Therefore, a 1 km pointing is deemed negligible. As expressed in appendix A, a 3 s timing error can result in a pointing error of 20 km which can be corrected.

B.2 Dimensions

The satellite's dimensions have the largest impact on the payload. To elaborate, the aperture of an optical payload determines its diffraction-limited angular resolution and, therefore, limits its ground spatial resolution. This is described by the Rayleigh diffraction criteria for a circular aperture expressed in Eq. (4.3) [63].

$$G \approx \eta \left(\frac{\pi D}{\lambda} \right)^2 \tag{B.1}$$

Therefore, for this thesis, the Simera Sense HyperScape100 is used that fits in a small satellite. A smaller spatial resolution cannot be acquired for its dimensions as it is governed by physics. Similarly, the *diameter* of an antenna dictates its gain; it

affects the signal-to-noise ratio. In particular, the gain for an aperture antenna is expressed in Eq. (B.1), where η is the antenna's efficiency (usually between 0.55 and 0.7), D is its diameter, and λ is the frequency at which the antenna is operating. Consequently, the gain of an antenna scales with its lengths and diameter, with respect to its wavelength. As such, complex antennas operating in VHF and UHF become infeasible for CubeSats. It should be noted that UHF deployable antennas for CubeSats do exist [31].

B.3 Communications

It is assumed that the satellites will only have one ground station located at Stellenbosch University. Therefore, the data-downlink will require a separate frequency and can only transmit stored information.

The main limitation for a CubeSat's data-rates is the available link budget that impacts its size, power-usage, and data-rate [63]. Therefore, it has an influence on the transmitting power, operating frequencies, gain and beam-widths of the antenna topologies [31]. Furthermore, a satellite's telemetry, tracking, and command (TT&C) data is transmitted specifically using the VHF and UHF bands to its ground station[31]. TT&C is used for communication between spacecraft and the ground systems. The subsystems functions are: controlling of the spacecraft by the operator on Earth. Receive the uplink commands, process and send them to other subsystems for execution.

Considering the following two off-the-shelf transmitter-products from EnduroSat: an X- and S-band transceiver. The EnduroSat S- and X-Band transmitters are able to transmit at 32 dBm requiring 7.2 W and 12 W, respectively, and can reach a data-rates up to 5 Msym/s and 30 Msym/s [64], [65]. Additionally, both units can store up to 32 GB internally. Consequently, when the link is strongest, the signal can be sent at a data-rate of 2.4 MBps or 14 MBps for the S-band and X-band transmitters, respectively.

S-band transmitters have a strong flight heritage, whereas X-band transmitters require high gains and are preferred for deep-space communication [24], [31]. The X-band transmitter will consume too much power for a 6U satellite that is both imaging and collecting AIS-data. Therefore, the S-band transmitter is recommended.

A best-case data-rate can be estimated by assuming the following:

- $f = 2.4\,\text{GHz}$,
- $P_t = 7.2\,\text{W}$,
- $G_t = 8\,\text{dBi}$, a high gain transmitting antenna,
- $G_r = \eta\left(\frac{\pi D}{\lambda}\right)^2 = 0.65\left(\frac{2\pi}{0.124}\right)^2 \approxeq 1670\,\text{dBi}$, an S-band dish antenna (recall Eq. (B.1)),

- $L_{\text{tot}} = 4\,\text{dB}$,
- $L_\ell = 154.1\,\text{dB}$,
- $r = 500\,000$, the closest distance for a 500 km altitude satellite,
- $T = 300\,\text{K}$, noise factor of 2,
- $\frac{E_b}{N_0} = 10\,\text{dB}$, QPSK BER of 10^{-5}

Which will result in a data-rate of approximately 20 MBps. This estimation does not include antenna inaccuracies, satellite pointing losses, increased communication distance for when the satellite does not fly over-head. As this is a highly optimistic data-rate, a more conservative downlink of 2.4 MBps is used.

B.4 Onboard Data Handling

The microcontrollers used in CubeSats are power efficient and generally feature ARM processors. Certain architectures support OpenCV which is a powerful machine vision software tool that is useful for imaging applications and is used in chapter 5 [24]. Onboard computers generally have clock speeds of 4 MHz–48 MHz with 16 bit–32 bit architectures [32].

A LEO satellite can download 1.7 GB during a single pass of 12 min at a 2.4 MBps, which is roughly the size of two hyper-spectral images. Furthermore, there will be an average of eight daily passes over Stellenbosch for a low inclination orbit. Therefore, the theoretical maximum data that can be downloaded is 11.2 GB. However, the data-rate can degrade to 2.4 Mbps should the satellite operate in low-power mode, which will result in 180 MB to be downloaded in a day. This could restrict a CubeSats from transmitting high-resolution images or relaying it; as such, onboard processing becomes a viable option.

Assuming that each AIS channel is sampled at twice the Nyquist frequency of 38 400 Hz with a 12 bit depth, equates to 921.6 kbps for both channels. If it is further assumed that AIS signals are received for 50% of the time, the effective data stream bitrate is 460.8 kbps. This translates to approximately 42 MB of SA EEZ AIS-data per typical 90 min orbit. It is shown that 90 s of AIS-data takes three to five days to download over a 32 kbps S-Band connection [66]. Therefore, only prioritised data should be downlinked, such as uncertain areas or requested remotely sensed images of Earth. Lastly, it is assumed that the onboard computer will weigh no more than 0.4 kg and have an average power consumption of 1.5 W.

It is assumed that the satellite can achieve a slew of 30° within 60 s for Sun tracking modes. The effects of gravity gradient, aerodynamic drag, magnetic torquers, reaction wheels, and misaligned thrusters fall outside the scope of this thesis.

For the inter-satellite communication discussed in this thesis, there exists a 60 GHz

V-band antenna to fit the CubeSat chassis resulting in a 15.4 dBi of gain and used for inter-satellite CubeSat communication link [31]. However, this is experimental technology and is deemed future work.

B.5 Power

One 1U CubeSat facet offers an area of 83 cm^2 for solar panels. It is not possible to generate more than 1 W when using low-cost silicon-based solar cells. Therefore, gallium arsenide based multi-junction solar cells are recommended, as they can generate a maximum of 3 W [67]. Two standardised cells per facet are possible and can be wired in series to increase it efficiency at the cost of reliability [67].

$$P = \eta_{\mathrm{n}} S A \cos\varphi \tag{B.2}$$

Eq. (B.2) is a simplified expression to calculate the energy generated by solar cells, P, where η_n is the nominal efficiency, S is the sunlight power density (approximately 1350 $\mathrm{W\,m^{-2}}$), A is the solar-cell area facing the sun, and φ sunlight incidence angle, measure from the solar-cell. The efficiency is inverse proportional to temperature: during temperature extremes of 60 °C, the efficiency will degrade by 10% [67].

The aforementioned power levels are incompatible with active illumination payloads. Consider the received power in the pseudo-radar expression:

$$P_r = \frac{\sigma P_t G_t A_r}{(4\pi R^2)^2}$$

Where P_r is the received power, P_t is the transmitted power, G_t is the antenna's gain, A_r is the receiving antenna's effective aperture:

$$A_r = \frac{G_r \lambda^2}{4\pi}$$

Where λ is the transmitted wavelength and G_r is the antenna gain, which in this case is equal to G_t. Furthermore, σ is the radar cross section, for a coaster-vessel in centimetre wavelengths is in the range of 40 m^2–2000 m^2 [68], and R is the transmission distance. It is assumed that satellite's motion has a negligible effect on the distance. Considering a 500 km altitude satellite with an antenna gain of 32 dB, effective aperture of 11.34 m^2 and operating at a 1 GHz, results in $\frac{P_r}{P_t} \approx 2 \times 10^{-18}$. Consequently, to receive −120 dBm, the payload should transmit in the order of mega watts.

Lastly, the battery size should also be considered and will be briefly discussed. The orbit's worst-case eclipse time is expressed as:

$$T_{\mathrm{E}} = \frac{\rho}{\pi} \times T_N \tag{B.3}$$

Where T_N is calculated using Eq. (2.7) as 94.4 min for the RGT orbit defined in Sec. 4.3.3. Finally, the worst case eclipse time is calculated as 35.8 min. The worst case power usage for the satellite will be 15.4 W:

- 1.5 W - satellite pointing,
- 2.5 W - imager electronics,
- 1.4 W - AIS decoder,
- 7.5 W - S-band downlink,
- 1.5 W - onboard computer, and
- 1.0 W - contingency

This is considerable power usage for a 6U CubeSat. The solar panel energy regeneration required is expressed as:

$$P_{\text{sa}} = \frac{\frac{P_e T_e}{X_e} + \frac{P_d T_d}{X_d}}{T_d}$$

Where subscripts e and d denoted eclipse and daytime and X is the efficiency, which is 0.6 and 0.8 during eclipse and daytime, respective. It's assumed that the imager will be switched off during eclipse and that the satellite will operate in low-power mode, resulting in roughly 5 W less being used. As such, the solar panel power is calculated as 16.94 W. Assuming that half the Sun's irradiance will illuminate the solar panels, roughly 18 solar panels will be required. Therefore, the satellite will require deployable panels.

Lastly, a typical CubeSat components function in the range of 5 V. Therefore, groups of two 3.6 V 1.5 A h Li-Ion cells are assumed to be used with a 7.2 V bus voltage. It is assumed that the transmission efficiency, η_b, between the battery and the load is 0.9 and that the batteries have a depth-of-discharge (DoD) of 50% with an energy density of 80 W h kg^{-1}. The rated capacity required for the eclipse period is calculated as:

$$C = \frac{P_e T_e}{\eta_b \text{DoD}}$$

Which results in a capacity, C, of 10.5 W h required for when the satellite is in eclipse. Furthermore, the rated current is specified as 1.5 A h and the batteries are able to supply 1.46 A h. As such, no cells are required to be placed in parallel. Lastly, the capacity of the batteries is calculated as $1.5 \times 7.2 = 10.8$ W h. Finally, this results in 0.14 kg batteries required for the satellite.

B.6 Propulsion

Literature suggests that CubeSats have propulsion-budgets, denoted ΔV, ranging from 10 m s^{-1}–30 m s^{-1} [32]. ΔV is a cumulative measure of velocity changes that can be induced onto a satellite's dynamics. It is dependent on the propellant's specific impulse, I_{sp}, that is the thrust per unit propellant mass:

$$I_{\text{sp}} = \frac{T}{\dot{m}_{\text{p}} g}$$

Where T is the thrust in N m, $\dot{m}_\mathrm{p}$ is the change in propellant mass, and g is the experienced gravity. This is used to calculate the propulsion system's Delta-v:

$$\Delta v = -gI_\mathrm{sp} \ln\left(\frac{m_\mathrm{s} + m_\mathrm{p}}{m_\mathrm{s}}\right)$$

The specialised orbit discussed in Sec. 4.3.3 requires periodic orbit-adjustments burns must be made to restore the semimajor axis to maintain its orbit. The change in groundtrack shift grows quadratically with the number of revolutions and results in severe decay under strong drag:

$$\alpha_D = -B^* v_s^2$$

Where v_s is the satellite's velocity calculated using the Vis-Viva equation expressed in Eq. (4.5). Recall Eq. (2.13), for a 6 U satellite orbiting at a 500 km altitude, the worst-case B^* is calculated as:

$$B^* = \frac{2.2 \cdot [(0.06\cos 26.4° + 0.03 \sin 26.4°)\cos 16.6° + 0.02 \sin 16.6°]}{2 \times 1.33 \times 6} \times 2.03 \times 10^{-12}$$

Which equates to 1.9588×10^{-14} that is used to calculate the drag as $-3.439 \times 10^{-7}\,\mathrm{m\,s^{-2}}$ per orbit. Finally, the required ΔV required for a five-year mission is:

$$\Delta v_\mathrm{tot} = 2 \times 365 \times 86400 \alpha_D = 54.23\,\mathrm{m\,s^{-1}}$$

Cold gas systems have strong small satellite flight heritage and are robust and usually 2 U in volume [24], [69]. For this thesis, a Butane propulsion system is assumed with a thrust of 0.5 N and I_isp of 80 s. Furthermore, as contingency the ΔV is increased by 10% to $60\,\mathrm{m\,s^{-1}}$. For such a mission the fuel-mass, m_fuel, can be calculated as:

$$m_\mathrm{fuel} = m_\mathrm{sat}\left(1 - e^{-\frac{\Delta v}{gI_\mathrm{isp}}}\right)$$

That equates to 0.587 kg. Lastly, Butane has a liquid density of $530\,\mathrm{kg\,m^{-3}}$ that results in $1.11 \times 10^{-3}\,\mathrm{m^3}$ which is approximately 1U.

B.7 Thermal Control

This subsection will elaborate on the necessary thermal control required for CubeSat missions. Onboard components have a range of allowable temperatures that must be met for optimal functionality. These temperatures must be regulated using thermal management. For this thesis, passive thermal control was chosen.

Passive thermal control is low cost, reliable and has negligible volume and mass [24]. They include multi-layer insulation (MLI), thermal coatings, heat pipes, sunshades, and louvres. Heat is transferred by means of radiation and conduction in space. The thermal radiation environment is manipulated by using materials that have

certain specific radiative properties, commonly referred to as solar absorptivity, α, and IR emissivity, ε. Solar absorptivity is the amount of impinging solar flux that a satellite absorbs, while IR emissivity is the satellite's ability emit its thermal energy into space relative to a perfect Black-body emitter [24].

The typical absorptivity, α_{sp}, and emissivity, ε_{sp}, of GaAs solar panels are assumed to be 0.805 J and 0.825 J, respectively. It is assumed that the satellite's thermal limit is $-30\,^{\circ}\text{C}$–$30\,^{\circ}\text{C}$, which needs to be re-evaluted once all subsystems have been assessed. It is assumed that the satellite's body will be covered with white epoxy paint wit $\alpha_{\text{wp}} = 0.25$ and $\varepsilon_{\text{wp}} = 0.85$. Furthermore, the radiator's material of choice is optical solar reflectors with $\alpha_{\text{r}} = 0.077$ and $\varepsilon_{\text{r}} = 0.79$, respectively. The remainder of the satellite will be covered with MLI with zero absorptivity and emissivity.

B.8 Conclusion

This section shows that the proposed satellite solution is possible on a 6U satellite. No specific budgets are supplied as small compromises can be made should certain budgets exceed absolute maximums. As such, mission costs cannot be calculated and, therefore, the cost for surveillance is subject to change.

Additionally, the power usage and complexity can be reduced by placing the ground station outside the satellite's FoV when flying across SA. It was also shown with a pseudo radar equation that active illumination will not be possible given the power limitations of a CubeSat. Furthermore, it is not possible to survey the entirety of the EEZ and download the images as the satellites can not maintain a strong enough link with a single ground station to achieve this. Ultimately, it is plausible for the constellation to function for 5 years.

C. Image Processing Addendum

This chapter briefly discusses the different identified regions in images and elaborate on how they were acquired and helped shape the algorithms. The first section will discuss the distinct vessel features and when vessels are difficult to distinguish from their environment. Next, non-vessel features will be discussed and how they differ from vessel objects. Lastly, region growing will be discussed to elaborate on when the algorithm fails.

C.1 Vessel Features

Examples of vessels are depicted in Fig. C.1 with their respective features show in Table C.1, where N_p, ε, C_p, and C_v are the number of pixels, shape-eccentricity, compactness, and convexity, respectively. The texture features are excluded as they depend on the shape-features and do not make intuitive sense as the vessels have varying textures. These images are distorted and scaled to fit properly, therefore, their features might not visually correspond with the tabled values.

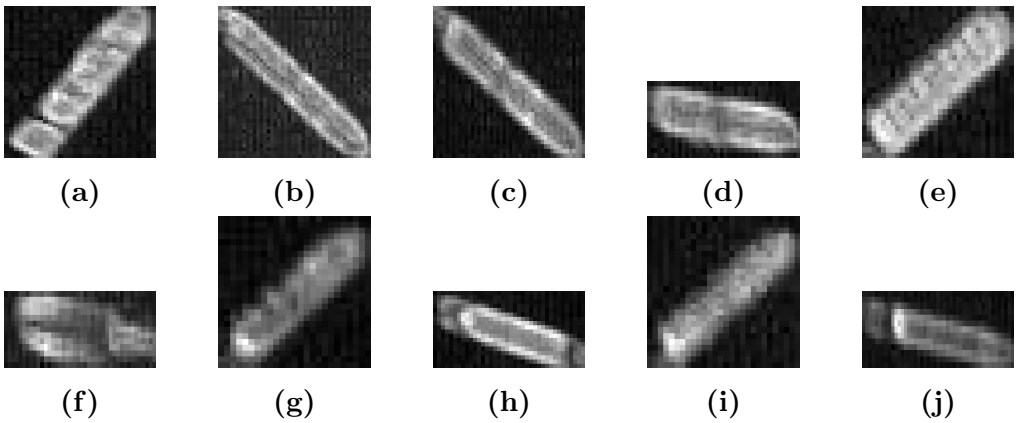

Figure C.1: Examples of valid vessel candidates.

These vessels are considered as large in contrast to the small vessels displayed Fig. C.2. Larger vessels generally contain more than 100 pixels as it assumed that they are at least 200×20 m^2 in size. However, it is difficult to distinguish actual vessel from their wakes as depicted in Fig. C.2(a). Vessels depicted in Fig. C.1(a), (g), (h), (i), and (j) have clear castles, whereas the other vessels have smoother textures. Notably, Fig. C.1(f) is half of a vessel and upon further inspection, it was discovered that its intensity faded and appeared to grow into the background. Vessels, such as this one, are regarded as a hit-or-miss and classifying these vessels falls outside the thesis scope.

Furthermore, a general trend that is observed is that the larger vessels contain more than 300 pixels and are easily identifiable. The vessels show high eccentricity of larger than 1.5 with convexities near one. This indicates long and smooth shapes. Compactness scale with the number of pixels and, therefore, is used as an auxiliary feature to discriminate candidates with interclass variance.

Table C.1: Vessel image description, where N_p, ε, C_p, and C_v are the number of pixels, shape-eccentricity, compactness, and convexity, respectively

Label	N_p	ε	C_p	C_v	**Label**	N_p	ε	C_p	C_v
a	507	4.14	4.12	0.896	f	368	3.79	2.57	0.911
b	498	5.98	4.46	0.938	g	344	2.58	2.24	0.985
c	489	5.50	3.91	0.907	h	332	3.94	2.85	0.917
d	409	4.20	2.53	0.900	i	329	3.03	2.62	0.9627
e	379	3.33	2.73	0.943	j	327	6.05	3.33	0.879

It is noted that small vessels should form a separate class to large vessels as their features differ significantly, as seen in Fig. C.2. Vessel (a) is a speedboat with a large wake, vessel (b) is slightly larger with a wider wake and both vessels (c) and (d) are vessels with small wakes with vessel (d) turning resulting convex shape. However, only the vessel-part was detected in image (d) as there is only 31 pixels listed in Table C.2. These vessels produce many false alarms when attempting to distinguish them from small clouds.

(a) **(b)** **(c)** **(d)**

Figure C.2: Small vessel examples that generate false alarms.

Table C.2: Small vessel image description

Label	N_p	ε	C_p	C_v
a	262	1.73	1.99	0.929
b	116	2.54	2.08	0.943
c	40	1.86	1.56	0.975
d	31	1.64	1.48	0.969

Lastly, the vessel candidates depicted in Fig. C.3 are assumed to be missed by detection algorithms. Image (a) shows a vessel in the top left corner that is obscured by clouds. The region growing will grow from the vessel and into the cloud and will result in misclassification. Therefore, the BLOb exceeds 1500 pixels and will be

rejected. Images (b) and (d) show vessels with poorly illuminated decks that will be suppressed by the detector algorithm with the edges being highlighted and the images will look like small clouds. Lastly, image (c) shows two vessels next to each other that was extracted, therefore, the convexity is below 0.8 and will result in a false alarm.

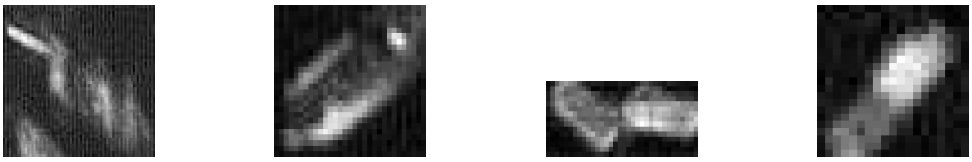

(a) **(b)** **(c)** **(d)**

Figure C.3: Vessel anomaly examples that generate false alarms.

Table C.3: Vessel anomaly image description

Label	N_p	ε	C_p	C_v
a	1563	3.54	3.49	0.876
b	514	1.90	2.19	0.931
c	271	3.24	3.24	0.757
d	232	1.97	2.09	0.943

C.2 Non-Vessel Features

The largest contributors to false alarms are clouds, land-remnants, and clutter. Clouds are depicted in Fig. C.4 and they can only be distinguished from vessels by considering texture. Furthermore, clouds can be separated from large vessels by taking eccentricity into account. However, clouds have very similar features to small vessels and only textural features can be used to discriminate small vessels from clouds. As such, when a SVM is trained to classify both large and small vessels will cause for significant interclass variance as depicted in Fig. 5.19.

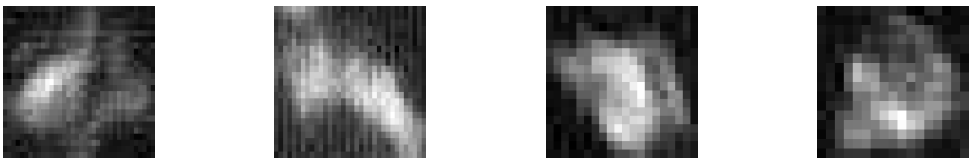

(a) **(b)** **(c)** **(d)**

Figure C.4: Examples cloud candidates.

Land-candidates are shown in Fig. C.5 and it is clear that they are easier to discriminate land from vessels. Their eccentricity, compactness, and convexity lie near 2.5, 3, and 0.8, respectively. However, as the SVM is trained on both large and small vessels, certain large vessels may be misclassified as land as they have similar textures.

Table C.4: Cloud image description

Label	N_p	ε	C_p	C_v
a	589	1.42	1.98	0.952
b	442	2.35	2.26	0.877
c	234	1.20	1.71	0.955
d	196	1.18	1.56	0.956

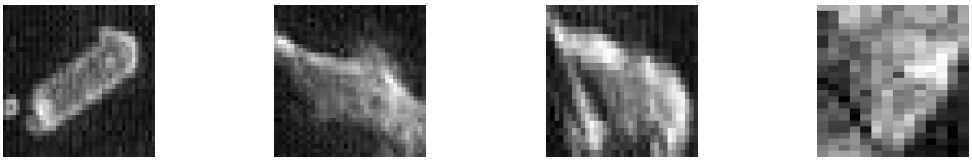

(a) **(b)** **(c)** **(d)**

Figure C.5: Examples land-candidates extracted from the Singapore image-composite.

Finally, the objects shown in Fig. C.6 were unidentifiable under the author's discretion. These objects' features are tabled in Table C.6 and it is evident that they have fewer pixels as the previous examples. However, their features are similar to the smaller vessels' features and, again, might bias the larger vessels' features when using a linear SVM. However, their textures differ greatly from the small vessels and can be separated as such. Notably, when these objects were encountered during the labelling-phase as discussed in Sec. 5.3.2, they were labelled as non-vessel. Arguably, these candidates may be either clouds, clutter or small land-remnants.

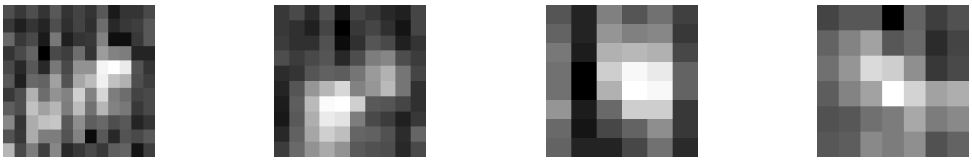

(a) **(b)** **(c)** **(d)**

Figure C.6: Unidentifiable objects extracted from the Singapore image-composite.

Table C.5: Land image description

Label	N_p	ε	C_p	C_v
a	690	2.35	3.37	0.801
b	538	2.31	3.20	0.818
c	447	2.14	3.44	0.865
d	166	3.25	2.70	0.830

Table C.6: Unidentifiable object image description

Label	N_p	ε	C_p	C_v
a	85	1.5	1.65	0.944
b	55	1.72	1.67	0.948
c	30	1.20	1.28	1.000
d	24	1.35	1.33	1.000

C.3 Region Growing

Results from the revised region-growing algorithm discussed in Sec. 5.2.3 will be elaborated upon in this section. This technique is depicted in Fig. C.7, where sets 1 and 2 are clouds and sets 3 and 4 are small vessels, with the methodology expressed in algorithm C.1.

The region-growing omits darker pixels within the BLOb that is fixed with morphological operators. However, these regions will remain should they be larger than the morphological kernels. The region-growing achieved similar results than what would have been achieved with thresholding if the proximity surrounding the RoI contains little clutter and the vessel have a bright deck. However, thresholding will result in wrong vessel boundaries when clutter and deck-variance is introduced, that will result in inaccurate convexity and compactness features.

Furthermore, it is noted that in set 2, the smaller parts of the cloud are omitted in the final result, which leads to a better representation of the cloud's shape. Additionally, the darker part of the vessel's wake, depicted in set 4, is removed, also leading to a better shape-representation.

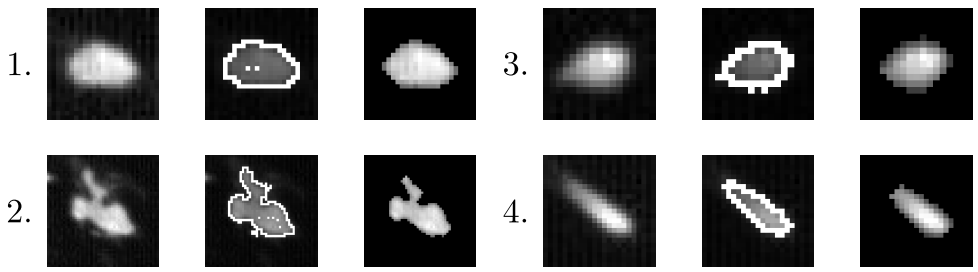

Figure C.7: Region growing examples.

Algorithm C.1: Connected-component labelling used to segment BLObs within a binary image, $B(j, i)$. The algorithm returns a BLOb-array, where a BLOb consists of its respective j- and i-coordinates within the binary image.

Input: $\boldsymbol{B}$
Output: BLObs

```
1  label_next ← 1, linked ← [ ], L ←zeros(B_length, B_width);
2  for j ← 1 to B_length step 1 do
3      for i ← 1 to B_width step 1 do
4          if B[j, i] == 1 then
5              N_N ← L[j − 1, i], N_W ← L[j, i − 1];
6              N_NW ← L[j − 1, i − 1], N_NE ← L[j − 1, i + 1];
7              S ←Unique(N_N, N_W, , N_NW, , N_NE);
8              S[S == 0] ←Null;
9              if S == Null then
10                 linked.append(label_next);
11                 L[j, i] ← label_next;
12                 label_next ← label_next + 1;
13             else
14                 L[j, i] ←min(S);
15                 for label in S do
16                     linked[label − 1] ← linked[label − 1] ∪ S;
17 i ← 0;
18 while i < label_next − 2 do
19     j ← i + 1;
20     while j < label_next − 1 do
21         if len(linked[i] ∩ linked[j])> 0 then
22             linked[i] ← linked[i] ∪ linked[j];
23             Remove(linked[j]);
24         else
25             j ← j + 1;
26     i ← i + 1;
27 for j ← 1 to B_length step 1 do
28     for i ← 1 to B_width step 1 do
29         if B[j, i] == 1 then
30             for slabel in linked do
31                 if label[j, i] in slabel then
32                     blobID ← linked.index(slabel);
33                 blobs[blobID].addPoint(j, i);
```